Ph.D. thesis

Mechanical behaviour of fibre metal laminates based on self-reinforced composites for impact applications

Joseba Iñaki Múgica
Department of Mechanics and Manufacturing
Mondragon Unibertsitatea

A dissertation submitted for the degree of

Doctor of Philosophy

Supervised by
Dr. Laurentzi Aretxabaleta and Dr. Ibai Ulacia

January 2016

A mis *aitas*

Acknowledgements

I would like to express my sincere gratitude to my supervisors, Dr. Laurentzi ARETXABALETA and Dr. Ibai ULACIA, from Mondragon Unibertsitatea, for their guidance, availability and providing me with an excellent atmosphere for researching. I would also like to thank Dr. Laurent GORNET, who gave me the opportunity of experiencing a stage within the École Centrale de Nantes.

This research work could not have been done without the support of the Group of Technology of Polymers and Composites of Mondragon Unibertsitatea consisted of Ingo, Ionson, Maidertxu, Mariasun, Jon, Christofer, Ivan, Esnaola, Jon Ander and Jaione. We have spent so many fun moments, dinners, conferences... Special thanks to Modest for our interesting and constructive numerical discussions and, of course, for the "beverages" we used to have after, wherever we were.

Ha sido un gustazo compartir cada momento con los chicos y chicas de la isla y aledaños: Llavman, Talaska, Erik, Kinian, Elena, Oyangu, Buru, Cuestinson, Eli, Txamaki, Arri... Sin dejar de trabajar, hemos sido capaces de pasarlo fenomenal. No dejaré sin citar a doctorandos "míticos" como Trini, Alaitz, Mendiguren, Aitor, Luis, Sarriegi, Hoskin o Manex. Sabias han sido sus palabras. También, me gustaría recordar al montonazo de compañeros de fatigas nantesas, de entre los que guardo especial recuerdo de Charbel, Elvis, Diego y Leonard. Gracias, cómo no, a todos mis colegas que, repartidos por todo el mundo, no han dejado de acordarse en ningún momento del tipo más peculiar (por vocación) de la cuadrilla. Sí, amigos, ya he acabado.

Tras un punto y aparte, dedico una mención especial a mis más que clasiquérrimos compañeros de Duplexland: Eka, mi confidente de birra y proveedor de risas; Joanet, asceta, cuenta cuentos y gran persona; y mis chicas (menuda suerte que tengo), Ione y Mirentxu.

Finalmente, acabaré agradeciendo infinitamente el estar ahí, no sólo a lo largo de la tesis, sino siempre y para absolutamente todo, a mis aitas, 'el Txefo' y 'la Mon'; y a mis tatas, Ido e Itzi. Mi mayor aspiración es ser un reflejo de vosotros.

Abstract

Lightness and appropriate mechanical response of materials are currently demanded in many applications related to transportation (automotive, aeronautic). Depending on the component, an appropriate mechanical behaviour may consist in having either damage tolerance or energy dissipation capacity. In this regard, it is essential to understand the mechanical behaviour of the materials in order to succeed in the selection of them and the design of components.

Fibre metal laminates (FMLs) are multilayer systems consisting of stacked metal sheets and thin plates of composite material. Among FMLs, the ones based on self-reinforced composites (SRCs) have demonstrated they can offer an excellent response to low and high velocity impact loadings in terms of impact energy dissipating capacity when compared to thermosetting matrix-based systems.

The main objective of this thesis is to study the mechanical behaviour of fibre metal laminates based on SRCs. Within this general objective, three partial subobjectives are established:

- To select the most appropriate SRC-FML, between an Al-based one and a Mg-based one, in terms of energy dissipation capacity under low-velocity impacts.
- To characterise the mechanical behaviour of the plain SRC and to evaluate its influence in the mechanical response of the FML based on the strain rate.
- To develop a constitutive model of the mechanical behaviour of the SRC.

The results reveal that the Al/SRPP-FML is the most appropriate in terms of energy dissipation capacity under low-velocity impacts. After that, the characterisation of the plain SRPP shows that, when the material is submitted to both tensile and shear stresses solicitations, it presents irreversible strains, hysteresis phenomena under cyclic loads, a rate-dependent behaviour and a stiffness varying with the strain. Besides, its influence in the mechanical response of the FML is considerable. Then, a constitutive model of the mechanical behaviour of the SRC is proposed. The model is based on the combination of a elastoplastic model and a fractional viscoelastic model. The numerical-experimental correlation demonstrates that the model is capable of predicting accurately both the cyclic tensile and shear behaviours of the SRPP.

Contents

List of Figures

List of Tables

Nomenclature

Roman Symbols

$\mathbf{N}$	Flow vector
σ_{y0}	Initial yield stress
σ_{y}	Yield stress
a_1	Material parameter 1
a_2	Material parameter 2
E	Tensile damaged elastic modulus
E^0	Tensile undamaged elastic modulus
E^*	Tensile elastic modulus of F-SLS model
E^{m}	Tensile elastic modulus of Maxwell model/branch
E^{r}	Reloading tensile elastic modulus
E^{v}	Tensile viscous modulus of Maxwell model/branch
G	Damaged shear elastic modulus
G^0	Undamaged shear elastic modulus
G^*	Shear elastic modulus of F-SLS model
G^{m}	Shear elastic modulus of Maxwell model/branch

G^{v}	Shear viscous modulus of Maxwell model/branch
$G^{\mathrm{m}}_{\mathrm{u.11}}$	Shear elastic modulus of the Maxwell branch of F-SLS model
$G^{\mathrm{v}}_{\mathrm{u.11}}$	Shear viscous modulus of F-SLS model
h	Energy associated to hardening
K	Hardening material parameter 1
m	Hardening material parameter 2
q	Equivalent stress
R_{s}	Stiffness variability ratio
s	Specific entropy
T	Absolute temperature
t	Time
z_k	Relaxation time for viscous element k
$\mathbf{C}^*$	Elasticity tensor of F-SLS model
$\mathbf{C}$	Elastic stiffness matrix
$\mathbf{C}^{\mathrm{v}}_k$	Discrete viscosity tensor of element k
$\mathbf{d}$	Damage variables vector
$\mathbf{r}$	Stiffening variables vector
$\mathbf{Y}$	Thermodynamic force associated to the damage variables
$\mathbf{Z}$	Thermodynamic force associated to the stiffening variables
$G_{\mathrm{u.11}}$	Shear elastic modulus of F-SLS model
$\mathbf{C}^{\mathrm{m}}$	Elasticity tensor of Maxwell model/branch
$\mathbf{C}^{\mathrm{v}}$	Viscosity tensor

d^{s}	Damage saturation
Y^0	Damage initiation thermodynamic force
Y^{c}	Damage critical thermodynamic force

Greek Symbols

α	Order of fractional derivatives or integrals
$\boldsymbol{\sigma}$	Cauchy stress tensor
$\tilde{\boldsymbol{\sigma}}$	Effective stress tensor
$\boldsymbol{\varepsilon}_k^{\mathrm{v}}$	Internal strain of the dashpot in branch k
δ_{e}	Error function during numerical evaluations
$\mathit{\Gamma}(z)$	Complete Eulers Gamma function
γ	Plastic multiplier
$\mathit{\Psi}$	Flow potential
ψ	Helmholtz free energy potential
ρ	Density
ζ	Damaged-undamaged elastic modulus ratio
β	Damage material parameter
Φ	Yield surface
$\tilde{\boldsymbol{\varepsilon}}^{\mathrm{p}}$	Effective plastic strain tensor
$\boldsymbol{\varepsilon}^{\mathrm{e}}$	Infinitesimal elastic strain tensor
$\boldsymbol{\varepsilon}^{\mathrm{p}}$	Infinitesimal plastic strain tensor
$\boldsymbol{\varepsilon}$	Infinitesimal strain tensor
κ	Hardening thermodynamic force

Υ	Dissipation potential
$\bar{\varepsilon}^{\mathrm{p}}$	Accumulated plastic strain
$\boldsymbol{\sigma}^{\mathrm{m}}$	Cauchy stress tensor of Maxwell model/branch

Other Symbols

${}^{\mathrm{L1}}_{0}\mathrm{D}^{\alpha}_{t}$	L1-algorithm fractional derivative of order α taken with respect to the variable t with lower terminal 0
${}^{\mathrm{L1}}_{0}\mathrm{I}^{\alpha}_{t}$	L1-algorithm fractional integer of order α taken with respect to the variable t with lower terminal 0

Chapter 1

Introduction

The present thesis entitled *Mechanical behaviour of fibre metal laminates based on self-reinforced composites for impact applications* is framed within the Doctorate Programme in Mechanical Engineering and Electrical Energy of Mondragon Unibertsitatea.

1.1 Motivation and background

In December 2011, the European Commission (EC) adopted the Communication "Energy Roadmap 2050". In the roadmap, the European Union (EU) was committed to reduce greenhouse gas emissions to 80-95% below 1990 levels by 2050. Transport is responsible for around a quarter of EU greenhouse gas emissions making it the second biggest greenhouse gas emitting sector after Energy (see Figure 1.1). Specifically, road transport contributes about one-fifth of the EU's total emissions of carbon dioxide (CO_2), the main greenhouse gas.

In the EC's road map was also committed to reduce road mortality. According to the figures, there were 54302 deaths on the EU's roads in 2001. The objective of the previous road safety action programme was to reduce these fatalities by 50% to no more than 27000 deaths in 2010. In 2009, 34500 road mortal victims were reported in the EU; i.e. a 36% reduction was reached. For 2010-2020, the Commission's aim is once again to halve the total number of road deaths in the

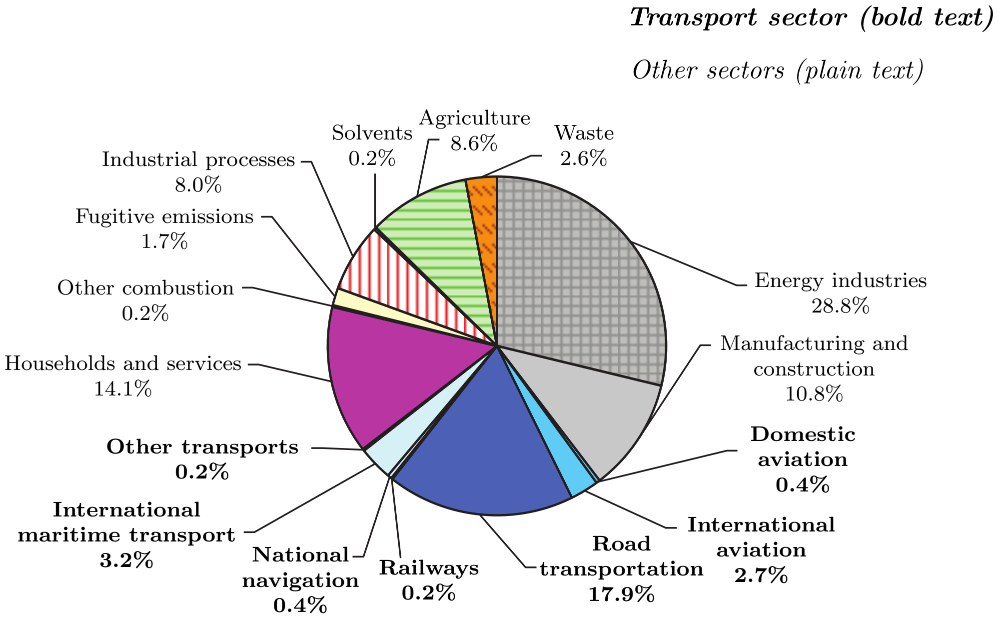

Figure 1.1: Total greenhouse gas emissions by sector (%) in EU-27, 2009.

EU. To achieve this, different strategies have been proposed, among those the manufacturing of safest vehicles can be highlighted.

In this context, lightness and appropriate mechanical response of materials are currently demanded in many applications related to transportation (automotive, aeronautic). Depending on the component, an appropriate mechanical behaviour may consist in having either damage tolerance or energy dissipation capacity. In this regard, it is essential to understand the mechanical behaviour of the materials in order to succeed in the selection of them and the design of components.

Fibre metal laminates (FMLs) are multilayer systems consisting of stacked metal sheets and thin plates of composite material. Each constituent material is responsible for providing its best so that jointly a material with improved properties is obtained when compared to their constituents. While toughness and fatigue resistance are features normally attributed to metals, lightweight is directly related with the concept of composite material.

Among FMLs, the ones based on semicrystalline matrix have demonstrated an excellent response under low and high velocity impacts in terms of energy dissipating capacity when compared to thermosetting polymer matrix-based systems [Abdullah and Cantwell, 2006b]. Moreover, when the semicrystalline matrix composite constituent is a self-reinforced composite (SRC), such capacity is even higher [Abdullah and Cantwell, 2006a].

SRCs are characterised by the reinforcing and matrix phases belong to the same polymer family. In comparison with thermoplastic or thermosetting matrix composites based on inorganic reinforcements, SRCs present several advantages: they are more lightweight, entirely recyclable and show higher damage tolerance [Aurrekoetxea et al., 2011]. Currently, there are commercial SRCs based on polypropylene, polyethylene terephthalate and polyethylene. SRCs present a relatively complex mechanical behaviour since they are orthotropic and significantly viscous when compared to thermoplastic or thermosetting matrix composites based on inorganic reinforcements. Besides, damage also occurs into SRCs when submitted to loads [Aurrekoetxea et al., 2011].

The researches conducted on SRCs have essentially dealt with the development of an energetically optimal manufacturing process and the study of the resulting mechanical properties depending on the process parameters. Concerning the research works on SRCs-based FMLs, the objects of study have been their impact and interlaminar behaviour, the scaling effects on the mechanical response and their formability. In every cases, they were based on aluminium.

Currently, the use of SRCs in automotive sector is spreading and, for this reason, researchers are increasingly focused on their study, both plain and as a part of a FML. However, there is a lack of knowledge about the use of SRCs to manufacture FMLs based on alternative lightweight metals different of aluminium, also concerning the influence of the mechanical behaviour of SRCs in FMLs and their modelling, being this last topic really important for the design of parts of both SRCs and SRCs-based FMLs.

1.2 Objectives and organisation of the thesis

The main objective of this thesis is to study the mechanical behaviour of fibre metal laminates based on self-reinforced composites for impact applications. In order to achieve this general objective, three partial subobjectives are established:

- To select the most appropriate SRC-FML, between an Al-based one and a Mg-based one, in terms of energy dissipation capacity under low-velocity impacts.
- To characterise the mechanical behaviour of the plain SRC and to evaluate its influence in the mechanical response of the FML based on the strain rate.
- To develop a numerical model of the mechanical behaviour of the SRC.

Each subobjective of the research work is associated to a chapter in this thesis, which is composed of six chapters including the general introduction and the scientific and technological framework corresponding, respectively, to Chapter 1 and Chapter 2.

Chapter 3 is devoted to the low-velocity impact behaviour of SRC-based FMLs. Firstly, the SRC, among three commercial alternatives, which offers the most appropriate response under low-velocity impacts based on the energy dissipation capacity, is selected. Secondly, an aluminium-based FML and a magnesium-based FML are manufactured, whose low-velocity impact behaviours are comprehensively studied to select the most appropriate FML based on its impact response.

Chapter 4 concerns the mechanical characterisation of the SRC. Its tensile and shear behaviours at different strain rates are studied. Then, the influence of the SRC in the mechanical response of the FML is evaluated based on the strain rate.

Chapter 5 addresses the mechanical behaviour modelling task. After observing the significant influence of the SRC in the mechanical response of the FML, a constitutive model within the framework of thermodynamics of irreversible processes is developed for the plain composite.

Chapter 6, finally, collects the main conclusions obtained during the research work and presents some future works.

Chapter 2

Scientific and technological framework

In this chapter, the scientific and technological framework of the mechanical behaviour of SRCs and SRCs-based FMLs is presented. Firstly, the origin and evolution of FMLs is described. Secondly, the low-velocity impact behaviour of FLMs depending on the constituent materials is shown. Then, the research works on the mechanical behaviour of SRCs-based FMLs are reviewed. Finally, the main trends concerning the modelling of composite materials, including SRCs, are commented.

2.1 Introduction

2.1.1 The hybridization concept

Hybridization[1], in Animal Biology, is any offspring resulting from the mating of two genetically distinct individuals; in Molecular Biology, the process of establishing an interaction between two or more complementary strands of acids into a single complex; in Motor Industry, the combination of a conventional

---

[1] According to the Oxford English Dictionary, the word is derived from Latin hybrida, meaning the “offspring of an tame sow and a wild boar”, “child of a freeman and slave”, etc. The term entered into popular use in English in the 19th century, though examples of its use have been found from the early 17th century.

internal combustion engine (ICE) propulsion system with an electric propulsion system. Such concept appears repeatedly at different scales in numerous scientific areas. Nature shows the best example of the potential of hybridization with the shells of molluscs [Meyers et al., 2008]. Shells are basically constituted by one or more ceramic phases and a minimum quantity of proteins (between 0.1% and 5%). These ceramic phases, an example is calcium carbonate ($CaCO_3$), are brittle by nature and they are not valid as armour. However, the resultant bio-composite when combined with proteins in order to obtain a complex laminar structure shows very superior mechanical properties when compared to the monolithic ceramic phase, e.g. the fracture toughness and tensile strength of $CaCO_3$ bio-composite are 20-30 higher than that of monolithic version.

Likewise, human has made use of hybridization to the development of new alternative materials. In structural design engineering, such concept is applied to join the virtues of materials of different nature. FMLs are an example of materials hybridization; they are multilayer structures consisting of stacked metal sheets and thin plates of composite materials. Each constituent material is responsible for providing its best so that jointly a material with specific mechanical properties is obtained (see Fig. 2.1).

2.1.2 Origin and evolution of FMLs

During the last decades the application of composite materials in aerospace, aircraft and automotive sectors has become increasingly popular. Composite

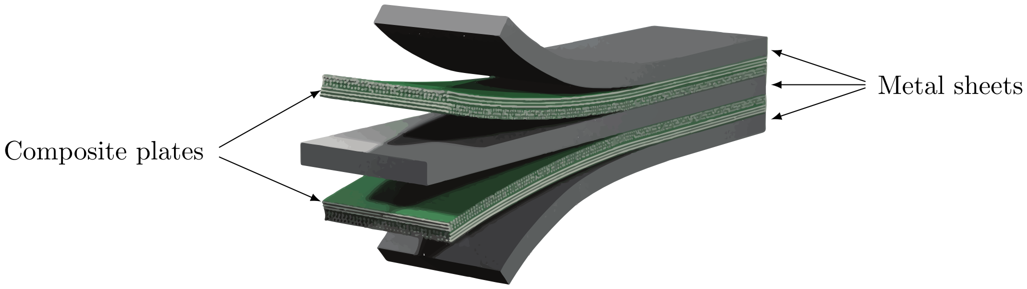

Figure 2.1: Configuration of a typical fibre-metal laminate (FML).

materials have replaced traditional materials, such as metals, in numerous applications because of their improved specific mechanical properties concerning strength/stiffness ratio and fatigue resistance. However, there exist other applications where the positioning of composite materials is not possible since their mechanical response do not enhance that of the original material. In this regard, the demands by the Aircraft Industry and Defence of increasingly lightweight and high-performance materials resulted in the conception of laminate materials consisted of metal sheets and composite thin plates. These were named 'hybrid materials'. The recognized fatigue and fracture behaviour associated with fibre-reinforced composite materials combined with the plastic behaviour and durability offered by many metals gave way to the age of laminate materials based on composite and metal [Vlot, 2001a].

A. Vlot, researcher of Delft University of Technology, firstly introduced the concept of hybridization into materials in the 80's; the result was a new material typology which was called fibre-metal laminate, FML [Vlot, 2001a]. The first generation of FMLs were based on thermoset matrixes, typically epoxy, as its stiffness and thermo-mechanical strength is higher than that of thermoplastic ones. After years of research and development, two commercial FMLs arose. Firstly, ARALL®, whose constituents are aramid fibre-reinforced epoxy composite (AFRP) and aluminium sheets; it is currently utilized in military aviation. Then, GLARE® [Vlot, 2001b], whose composite constituent is S2-glass fibre-reinforced epoxy (GFRP), is currently one of the key materials used to manufacture the upper fuselage of the Airbus A380 [Pora and Hinrichsen, 2001] (see Fig. 2.2).

The success of GLARE® was due to its fatigue resistance, higher than that of its predecessor, monolithic aluminium, and its lightness since it supposed a weight reduction of 30%. Once FML was established in the aircraft sector, the interest in introducing them into the automotive industry emerged. Something similar happened successfully with composite materials. After being used in aeroplanes, they were introduced in luxury cars, e.g. the Lamborghini Sesto Elemento, with a body made of carbon fibre-reinforced polymer, (CFRP), and high-end cars, e.g.

Figure 2.2: Image of the Airbus A380 highlighting the upper fuselage which is made of GLARE®.

the Audi A8 (launched in 2015), with rims made of still an unknown reinforced polymer called 'Chromtec', which will lead to a total weight saving of 18 kg [Chr, 2015]. More recently, BMW has started the production of its revolutionary i3 city car, which is the first mass-produced automobile using a composite frame. The composite-based design supposes a total vehicle weight saving of 350 kg when compared to a steel-based one. According to Automotive Light-weighting Materials (ALM) project, a 10% weight reduction in vehicle implies a 7% fuel saving, which implies a decreasing of combustion gas emissions to atmosphere. These facts suggest that, as happened with composites, the introduction of FMLs in automotive industry seems to be something possible; however, their effect would be limited by now to relatively high cost products and generally low volume of production.

2.2 Impact behaviour of FMLs

The utilization of FMLs in Transportation Sector makes them susceptible to impacts. As an example, among different types of damages in an aircraft, such as fatigue, corrosion and accidental (impact) damage, it is reported that at least 13% of 688 repairs to 71 Boeing 747 fuselages were related to impact damage, usually located around the doors, on the nose of the aircraft, in the cargo compartments and at the tail (due to tail scrape over the runway) [Vlot, 1993a]. Impact damage of aircraft is caused by sources such as runway debris, hail, maintenance damage or dropped tool, collisions between service cars or cargo and the structure, bird strike, ice from propellers striking the fuselage, engine debris, tire shrapnel from tread separation and tire rupture and ballistic impact (for military aircraft) [Vlot, 1993b]. In automotive, as happened in aircraft, vehicles can be subjected to impact loads in different situations: crash, a rock hitting or even when an animal is knocked down. Every of them can compromise the safety of occupants in road.

In short, the nature of impacts in transportation varies, just like the velocity of impacts and, by extension, the strain-rates within the parts. This justifies the interest of the rate-dependent behaviour of materials as study object. Scientifically, impacts are categorized according to the velocity; ‘low-velocity impacts’, until approximately 15 m/s, and ‘high-velocity impacts’, for higher velocities.

2.2.1 Types of metal constituents for FMLs

The use in research works of aluminium, specifically the 2024-T3 aluminium alloy as metal constituent in FMLs, has been the habitual trend until now due to its competitive price and specific mechanical properties; however, there exist other alternative metal constituents, such as magnesium, titanium, nickel-titanium or steel, which can provide interesting properties for specific applications. Among the different options mentioned, the last three are the less used mainly due to their relatively high weight in comparison with the two first. According to the bibliography, while it is true that aluminium is at the top of the ranking in use in research works, its substitution by magnesium in FMLs constitutes an interesting alternative in Aircraft and Automotive Industry due to its lower density. Moreover, apart from this, it is also worth highlighting its improved electromagnetic shielding capability and superior corrosion resistance. In this regard, diverse authors have tried to elucidate which alternative as metal constituent in a FML would provide better mechanical response under low-velocity impacts.

On the one hand, Cortés and Cantwell [2006b] studied the impact properties of different alternatives of AZ31 magnesium FMLs. They demonstrated that a

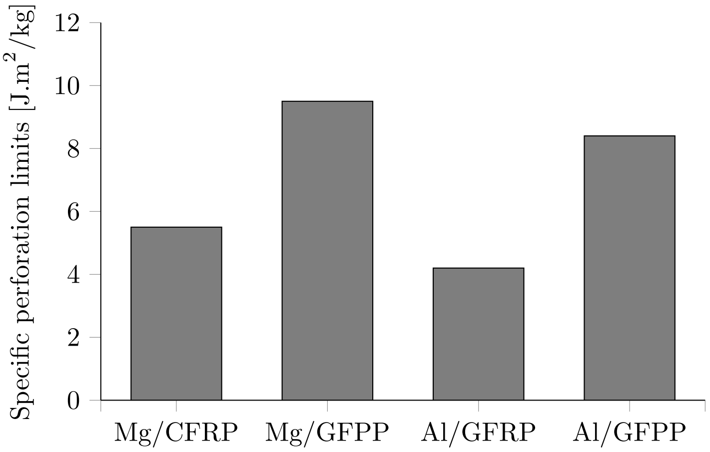

Figure 2.3: Comparison of the specific perforation energies of two magnesium alloy FMLs, a carbon fibre-reinforced (CFRP) one and a GFPP one, with a woven Al/GFRP-FML and a unidirectional Al/GFPP-FML (Adapted from [Cortés and Cantwell, 2006b]).

magnesium laminate with glass fibre-reinforced polypropylene (GFPP) offered superior specific perforation resistance to those offered by both an aluminium/glass fibre-reinforced epoxy (GFRP) and an aluminium/unidirectional GFPP (see Fig. 2.3), suggesting that magnesium multi-layered systems could offer an improved resistance to localised impact loading.

On the other hand, Alderliesten et al. [2008] studied the applicability of magnesium FMLs in aerospace structures. They carried out an initial viability study by using validated prediction models addressed and obtained from literature. They concluded that in spite of the weight reduction which magnesium provided in comparison with aluminium, its lower properties required changing the structural design, which most likely would nullify the weight saving for most structures. Besides, a direct comparative between S2-glass/epoxy-based Mg-FML and Al-FML have been undertaken recently by Pärnänen et al. [2012], who compared the impact responses of the first one with AZ31B-H24 magnesium and the other with 2024-T3 aluminium of two different thicknesses. In their work, they concluded that the Mg-FML did not offer an improvement in perforation resistance or damage tolerance over the traditional Al-FML; the specific limit energies for perforation of the Mg-FML and the Al-FML were equal (see Fig. 2.4), and the

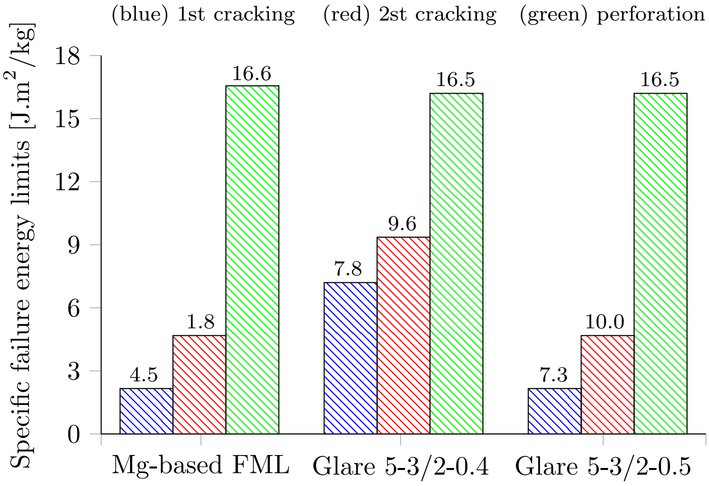

Figure 2.4: Specific limit energies of a Mg/GFRP-FML and two Al/GFRP-FMLs of different thicknesses of constituent metal (Adapted from [Pärnänen et al., 2012]).

extent of cracked metal as well as the delamination area were higher in the Mg-FML for the same impact energy (see Fig. 2.5). The authors affirmed that the higher the rate of strain hardening and the fracture toughness of a constituent metal, the smaller the delaminated area and the extent of metal cracking in the FML. Unfortunately, the above comparative studies [Cortés and Cantwell, 2006b; Pärnänen et al., 2012] cannot be directly compared since stacking configuration as well as the thickness of the constituents were different [Pärnänen et al., 2012].

As previously mentioned, although to a lesser degree, titanium has been proposed in the literature as another alternative metal constituent in FMLs [Cortés and Cantwell, 2002, 2006a,c; Johnson et al., 1996]. [Cortés and Cantwell, 2004] initially performed tension-tension fatigue tests on notched unidirectional carbon fibre-reinforced poly-ether-ether-ketone (PEEK) Ti-FMLs and appreciated that these laminates offered fatigue lives up to fifty times greater than those of notched monolithic titanium alloy. These authors stated that FMLs based on titanium alloys appeared to be the most attractive for Aerospace Industry as they would extend the advantages of the existing GLARE® to higher temperatures [Cortés and Cantwell, 2005]. Bourlegat et al. [2010] produced a laminate with carbon fibre reinforced epoxy (CFRE) prepreg and titanium sheets

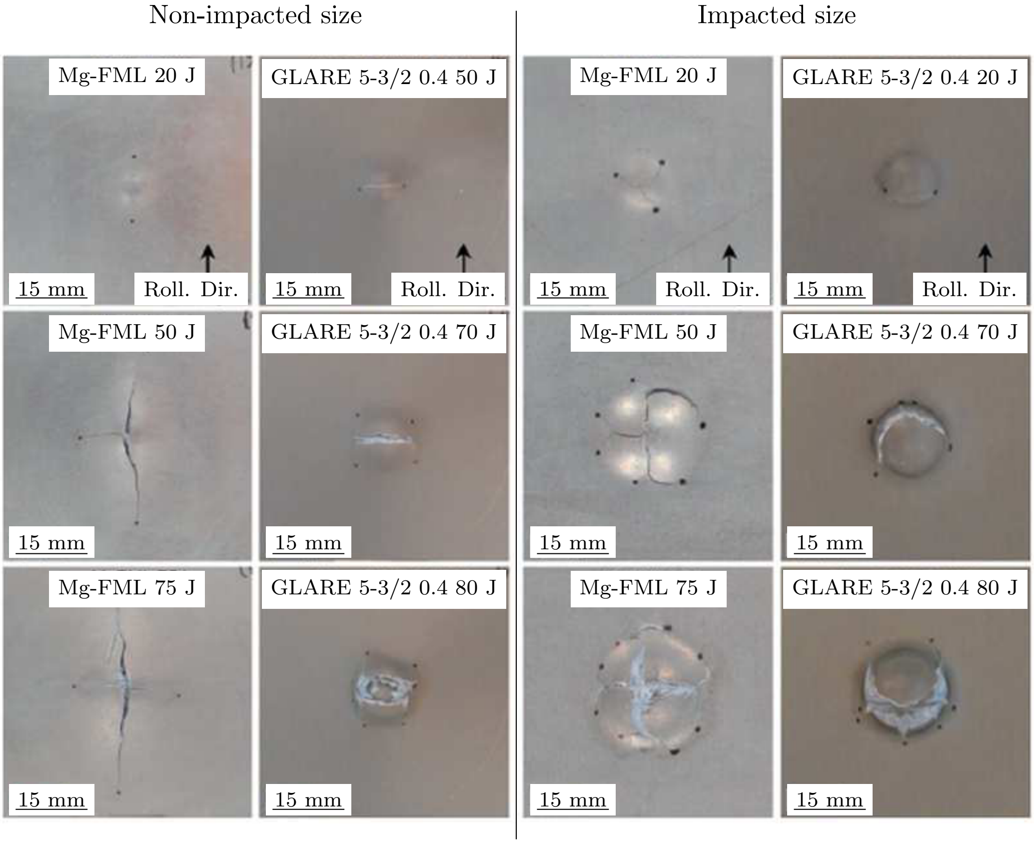

Figure 2.5: Examples of metal cracking patterns on the non-impacted and impacted sides of the Mg/GFRP-FML and the Al(0.4)/GFRP-FML specimens (Images taken from [Pärnänen et al., 2012]). The ends of the crack tips are marked with black dots.

inside of autoclave system. According to this study, the tensile stress, tensile modulus, shear stress, and shear modulus values for titanium/CFRE laminates are superior to those of GLARE® and CARALL®. Li and Johnson [1998] manufactured hybrid titanium composite laminates (HTCLs) with prepreg layers of high-temperature resin reinforced with carbon fibres; they assessed that the performance of the HTCLs in fatigue was better than the one of the monolithic titanium alloy for room-temperature and elevated-temperature conditions. Nevertheless, Cortés and Cantwell [2007], when studied in a subsequent work the low and high-velocity impact properties of two Ti-FMLs based on carbon fibre-reinforced PEEK (CF/PEEK) and glass fibre-reinforced poly-ether-imide (GF/PEI) composites, reduced the profile of Ti-FMLs as potential material to

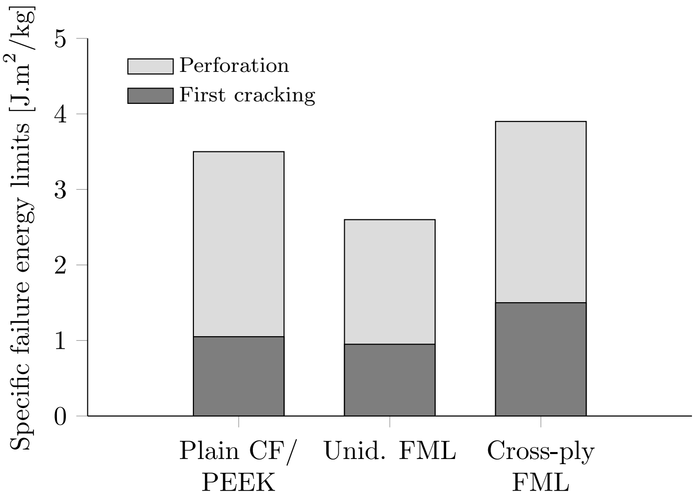

Figure 2.6: Specific perforation energies of a titanium-based CF/PEEK FML and the plain composite (Adapted from [Cortés and Cantwell, 2007]).

applications susceptible to impacts. In accordance with their study, low velocity impact tests showed that the specific perforation energy of the CF/PEEK FML was similar to that offered by the CF/PEEK composite (see Fig. 2.6) and, in contrast, for the GF/PEI FML system this value was lower than that of the plain GF/PEI composite (see Fig. 2.7). As an exception, under high velocity impacts, the specific perforation energy of the GF/PEI FML resulted higher than those exhibited by the plain GF/PEI composite.

Briefly, and according to Cortes and Cantwell, the experimental evidence suggests that titanium-based alloys are not recommendable as constitutive metal in FMLs for impact applications. Regarding the other alternatives of metal constituents, nickel-titanium and steel, they have also been object of study when used in a FML, as previously commented [Cortés et al., 2007, 2008; Reyes and Gupta, 2009]; however, their low-velocity impact behaviour has not been studied yet.

2.2.2 Types of matrices for FMLs

First FMLs, developed for aerospace applications, were based on thermosetting matrix composites. These composites present higher stiffness, strength and

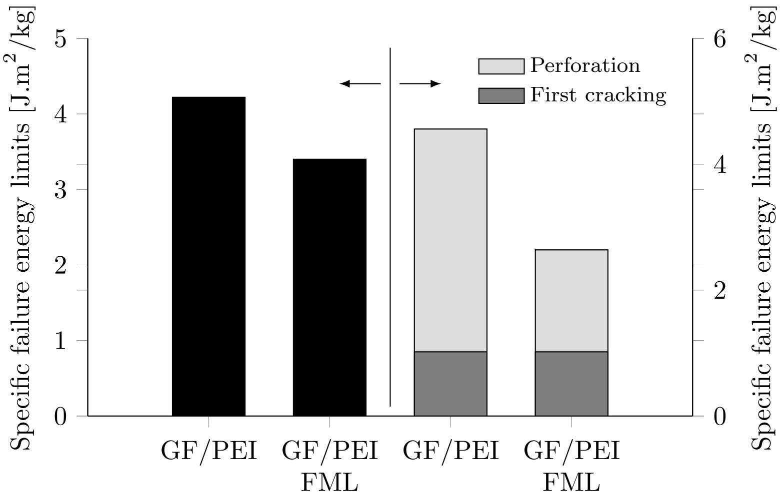

Figure 2.7: Specific perforation energies of a titanium-based GF/PEI FML and the plain composite (Adapted from [Cortés and Cantwell, 2007]).

temperature resistance compared to thermoplastic matrix composites. However, thermosetting matrix-based FMLs present comparatively disadvantages such as brittleness, requirement of relatively long processing cycles to ensure the complete curing and the providing of optimized bonding across the composite/metal interface, even difficulties associated with repair. These drawbacks have been in the last decades the reason of increasing the attention to the thermoplastic matrix-based FMLs [Bourlegat et al., 2010; Cortés and Cantwell, 2004, 2005, 2006a,c, 2007; Cortés et al., 2007, 2008; Li and Johnson, 1998; Reyes and Gupta, 2009; Vlot, 1993b]. These last ones offer several advantages associated to the manufacturing process; shorter cycle times, absence of volatile substances, possibility of post-manufacturing forming, etc. Furthermore, they present functional advantages concerning mechanical properties, such as higher toughness and interlayer toughness, as well as lower density, higher facility to repair and to recycle [Reyes and Kang, 2007].

Currently, there is not any comprehensive work to compare the low-velocity impact behaviour of both FML types. Most of studies on GF thermoplastic composite FMLs are on high-velocity impact [Abdullah and Cantwell, 2006a; Compston et al., 2001; Reyes and Cantwell, 2004]. However, it is worth noticing that in the high velocity impact studies Compston et al. [2001] demonstrated that the specific perforation energy of GFPP-based FMLs is about 25% higher than for the the corresponding thermosetting matrix GLARE®. In the same study, it is reported that GFPP-based FMLs show an increase in the ballistic perforation limit of 50% when compared to monolithic aluminium alloy.

2.3 SRCs, all-thermoplastic composites

2.3.1 SRCs, an alternative to traditional composites

In response to the proposals expressed by the EC, to put only 5% of ELV residues into landfills [dir, 2000], recyclability of materials is a topic increasingly important in Automotive Industry. At the same time, it is indispensable that the compliance with this demand does not prejudice to the requirements concerning the safety of vehicles. Nowadays, it can be said that utilization of composite materials in such industry is a reality, where the impact performance, impact damage tolerance and post-impact integrity are some of the most important safety issues. Traditional ceramic fibre composites can be damaged when submitted to low-energy impacts and, consequently, the residual properties of these composites can be degraded [Richardson and Wisheart, 1996]. On the other side, thermoplastic fibre composites are normally less sensitive to damage caused by such solicitations due to their plastic behaviour [Bigg, 1994].

Self-reinforced thermoplastic composites or, simply, self-reinforced composites (SRCs) (also called self-reinforced polymers (SRP), all-polymer composites or all-thermoplastic composites) are composite materials in which the reinforcement and the matrix belong to the same polymer family [Kmetty et al., 2010]. The reinforcement consists in highly oriented thermoplastic fibres embedded in an amorphous matrix. The adhesion between the two phases takes place at molecular level thanks to the chemical compatibility of the phases. As a result, SRCs present higher strength and stiffness than the bulk polymeric material [Alcock et al., 2006, 2007]. In comparison with other thermoplastic or thermosetting matrix composites with GF or other inorganic reinforcements, SRCs are the most lightweight and presents easier recyclability [Peijs, 2003], attributes in line with the cited purposes of the EC [dir, 2000]. For example, GFRP can only be recycled into new fibre reinforced grades because of the difficulty of separating glass fibres from polymer matrix. Unlike GFRP, all-polymer composites can be entirely melted at the end of the product life for recycling into polymer feedstock which can be used for a wide range of future applications [Peijs, 2003]. Moreover, these composites have also demonstrated other interesting properties when compared to thermosetting matrix composites, such as higher impact damage tolerance and post-impact integrity [Aurrekoetxea et al., 2011] and possibility of forming, single [Cabrera et al., 2008] or jointly with metal as FML [Compston et al., 2004; Gresham et al., 2006; Kalyanasundaram et al., 2007, 2013; Mosse et al., 2005a,b, 2006; Reyes and Gupta, 2005; Sexton et al., 2012].

2.3.2 Origin and evolution of SRCs

The first example of SRC was attributed to Capiati and Porter [1975]. They defined the concept of 'one polymer composite', in their case made of high-density polyethylene (HDPE), which was based on a difference in melting points between fibre and matrix. The authors manufactured fibres that contained aligned and extended chains which in turn provided thermodynamically more stable crystals, with higher melting points than conventional ones. They stated that the growth of transcrystalline regions in the melt matrix at the interface plus partial melting between fibre and matrix were indications of a strong and intimate interfacial bond with a gradient in morphologies for the system studied. Following this pioneering work, numerous studies have been carried out on SRCs. Several techniques have been developed and utilized to prepare these composites, including film stacking [He and Porter, 1988; Zhang et al., 2009], powder or solution impregnation [Lacroix et al., 1998, 1999], hot compaction [Hine et al., 1993; Ward and Hine, 2004], co-extrusion [Peijs, 2003] and selective surface dissolution [Qin et al., 2008; Soykeabkaew et al., 2008; Zhang et al., 2010].

Polymers, such as polyethylene (PE) and polypropylene (PP), have been particularly investigated and utilized from the very beginning for manufacturing of SRCs because of their use in large number of industrial and domestic applications. Nevertheless, the glass transition and melting temperatures of PE are lower than those of PP, which means that creep and usage at elevated temperatures can be problematic [Govaert and Peijs, 1995; Govaert et al., 1991, 1993]. Therefore, in the recent years increasingly effort has been given to the research of PP and its use in SRCs. This trend has prevailed to the point that nowadays there are available commercial SRPPs, e.g. Curv® [Pro, 2015], Tegris® [Teg, 2015], PURE® [Pur, 2015] or Armordon® [Arm, 2015]. From them, different kinds of products, for automotive, sport staff or luggage, are currently manufactured (see Fig. 2.8).

At the same time, researchers, encouraged by the success of all-PP composites, also focused on Poly(ethylene terephthalate) PET ($T_\mathrm{g} \approx 80\,°\mathrm{C}$, $T_\mathrm{m} \approx 265\,°\mathrm{C}$), which constituted an alternative solution to manufacture all-PET composites for applications when temperature range is not attainable for SRPP. Moreover, as there are well-developed recycling schemes for PET, SRC based on recycled PET could be obtained [Pla, 2010]. In this regard, researchers from University of Leeds successfully applied the hot compaction method in the manufacturing of SRPET, studying the influence of process variables [Hine and Ward, 2004; Rasburn et al., 1995]. Likewise, another research team from the University of Connecticut also investigated the influence of amorphous and crystalline phases on mechanical properties [Rojanapitayakorn et al., 2005]. Besides, Zhang et al. [2009] and Zhang

Figure 2.8: Some products made of SRPP; (a) under body shields, (b) ice skating boots and (c) suitcases.

and Peijs [2010] used the film stacking method to manufacture SRPET and implementing a combined process of filament winding and hot-pressing, respectively.

2.4 FMLs based on SRCs

The aforementioned strengths of thermoplastic-based FMLs led researchers to carry out plenty of research works on mechanical response of such type of FMLs. Among these, GFPP-based FMLs have been the most studied in the last two decades. Its interlayer behaviour [Reyes and Cantwell, 1998], formability [Reyes and Gupta, 2005], fatigue behaviour [Reyes and Kang, 2007], low-velocity impact response [Reyes and Cantwell, 2000] and high-velocity impact response [Abdullah and Cantwell, 2006b; Cantwell et al., 2001, 2002] have already been comprehensively studied. The extensive testing on such material has shown that it offers an excellent response to low and high velocity impact loads in terms of impact energy dissipating capacity when compared particularly to thermosetting matrix-based systems.

Recently, Abdullah and Cantwell [2006a, 2012] analysed the high-velocity impact resistance of SRPP-based FMLs. Initial tests were conducted on 2/1 stacking FMLs based on 2024-O and 2024-T3 aluminium alloy sheets and SRPP core of different thicknesses (sandwich laminates). They determined that laminates based on the 2024-T3 alloy offered higher perforation resistance to those based on 2024-O alloy. Besides, tests were also conducted on 3/2, 4/3 and 5/4 stacking multi-layered laminates in which the composite plies, always of the same thickness, were dispersed between more than two aluminium sheets. For a given target thickness, the multi-layered systems offered higher perforation resistance than the sandwich laminates, while these latter ones demonstrated higher specific perforation resistance (SPR) than the former ones.

Additionally, the 3/2 stacking FML were contrasted with other thermoplastic matrix composites FMLs of same stacking configuration; e.g. the former offered roughly double SPE than that of exhibited by a Kevlar-based laminate (see Fig. 2.9). To date, SRPP is the unique all-polymer composite used as composite con-

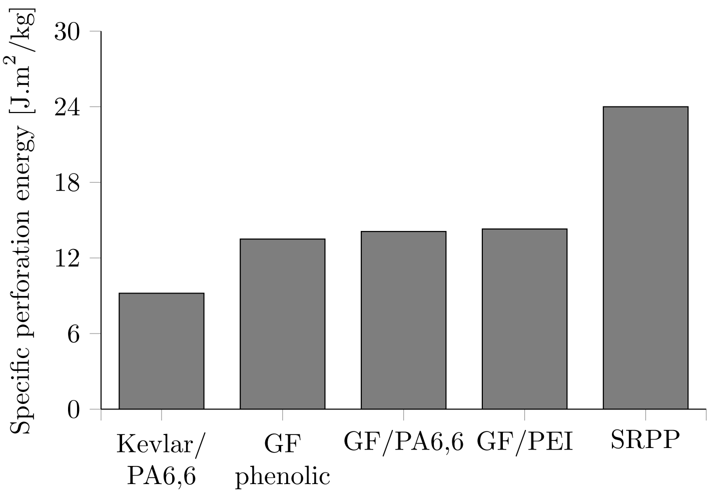

Figure 2.9: Specific perforation energy of 3/2, 4/3 and 5/4 stacking configuration FMLs based on 2024-T3 and 2024-O aluminium with SRPP (Adapted from [Abdullah and Cantwell, 2006a, 2012]).

stituent in a FML and in all of these cases the metal constituent was aluminium. Among these works, there is no one about the capacity to dissipate energy under low-velocity impact loads.

2.5 Theoretical modelling of polymeric matrix composite

2.5.1 Classical models

Until about two decades ago, the scientific interest was mainly focused on the modelling of thermosetting matrix composite materials. Ladevèze et al. developed elastic models defined at the mesoscale level for carbon fibre reinforced laminates with unidirectional plies which correctly describe the intralaminar and even interlaminar damage mechanisms by the use of damage variables that take into account the decrease elastic moduli observed in experiments [Allix et al., 1998; Hild et al., 1997; Ladevèze, 1986, 1995; Ladevèze and LeDantec, 1992]. More recently Rozycki [2000] extended the model to take into account the strain rate effects on glass-fibre reinforced composites. Based on the methods developed for unidirectional ply composites previously mentioned, several authors have presented adapted methods for fabric reinforced composites under in-plane loads [Hochard et al., 2001; Johnson et al., 2001; Marguet, 2007; Marguet et al., 2007; Rozycki, 2000]. These models allow a correct description of the damage mechanisms at a reasonably low computational cost by the use of damage variables to describe the elastic moduli decrease [Lemaitre and Desmorat, 2005]. The irreversible strains have classically been described by plastic hardening models [Hochard et al., 2001; Ladevèze and LeDantec, 1992] or viscoplastic models [Marguet et al., 2007; Rozycki, 2000] which take into account strain rate effects.

Nevertheless, the hysteresis phenomenon occurring under cyclic loads, associated to the viscous character of polymers, has not been modelled in the aforementioned works. Such phenomenon affects the thermomechanical behaviour in both tensile [O. Westphal and Rozycki, 2012] and impact [Aurrekoetxea et al., 2011] fatigue loads. Several authors have developed models which take into account the hysteresis loops: Maire based on [J.M. Bribis and Naslain, 1985], proposed a spectral model for glass fibre-epoxy composites [Maire, 1992]. Hild et al. developed a model using of a damage variable which takes into account the size of the slip zone related to the crack spacing [Hild et al., 1996, 1997]. Halm and Dragon developed an anisotropic damage model which introduces a internal variable to account for the frictional sliding of closed microcracks within the material [Halm and Dragon, 1998]. More recently, Bois proposed a rheological model based on the superposition of a finite and infinite number of branches to model the sliding and adherence phenomena within the fissures inside the fabric reincoforced composite material [Bois, 2003] (see Appendix A.1). The main drawback of these models is the need of a relative big number of material parameters to obtain reasonable results.

Another possibility is the use of fractional models, which allow to reduce the number of necessary parameters to obtain comparable results to those of the previously cited models. Mateos [2014] modelled successfully the hysteretic and damage behaviour of carbon fibre reinforced composite materials by using fractional operators.

2.5.2 Fractional models

Fractional calculus is nowadays applied in many fields of science and engineering. In solid mechanics, fractional operators are now considered to be a convenient tool to model the constitutive behaviour of viscoelastic materials. In 1921, Nutting observed that the viscoelastic properties of materials appeared to be proportional to fractional powers of time [Nutting, 1921] and posteriorly, in 1936, Gemant proved the dependence of the viscoelastic properties on fractional powers of frequency [Gemant, 1936]. These findings led the latter to suggest the use of fractional operators to model material viscoelastic behaviour [Gemant, 1938].

From then on, several authors have addressed viscoelastic behaviour modelling by using fractional calculus. Scott-Blair and Caffyn [1949] proposed the use of fractional derivatives to relate time dependent strain and stress in viscoelastic materials. More recently, the application of fractional derivatives to viscoelasticity was extensively studied by Caputo [1969] and Caputo and Mainardi [1971]. At the beginning of the 80's, Bagley and Torvik [1983, 1986] physically justified the use of fractional models from a molecular point of view and later they developed the conditions to obtain thermodynamic consistency to assure a non-negative energy dissipation. Koeller [1984] suggested to replace the classical dashpots in the rheological models by generalised viscous elements called spring-pots. This name conveys the fact that for α fractional order values near 0, the element behaviour is nearly the one showed by an elastic spring and for α values close to 1, the behaviour is almost similar to that dissipative nature of dashpots. Thus, the spring-pots enable to model a wide range of behaviours by varying the values of α. A number of theoretical and experimetal studies have been devoted to this behaviour: Cosson [1995] characterised the mechanical behaviour of elastomers by fractional models. Enelund and Olsson [1999] analysed the performance of fractional models for viscoelastic behaviour characterisation and Adolfsson et al. [2005] developed a fractional behaviour formulation based on internal variables to reduce computational effort. On the other hand, several works have been devoted to the finite element implementation of fractional models and the reduction of the numerical effort during the evaluation of fractional derivatives: Padovan [1987] developed solution algorithms for finite element transient analysis of viscoelastic materials. Yuan and Agrawal [2002] developed a numerical scheme based on the Laguerre integral formula to reduce computational cost. Schmidt and Gaul [2002] developed a finite element formulation based on the Grünwald definition of fractional derivatives. Galucio et al. [2004] developed a finite element formulation for transient analysis of sandwich with a four parameter fractional model. Schmidt and Gaul [2006] developed a modified numerical scheme based on the use of transfer functions to evaluate the fractional derivatives. More recently, Deü and Matignon [2010] have developed a numerical scheme for the evaluation of fractional derivatives by combining a Newmark method and a diffusive representation of the fractional derivatives. The aforementioned works constitute good examples of fractional models ability to describe viscoelastic material behaviour in several analyses.

Origin and evolution of fractional calculus

Fractional calculus deals with integral and differential operators of non-integer order α. In fact, it generalises the concepts of derivative and integral (or antiderivative) operations of differential and integral calculus from integer orders to the entire complex plane. Nevertheless, fractional calculus is almost as old as calculus itself. Its origin goes back more than three centuries, when in 1695 in a letter Leibniz and L'Hôpital [1849] gave a first answer to a question from Gillaume de L'Hôpital about the mathematical meaning of a fractional derivative of order 1/2. The topic of fractional or irrational order derivatives [Leibniz and Bernouilli, 1850a] and later on derivatives of general order [Leibniz and Bernouilli, 1850b] can also be found in correspondences between Bernouilli and Leibniz in 1695. After the death of Leibniz in 1716, the topic of non-integer order derivatives continued with Euler's generalisation in 1738 of factorials when he worked on arithmetic progressions [Euler, 1738], concluding with the definition of the posteriorly so called as Gamma function by Legendre (see Appendix B.1).

The first detailed definition of a fractional derivative is considered to have been given by Laplace [1812]. Some years later, Lacroix [1819] devoted less than two pages to derivatives of arbitrary order in his book on differential and integral calculus, where he worked on the generalisation of the derivatives of integer order m of the function $y(x) = x^n$, $n \in \mathbb{N}$ to fractional order by the use of Euler's Gamma function. The relevance of Lacroix's work lies in the fact that his result is the same obtained by nowaday's Riemann-Liouville definition of a fractional integro-differential. Since then, many authors contributed to the evolution of fractional derivation and integration [Abel, 1881; Caputo, 1967; Fourier, 1822; Grünwald, 1867; Letnikov, 1868; Riemann, 1953; Sonin, 1869]. In 1974, the first conference devoted exclusively to the theory and applications of fractional calculus was held in the University of New Haven. In that same year, the first book on fractional calculus by Oldham and Spanier [1974] was published. After that, several books have appeared, the most popular being the ones by Miller and Ross [1993], S. Samko and Marichev [1993], Podlubny [1999], Hilfer [2000] , and more recently the ones by A.A. Kilbas and Trujillo [2006], Magin [2006] and Mainardi [2010]. Finally, in 1998, the first issue of the mathematical journal "Fractional calculus and applied analysis" appeared, which deals exclusively with topics on fractional calculus theory and applications.

As it has been seen above, several different fractional operators have been developed throughout history. In the following subsection the Riemann-Liouville (RL) fractional integro-differential, utilized in this research work, is described.

Riemann-Liouville fractional integro-differentials

The Riemann-Liouville definition of integro-differential operator is based on the Cauchy formula for repeated integration:

$$\begin{aligned} \mathrm{I}^n f(t) &= \int_a^t \mathrm{d}t_{n-1} \int_a^{t_{n-1}} \mathrm{d}t_{n-2} \ldots \int_a^{t_1} f(t_0)\,\mathrm{d}t_0 = \\ &= \frac{1}{(n-1)!} \int_a^t (t-\tau)^{n-1} f(\tau)\,\mathrm{d}\tau, \end{aligned} \tag{2.1}$$

with $a < t < b$, $n \in \mathbb{N}$. With the use of the Euler's Gamma function, Eq. 2.1 can be extended to calculate any positive real fractional order α Riemann-Liouville integral:

$$ {}^{\mathrm{RL}}_{\ a}\mathrm{I}^{\alpha}_{t} f(t) = \frac{1}{\Gamma(\alpha)} \int_a^t (t-\tau)^{\alpha-1} f(\tau)\,\mathrm{d}\tau, \tag{2.2} $$

with $a < t < b$, $\alpha \in \mathbb{R}_+$. For functions n times differentiable with $\Re(\alpha) < n$, repeated integration by parts yields

$$ {}_{a}\mathrm{I}^{\alpha}_{t} f(t) = \sum_{k=0}^{n-1} \frac{(t-a)^{\alpha+k} f^{(k)}(a)}{\Gamma(\alpha+k+1)} + {}_{a}\mathrm{I}^{\alpha+n}_{t} f^{(n)}(t). \tag{2.3} $$

Applying Eq. 2.3 to the definition of Riemann-Liouville integral, Eq. 2.2, the following alternative expression may be obtained [Oldham and Spanier, 1974; Podlubny, 1999; Riesz, 1949]:

$$ {}^{\mathrm{RL}}_{\ a}\mathrm{I}^{\alpha}_{t} f(t) = \sum_{k=0}^{n-1} \frac{(t-a)^{\alpha+k} f^{(k)}(a)}{\Gamma(\alpha+k+1)} + \frac{1}{\Gamma(\alpha+n)} \int_a^t (t-\tau)^{\alpha+n-1} f^{(n)}(\tau)\,\mathrm{d}\tau. \tag{2.4} $$

In order to obtain the Riemann-Liouville fractional differential (or derivative) operator, property 6 (see Appendix B.2) may be used, which yields

$$ {}^{\mathrm{RL}}_{\ a}\mathrm{D}^{\alpha}_{t} f(t) = \mathrm{D}^{n}_{t} \left({}^{\mathrm{RL}}_{\ a}\mathrm{I}^{n-\alpha}_{t} f(t) \right) = \frac{1}{\Gamma(n-\alpha)} \frac{\mathrm{d}^n}{\mathrm{d}t^n} \left(\int_a^t (t-\tau)^{n-\alpha-1} f(\tau)\ \mathrm{d}\tau \right), \tag{2.5} $$

with $n \in \mathbb{N}$ such that $0 < n-1 < \alpha \leq n$, that is, n is the smallest positive integer greater or equal to α and D^n is the ordinary differential operator. Again, under the same conditions previously established for fractional integrals, by perfoming repeatedly integration by parts, the following expression is obtained:

$$ {}^{\mathrm{RL}}_{\ a}\mathrm{D}^{\alpha}_{t} f(t) = \sum_{k=0}^{n-1} \frac{(t-a)^{k-\alpha} f^{(k)}(a)}{\Gamma(k-\alpha+1)} + \frac{1}{\Gamma(n-\alpha)} \int_a^t (t-\tau)^{n-\alpha-1} f^{(n)}(\tau)\,\mathrm{d}\tau. \tag{2.6} $$

As it may be observed, this last relation coincides with Eq. 2.4 when substituting negative values of α into it, taking into account the fact that $\mathrm{I}^{-\alpha} = \mathrm{D}^{\alpha}$.

In general, within the applications covered in this work $0 \leq \alpha \leq 1$, then $n = 1$

and Eq. 2.5 gives the following definition of the Riemann-Liouville fractional derivative:

$$ {}^{\mathrm{RL}}_{a}\mathrm{D}^{\alpha}_{t} f(t) = \mathrm{D}^{1}_{t}\left({}^{\mathrm{RL}}_{a}\mathrm{I}^{1-\alpha}_{t} f(t)\right) = \frac{1}{\Gamma(1-\alpha)}\frac{\mathrm{d}}{\mathrm{d}t}\left(\int_a^t (t-\tau)^{-\alpha} f(\tau)\,\mathrm{d}\tau\right) \tag{2.7} $$

provided that $f(t) \in \mathcal{C}^1[a,b]$.

Alternativelly, substituting $n = 1$ in Eq. 2.6 leads to

$$ {}^{\mathrm{RL}}_{a}\mathrm{D}^{\alpha}_{t} f(t) = \frac{(t-a)^{-\alpha} f(a)}{\Gamma(1-\alpha)} + \frac{1}{\Gamma(1-\alpha)}\int_a^t (t-\tau)^{-\alpha}\left(\frac{\mathrm{d}f(\tau)}{\mathrm{d}\tau}\right)\mathrm{d}\tau. \tag{2.8} $$

These relations will be used subsequently to produce numeric algorithms for Riemann-Liouville fractional integro-differential operators. It is apparent that Riemann-Liouville operators are also non-local, since their value at time t depends on the whole history of the kernel function $f(\tau)$. The storage of all the values $f(\tau)$ along time $t \in [a,t]$ is needed. This fact is one of the main drawbacks of fractional operators, as they require more and more data-storage as time progresses.

R-L algorithms

The R-L-algorithms are based on the Rieman-Liouville definition of integro-differentials. The R-algorithms are used for fractional integration and the L-ones for fractional differentiation. These latter ones are subsequently described since they are the ones used in this work.

For fractional derivatives, Eq. 2.8 with $a = 0$ may be rewritten as

$$ {}^{\mathrm{RL}}_{a}\mathrm{D}^{\alpha}_{t} f(t) = \frac{t^{-\alpha} f(0)}{\Gamma(1-\alpha)} + \frac{1}{\Gamma(1-\alpha)}\int_0^t \tau^{-\alpha}\left(\frac{\mathrm{d}f(t-\tau)}{\mathrm{d}\tau}\right)\mathrm{d}\tau, \tag{2.9} $$

which may be transformed into a summation as

$$ {}^{\mathrm{RL}}_{a}\mathrm{D}^{\alpha}_{t} f(t) = \frac{t^{-\alpha} f(0)}{\Gamma(1-\alpha)} + \frac{1}{\Gamma(1-\alpha)}\sum_{j=0}^{N-1}\int_{j\frac{t}{N}}^{(j+1)\frac{t}{N}} \tau^{-\alpha}\left(\frac{\mathrm{d}f(t-\tau)}{\mathrm{d}\tau}\right)\mathrm{d}\tau. \tag{2.10} $$

The L1-algorithm is constructed by backwards discretisation of the derivative within the integral in Eq. 2.10:

$$\int_{j\frac{t}{N}}^{(j+1)\frac{t}{N}} \tau^{-\alpha} \left(\frac{\mathrm{d}f(t-\tau)}{\mathrm{d}\tau}\right) \mathrm{d}\tau \approx \frac{f\left(t-j\frac{t}{N}\right) - f\left(t-(j+1)\frac{t}{N}\right)}{t/N} \int_{j\frac{t}{N}}^{(j+1)\frac{t}{N}} \tau^{-\alpha}\, \mathrm{d}\tau, \tag{2.11}$$

which, after integration and manipulation, finally yields the L1-algorithm for fractional derivatives of order α with $0 \leq \alpha < 1$:

$$\begin{aligned} {}^{\mathrm{L1}}_{0}\mathrm{D}^{\alpha}_{t} f(t) = & \frac{(t/N)^{-\alpha}}{\Gamma(2-\alpha)} \left[\frac{1-\alpha}{N^{\alpha}} f(0) + \right. \\ & \left. \sum_{j=0}^{N-1} \left[f\left(t - j\frac{t}{N}\right) - f\left(t-(j+1)\frac{t}{N}\right)\right] \left[(j+1)^{1-\alpha} - j^{1-\alpha}\right]\right]. \end{aligned} \tag{2.12}$$

For higher orders of the fractional derivative order α, numerical algorithms may be developed in a similar way but they will not be covered in this work as the fractional orders of interest in the applications analysed lie within the range $0 \leq \alpha < 1$.

Regarding the error induced by numerical discretisation of Riemann-Liouville integro-differential operators, it generally depends on the values of α and N. It tends to zero as N approaches infinity.

2.6 Conclusions

In this chapter, the scientific and technological framework of the mechanical behaviour of SRCs and SRCs-based FMLs is presented. Firstly, the origin and evolution of FMLs is related. Secondly, the low-velocity impact behaviour of FLMs depending on the constituent materials is shown. Then, SRCs are presented as alternative composite material and the research works on mechanical behaviour of SRCs-based FMLs are reviewed. Finally, the main trends concerning the modelling of composite materials, including SRCs, are described.

According to the introduction, as it happened with composite materials, the inclusion of FMLs in Automotive Industry seems to be feasible due to their enhanced specific mechanical properties when compared to their composite constituents; however, their implementation would be limited by now to high class vehicles duo to the high manufacturing costs.

From the review of the impact behaviour of FMLs, it can be stated that since automotive parts are susceptible to impacts, specifically low-velocity impacts, the study of the low-velocity impact response is of great interest, being the strain-rate effect on the mechanical response of constituents an essential interest aspect. On the one hand, among the different metal constituents, aluminium and magnesium seem to be the most appropriates for impact applications thanks to their lightweight and impact behaviour; nevertheless, the suitability of one metal or the other varies depending at least on the composite constituent and the stacking configuration. On the other hand, there is no work comparing directly the low-velocity impact behaviour of any thermosetting matrix FML with that of its thermoplastic counterpart; however, the studies on high-velocity impact behaviour of FMLs have demonstrated that thermoplastic-based FMLs are more appropriate for impact applications due to enhanced energy dissipation capacity.

Concerning SRCs, their recyclability and improved impact behaviour, specifically, in respect of damage tolerance and post-impact integrity, in comparison with the rest of composites are their main attractions. Being SRPP the only commercialised all-polymer composite, there are other alternatives which deserve to be contemplated as composite constituent in FMLs. Regarding SRC-based FMLs, several studies have been undertaken, but there is no one focusing on their low-velocity impact.

Finally, the use of classical models to reproduce phenomena, such as hysteresis, associated in most of the cases to the viscous character of polymers, requires a relative big number of material parameters to obtain reasonable results. This suggests that the employment of fractional models is a more effective alternative which can be valid to model the behaviour of SRCs.

Chapter 3

Low-velocity impact behaviour of SRCs and SRC-based FMLs

This chapter is devoted to the low-velocity impact behaviour of SRCs and SRC-based FMLs. It is divided into two parts. In the first one, the impact response of three different SRCs is studied in order to determine the most appropriate in terms of their energy dissipation capacity under low-velocity impacts. In the second one, two different FMLs, one based on aluminium and other based on magnesium, are manufactured by using the SRC previously chosen. Then, their low-velocity impact response is analysed in detail to elucidate which alternative presents the highest energy dissipation capacity.

3.1 Low-velocity impact behaviour of SRCs

3.1.1 Materials

Three different SRCs are studied in this part; a SRPP, a SRPET and a SRPE. All of them consist of a thermoplastic polymer fibre 0°/90° woven reinforcement embedded in a same-polymer matrix. They were supplied by Propex$^{\mathrm{TM}}$, Comfil$^{\mathrm{TM}}$ and Kaypla$^{\mathrm{TM}}$, respectively, being the SRPP commercialised under the trade name of Curv® and the others with the enterprise name. Their mechanical properties, provided by the manufacturers, are shown in Table 3.1.

Table 3.1: Mechanical properties of the SRPP [Pro, 2015], SRPET [Com, 2015] and SPPE.

	SRPP		SRPET		SRPE	
	1-Direc.	2-Direc.	1-Direc.	2-Direc.	1-Direc.	2-Direc.
Elastic modulus [GPa]	4.2	4.2	5.4	5.0	20.0	20.0
Yield stress [MPa]	120	120	192	159	–	–
Strain to faiulure [mm/mm]	0.20	0.20	0.24	0.24	–	–
Density [g/cm^3]	0.93		1.38		< 1	
Melting point [°C]	165		265		125	

3.1.2 Experimental procedure

Biaxial-bending impact tests

Low-velocity impact tests with different impact energies have been carried out on the SRCs by using a drop-weight machine. The machine, a Ceast 9350 model (Fractovis-Plus), was equipped with a 20 kN load cell attached to a 20 mm diameter hemispherical striker which measured contact force history. The selected impact height has been 500 mm for every test so that each material performs always with the same strain rate. The impact mass has been varied to establish specific impact energies. 80 mm × 80 mm square samples of 1 mm thick from plates of the three materials have been cut for the tests.

Energy profile method

The dissipated energy in an impact event versus impact energy is usually represented in a diagram called ‘energy profile’ (see Fig. 3.1). Such diagram is capable of revealing certain damage thresholds of composite materials and laminated structures [Feraboli and Kedward, 2006]. The energy profile presents a diagonal line (equal energy line) which indicates the maximum dissipated energy for an impact. Commonly, three regions can be distinguished in an energy profile diagram. Region (I) represents a stage in which the specimen is not penetrated. In that region, the curve is below the equal energy line, so dissipated energy is lower than impact energy. The energy excess is used to make the striker rebound from the sample at the end of the impact event. At the upper limit of Region

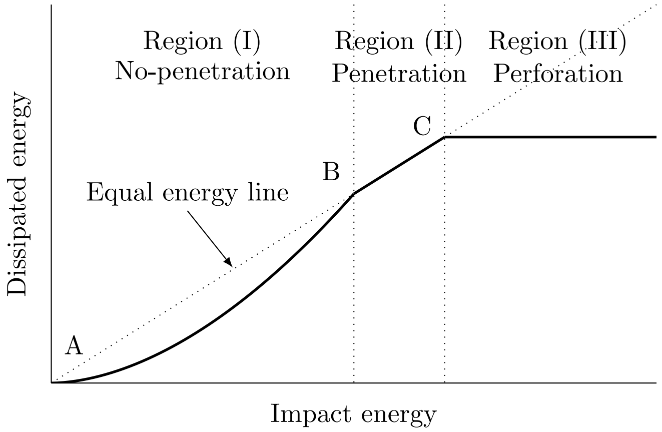

Figure 3.1: General scheme of an energy profile divided into the Region (I), Region (II) and Region (III), which correspond to the no-penetration, the penetration and the perforation phases, respectively.

(I) the penetration threshold (point B) is defined; in this point the dissipated energy equals the impact energy for the first time. Then, Region (II), known as penetration range, starts. In this stage the whole impact energy is dissipated by the sample. Normally, in this energy range the striker sticks into specimens and does not rebound any more [Aktas et al., 2009; Feraboli and Kedward, 2006]. Finally, in Region (III) the specimen is always perforated; the dissipated energy remains constant and corresponds to the perforation threshold, located at the beginning of such region (point C). As a consequence of the randomness of the damage caused by penetration, a slight dispersion of the value of dissipated energy may occur in Region (III). Hence, the average value of the impact energy in that region is taken as perforation threshold.

3.1.3 Results

Self-reinforced polypropylene, SRPP

Fig. 3.2 shows force-time corresponding to different damage stages of the SRPP and Fig. 3.2(b) its energy profile. The onset of fibre breakage (OFB) has been detected for a 30 J energy impact and perforation threshold has been detected at 44 J. Fig. 3.3 shows images of the impacted SRPP samples corresponding to the 6 J, 30 J and 60 J force-time curves and showing different damage stages.

According to the images, permanent deformation, already present for 6 J energy impact, increases with impact energy. Fibres breakage starts at 30 J and spreads through the thickness until perforation takes place at 44 J.

Self-reinforced poly(ethylene terephthalate), SRPET

Fig. 3.4(a) shows force-time corresponding to different damage stages of the SRPET and Fig. 3.4(b) its energy profile. The OFB has been detected for 18 J energy impact and perforation threshold has been detected at 23.5 J. Fig. 3.5 shows images of the impacted SRPET samples corresponding to the 12 J, 18 J and 30 J cases. According to the images, damage phenomena happened sequentially and similarly to the SRPP.

Self-reinforced polyethylene, SRPE

Fig. 3.6(a) shows force-time corresponding to different damage stages of the SRPE and Fig. 3.6(b) its energy profile. The OFB and the perforation phenomena have been detected for a 90 J energy impact, i.e there has not been a progressive fibre breakage prior to the perforation; this has been catastrophic instead. Fig. 3.7 shows images of the impacted SRPE samples corresponding to the 20 J, 70 J and 90 J force-time curves and showing different damage stages. As can be seen, there is no fibre breakage before that the perforation takes place, just permanent deflection.

Based on the results above, it is raised the question about which SRC offers the most appropriate response under low-velocity impacts. On the one hand, the SRPE has demonstrated the higher capacity to dissipate impact energy; however, it has been observed some phenomena which cast doubt on the suitability of this SRC to manufacture FMLs for impact applications. It has shown much less bending stiffness than the SRPP and the SRPET, and it started to yield at relatively low energy impacts. Moreover, it is worth reminding that the original SRPE samples, of similar dimensions as the SRPP and SRPE ones, pulled into the holder during impacts in spite of being clamped. After performing the tests on the final dimensions SRPE samples, it has been detected that, even being

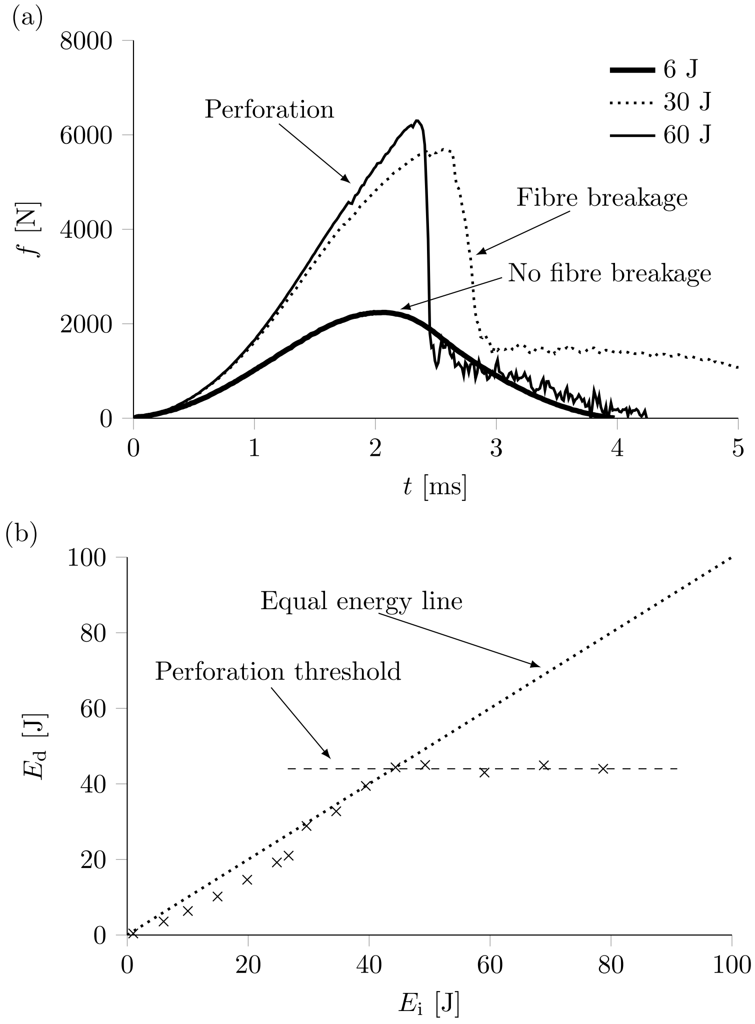

Figure 3.2: (a) Force-time curves corresponding to different damage stages of the SRPP and (b) its energy profile.

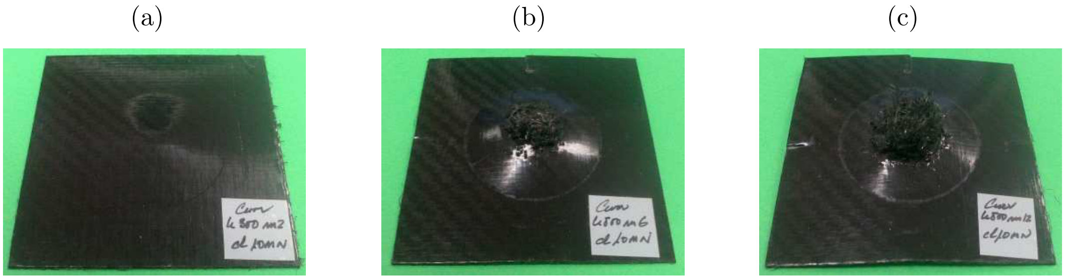

Figure 3.3: Images of impacted SRPP samples showing different damage stages; (a) permanent deformation for 6 J, (b) fibres breakage for 30 J and (c) perforation for 60 J.

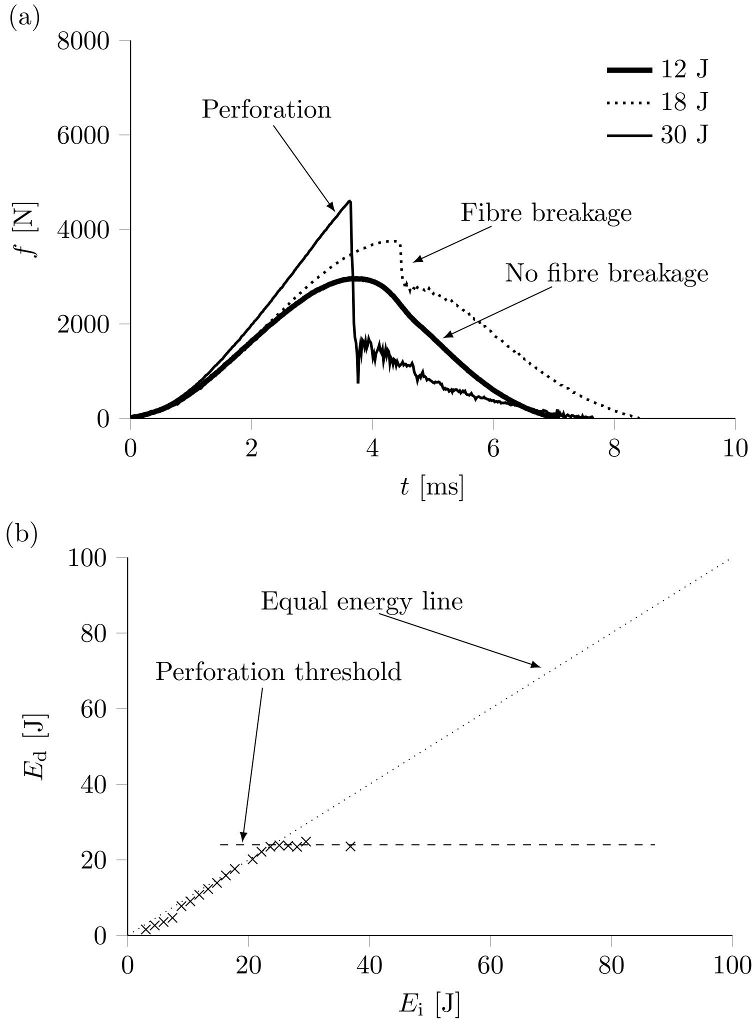

Figure 3.4: (a) Force-time curves corresponding to different damage stages of the SRPET and (b) its energy profile.

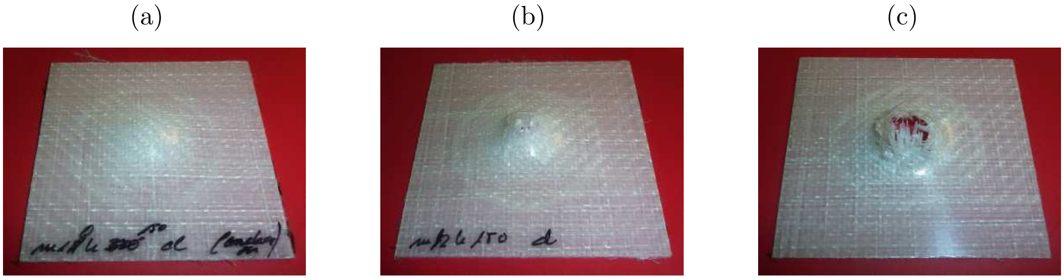
(a)
(b)
(c)

Figure 3.5: Images of impacted SRPET samples showing different damage stages; (a) permanent deformation for 12 J, (b) fibres breakage for 18 J and (c) perforation for 30 J.

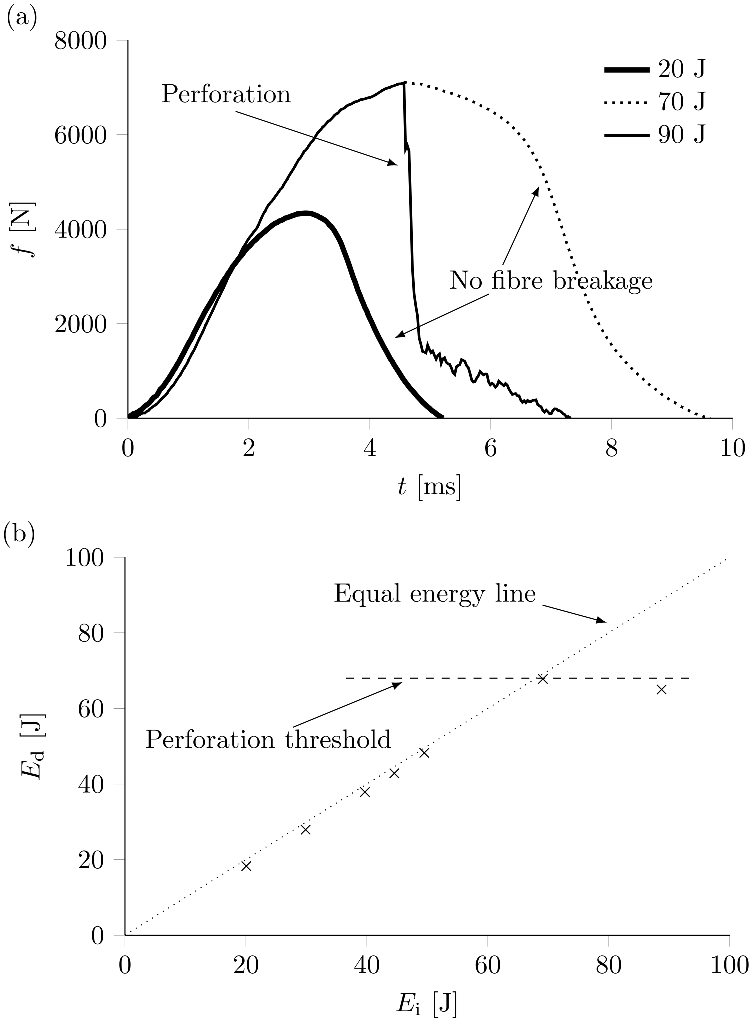

Figure 3.6: (a) Force-time curves corresponding to different damage stages of the SRPE and (b) its energy profile.

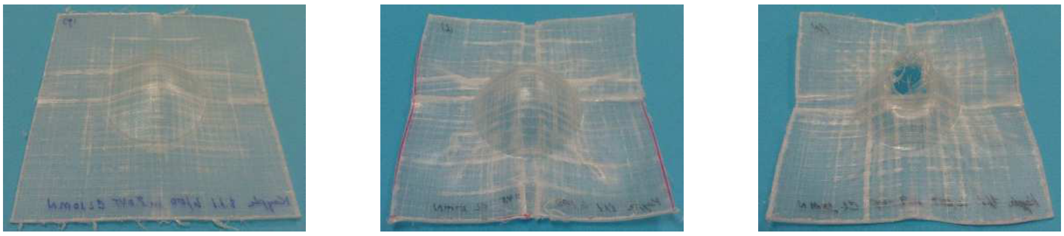
(a) (b) (c)

Figure 3.7: Images of impacted SRPE samples showing different damage stages; (a) permanent deformation for 20 J and (b) 70 J (close to perforation) and (c) perforation for 90 J.

larger, yield effects went over the clamped area. In fact, the deformation in plane was so large that a wrinkling phenomenon occurred. Such phenomenon is a consequence of an inappropriate (generally low) compaction temperature in the manufacturing process [Meerten et al., 2015]. On the other hand, the SRPP and the SRPET have qualitatively shown the same kind of response; nevertheless, quantitatively, the SRPP has shown almost twice penetration energy than the SRPET. These results suggest rejecting the SRPE as alternative for the FMLs and have demonstrated that the SRPP offers the most appropriate response under low-velocity impacts due to its capacity to dissipate impact energy at perforation.

3.2 Low-velocity impact behaviour of SRPP-based FMLs

3.2.1 Materials and manufacturing

Three different SRC-based FMLs have been studied; one with AZ31B-H24 magnesium and the other with 2024-T3 aluminium as metal constituent, and both with self-reinforced polypropylene (SRPP), selected in the previous section as composite constituent. Additionally, in the comparative study, a single SRPP of thickness similar to the FMLs' one is included as reference base material (provided also by Propex^{TM} and from now on referred to as 2.7-SRPP). Table 3.2 summarizes the thicknesses of the laminates and their constituents. A 2-1 stacking configuration was employed for both FMLs: [metal, SRPP]$_s$. The orientation of the layers is such that the metal's rolling and the composite's 0° directions coincides. The layers have been joined by using an interlayer adhesive consisting on a maleic anhydride modified polypropylene hot melt film [col, 2015].

The FMLs have been manufactured by hot pressing. Firstly, SRPP layers, interlayer adhesive films and metal sheets have been stacked according to the above configuration. Secondly, the laminate has been pressed (30 bar) using a mechanical press with hot plates at 165 °C; this temperature is less than SRPP's melting point and the minimal bondline temperature for the adhesive to melt and run

Table 3.2: Thicknesses of the constituents as received and total thicknesses of the laminates obtained after processing. Units are in millimetres.

	SRPP	Metal sheet	Adhesive	Total thickness
Mg-FML	0.63	0.42	0.06	2.28
Al-FML	0.63	0.41	0.06	2.26
2.7-SRPP	2.70	–	–	2.70

properly in operating status. Once the adhesive has been melted, the hot plates have been cooled at a rate of 10 °C/min until the temperature has dropped below 100 °C to assure the adhesive curing. Finally, the laminates have been removed from the press and cooled at room temperature. With this process, 250 mm × 250 mm square plates have been manufactured.

3.2.2 Experimental procedures

Tensile tests

Quasi-static tensile tests on the FMLs and the 2.7-SRPP have been performed to determine their mechanical properties. Five repetitions of each test have been performed at a strain rate of 10^{-3} s^{-1} and the strain has been measured with a 50 mm long extensometer. For this, the FMLs samples have been cut by water jet according to metal's rolling and composite's 0° directions (ASTM E8M-00 standard), whereas for the 2.7-SRPP, 20 mm × 200 mm rectangular samples have been cut.

Biaxial-bending impact tests

Low-velocity impact tests with different impact energies have been carried out on the SRC-FMLs by using the same drop-weight machine employed for the impacts on the SRCs. FML samples were 60 mm diameter circular plates, whereas SRPP samples were 80 mm × 80 mm square plates. The impact mass has been varied from 0.1 to 45.045 kg and the impact height has been kept constant at 500 mm (3.13 m/s) to avoid strain rate dependence of the mechanical response. The testing procedure has consisted in performing impacts with 0.5 J increments for each material and correlating events in the registered force-time curves with images of impacted specimens obtained with a macroscope. In this way, the failure energy for cracking of metal sheet (refers to as 'first cracking' for the non-impacted side (non-IS) and 'second cracking' for the impacted side (IS)), onset of fibre breakage (OFB) in the composite constituent and total perforation of the laminate have been identified.

The impact responses have also been studied by means of peak force and central deflection of the samples. The central deflection has been obtained by successive integrations of the acceleration signal obtained from the measured force-time curve. The permanent deflection has been measured directly from samples by using a dial gauge and the elastically recovered deflection has been obtained calculating the difference between maximum deflection and permanent deflection. Besides, the 'energy profile' method, described in Section 3.1, has been used to identified the no-penetration, penetration and perforation regions.

3.2.3 Results

Tensile tests

Tensile stress-strain response of materials, together with fracture toughness, has been used by different authors as a tool to estimate their impact energy dissipation capability [Pärnänen et al., 2012]. Fig. 3.8 shows the stress-strain curves of the FMLs and the 2.7-SRPP, and Table 3.3 collects their mechanical properties, deduced from the curves, as well as those of the metal sheets and the adhesive, provided by the manufacturers. According to Table 3.3, the Al-FML has higher mechanical properties than the Mg-FML. Moreover, the toughness of 2024-T3 is higher than that of AZ31B-H24 [Alderliesten et al., 2008]. Thus, the results suggest that the Al-FML would offer higher capacity to dissipate impact energy than the Mg-FML. However, impact properties of FMLs are generally expressed in specific values in order to consider the material weight. In this case, the Mg-FML implied a weight reduction of 21% when compared to its aluminium counterpart.

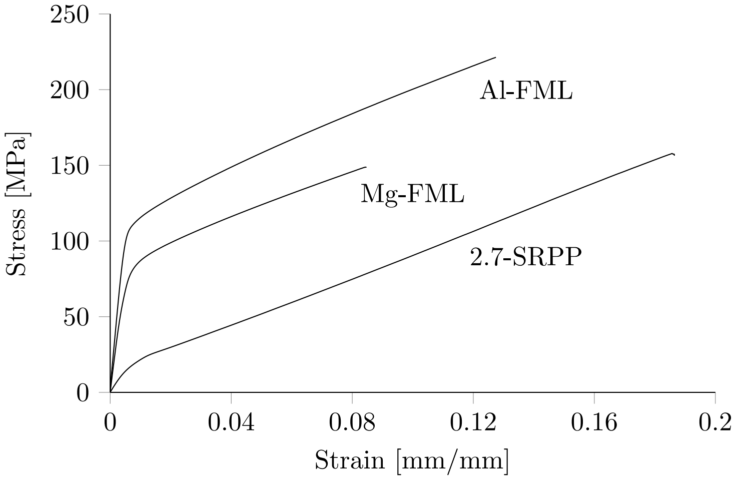

Figure 3.8: Quasi-static tensile stress-strain curves of the FMLs and the 2.7-SRPP composite.

Table 3.3: Mechanical properties of the metal sheets (aluminium [alu, 2015], magnesium [mag, 2015]), the adhesive [col, 2015], the FMLs and the 2.7-SRPP composite.

	Density [g/cm^3]	Elastic modulus [GPa]	Yield stress [MPa]	Maximum Strength [MPa]	Strain to failure [mm/mm]
Aluminium	2.70	73.1	288	436	0.164
Magnesium	1.78	50.7	207	275	0.095
Adhesive	0.92	0.5	–	25	6.000
SRPP/2.7-SRPP	0.92	3.24 ± 0.02	–	187 ± 2	0.171 ± 0.001
Mg-FML	1.24	15.7 ± 0.01	78 ± 2	149 ± 3	0.085 ± 0.001
Al-FML	1.57	21.5 ± 0.01	105 ± 3	221 ± 4	0.127 ± 0.002

2.7-SRPP composite

Three damage stages have been identified in the 2.7-SRPP composite. In the first one, the samples have revealed permanent deformation, e.g. from 29.6 J to 59.0 J. The second one has started with OFB on the non-IS at 63.9 J; the higher the energy impact, the higher the thickness affected by the breakages. Finally, the perforation has been reached at 75.3 J. Accordingly, Fig. 3.9 shows the damage evolution, while Fig. 3.10(a) and Fig. 3.10(b) presents the corresponding force-time curves.

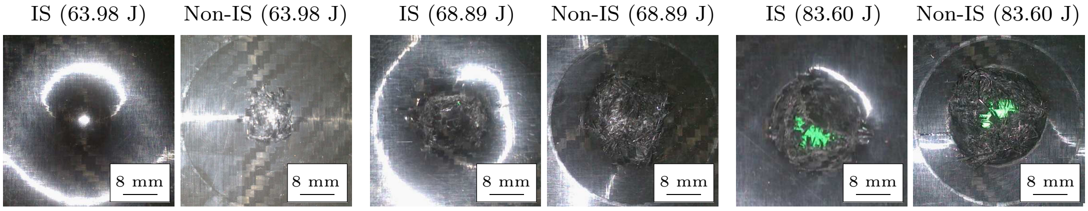

Figure 3.9: Images of the non-IS and the IS of the samples impacted with 63.9 J (OFB on the non-IS; end of the first stage), 68.9 J (partial fibre breakage through the whole section; belonging to the second stage) and 75.3 J (detection of the perforation threshold; end of the second stage) of the 2.7-SRPP composite.

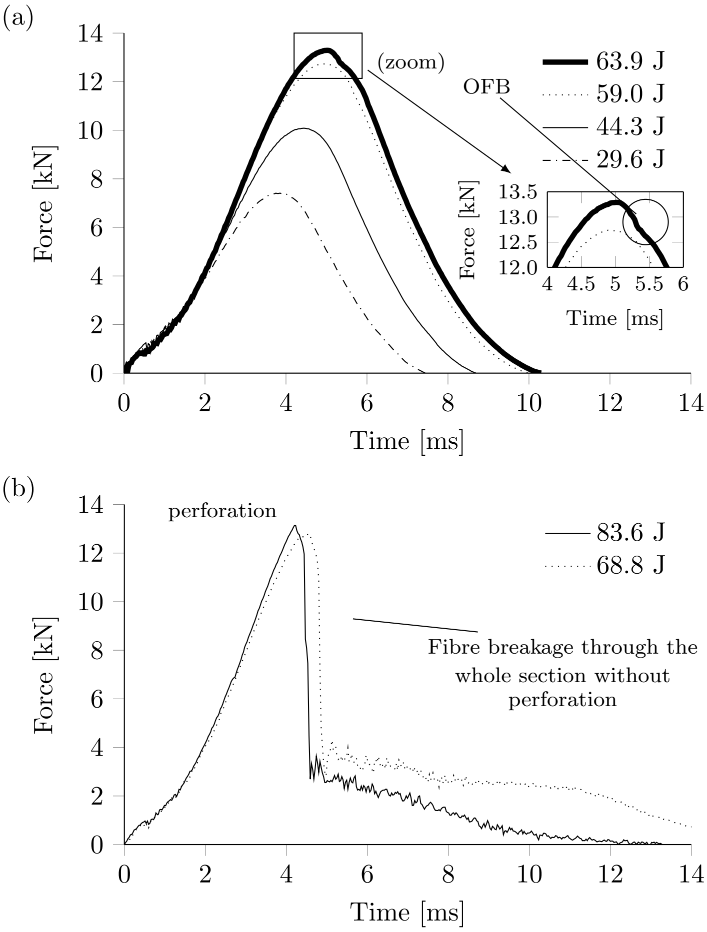

Figure 3.10: Force-time curves for different impact energies of the 2.7-SRPP; (a) belonging to the first stage which ended with the OFB and (b) one belonging to the second stage which suffered fibre breakage in the whole thickness and the other corresponding to the perforation thresholds.

Mg-FML

Four damage stages have been distinguished in the Mg-FML. Each stage has been initiated by a specific failure mode. Before detecting any of these failure modes, the FML has responded elastically, e.g. at 0.6 J (see Fig. 3.12a). The first failure mode, a permanent deflection associated to plasticity phenomenon, has been observed with a change in the slope of the force-time curve at approximately 1200 N, e.g. at 6.0 J (see Fig. 3.12a). Then, the first and second cracking, the OFB and the perforation have progressively led to other three damage stages at 10.0 J, 19.8 J and 39.4 J, respectively (see Fig. 3.11). The first (on the non-IS) and the second cracking (on the IS), which have occurred simultaneously at 10.0 J and in the rolling direction (RD) (see Fig. 3.11), have been associated with a force drop at around 3500 N (see Fig. 3.12a). Then, the OFB has been also detected on both sides of the FML. On the non-IS, fibres have failed by tensile stress (see Fig. 3.13(a)) and, on the IS, fibres have been sheared by the lips of the crack when the striker dented the metal sheet (see Fig. 3.13(b)). Moreover, at 19.8 J the crack of the non-IS propagated and perpendicular ramifications were generated (Fig. 3.13a) and the crack of the non-IS has traced a hemi-circular path according to the shape of the hemispherical striker (see Fig. 3.13(b)). Increasing the impact energy, the cracks have continued propagating and while some fibres have been sheared because of the dent, the rest of the fibres have performed properly under tension until failure (see Fig. 3.12(b)). Finally, at 39.4 J the laminate has been fully perforated. Regarding the interlayer behaviour, the hot melt adhesive film has kept the magnesium sheets and the composite material joined in some regions

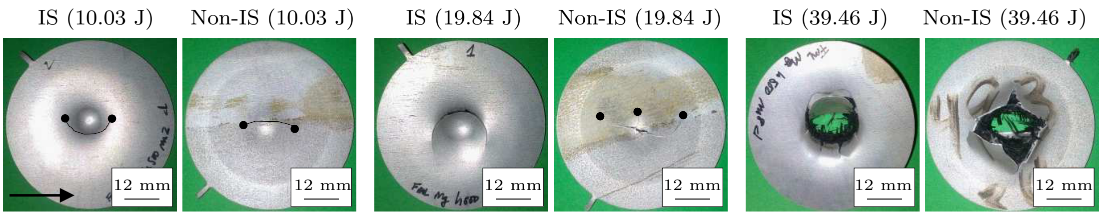
IS (10.03 J) Non-IS (10.03 J) IS (19.84 J) Non-IS (19.84 J) IS (39.46 J) Non-IS (39.46 J)

Figure 3.11: Images of the Mg-FML samples impacted with 10.0 J, 19.8 J and 39.4 J, corresponding to the first and second cracking (10.0 J), the OFB (19.8 J) and the perforation (39.4 J) (RD is indicated in the picture on the left and it is the same for all the samples).

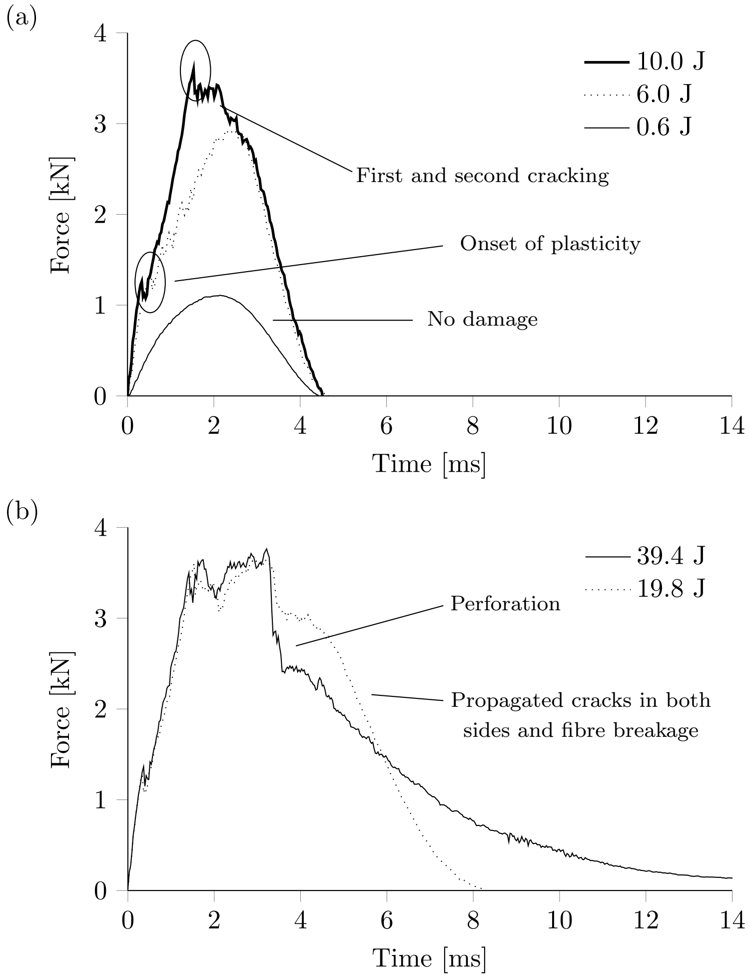

Figure 3.12: Force-time curves for different impact energy of the Mg-FML; (a) corresponding to responses with no damage, with plasticity (originate at 1200 N) as well as the first and second cracking and (b) corresponding to the OFB and the perforation.

of the impact area, forcing an intralayer failure in such regions. However, in some areas, the join between the substrates have failed, causing interlayer decohesion. In these parts the film has remained bonded to the composite (see Fig. 3.13(c)).

Al-FML

The same failure modes associated to the same damage stages of the Mg-FML have been identified in the Al-FML. The first and second cracking, the OFB and the perforation have been detected at 88.5 J, 108.1 J and 117.9 J, respectively (see

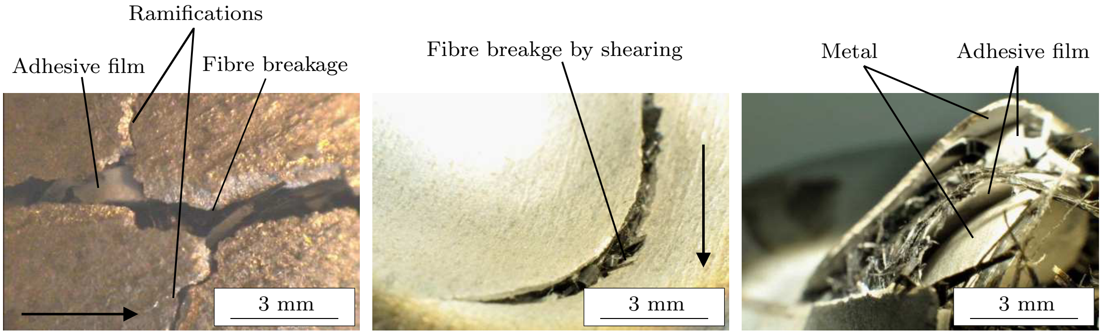

Figure 3.13: Macroscope images of the Mg-FML; (a) crack on the non-IS in presence of fibre breakage and ramifications at 19.8 J; (b) circular-shaped crack on the IS in presence of fibre breakage by shearing at 19.8 J; and (c) perforation region denoting composite-metal interlayer failure and showing a portion of adhesive bonded to the composite substrate at 39.4 J (the RD is indicated for the first two pictures).

Fig. 3.14). Fig 3.15a shows the different kinds of responses; an elastic response for 0.6 J, a response with presence of plasticity at 24.7 J and the corresponding to the first and second cracking moment, at 88.5 J. The change in the slope of the force-time curve which has announced the beginning of plasticity corresponds to approximately 1500 N (see Fig. 3.15a). The first (on the non-IS) and the second cracking (on the IS) have appeared in the RD (see Fig. 3.14) and caused a force drop after reaching the peak value (see Fig. 3.15a). The OFB has taken place in both sides of the FML at 108.1 J due to the tensile stress state produced throughout the thickness (see Fig. 3.15b). The cracks have defined hemi-circular paths (see Fig. 3.14) presenting a perpendicular ramification in the non-IS (see Fig. 3.16a) (see Fig. 3.16b). Finally, at 117.9 J the laminate has fully

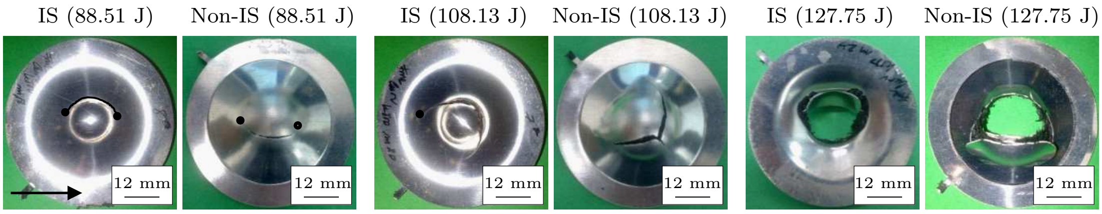

Figure 3.14: Images of the Al-FML samples impacted with 88.51 J, 108.13 J and 117.94 J, corresponding to the first and second cracking (88.5 J), the OFB (108.1 J) and the perforation (117.9 J) (the RD is indicated in the picture on the left and it is the same for all the samples).

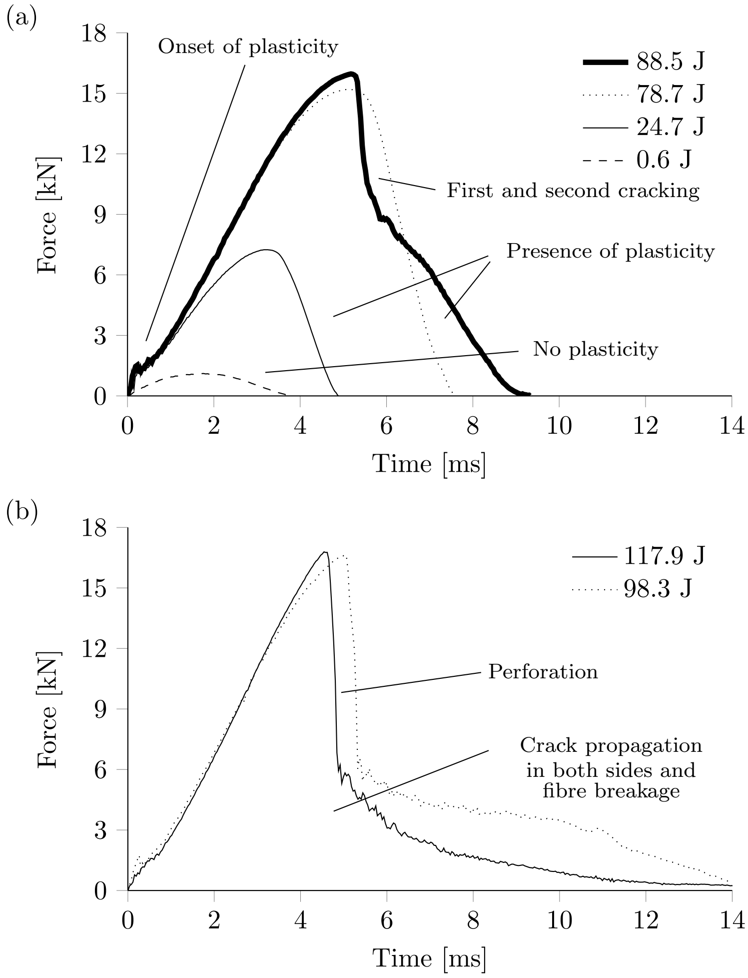

Figure 3.15: Force-time curves for different impact energy of the Al-FML; (a) corresponding to responses with no damage, with plasticity (originate at 1500 N) as well as the first and second cracking and (b) corresponding to the OFB and the perforation.

fully perforated. The hot melt adhesive film has kept the aluminium sheets and the composite material joined all over the region affected by the impact, forcing intralayer failure (see Fig. 3.16c).

Energy profile

Fig. 3.17 shows the energy profile of the Mg-FML (a) and the Al-FML (b). Neither Region (I) nor Region (II) can be distinguished for either laminates. The reason is that in both cases, for every impact below the perforation threshold,

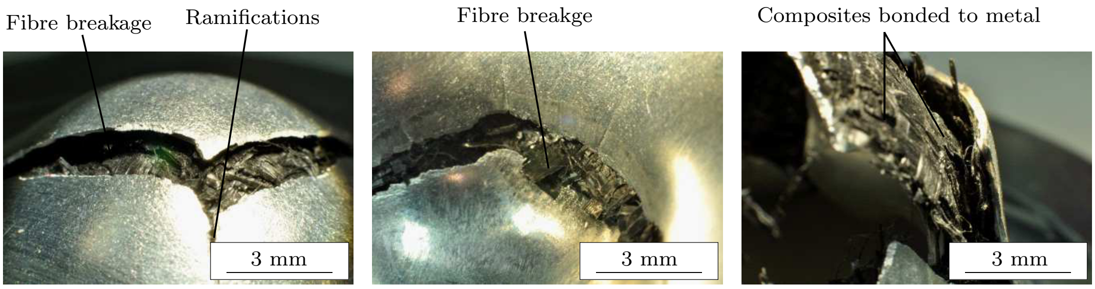

Figure 3.16: Macroscope images of the Al-FML; (a) crack on the non-IS in presence of fibre breakage by tensile and ramifications at 108.1 J; (b) circular-shaped crack on the IS in presence of fibre breakage at 108.1 J; and (c) perforation region with intralaminar failure at 117.9 J.

practically the whole impact energy has been dissipated by the samples making impossible the identification of their penetration thresholds. Thus, in order to distinguish their penetration thresholds, energy profiles have been represented in terms of the dissipated energy-impact energy ratio (see Fig. 3.18). Up to 30 J, the higher the impact energy, the higher the ratio as a consequence of the increasing plasticity in the constituents. At 30 J, the Mg-FML has reached a ratio of 1 (penetration threshold), whereas the ratio of the Al-FML has resulted 0.95. Later, the ratio of the Mg-FML has remained constant with a value of 1 until being perforated at approximately 40 J (according to Section 3.2.3), while the ratio of the Al-FML has not reached the value of 1 until 90 J. The penetration

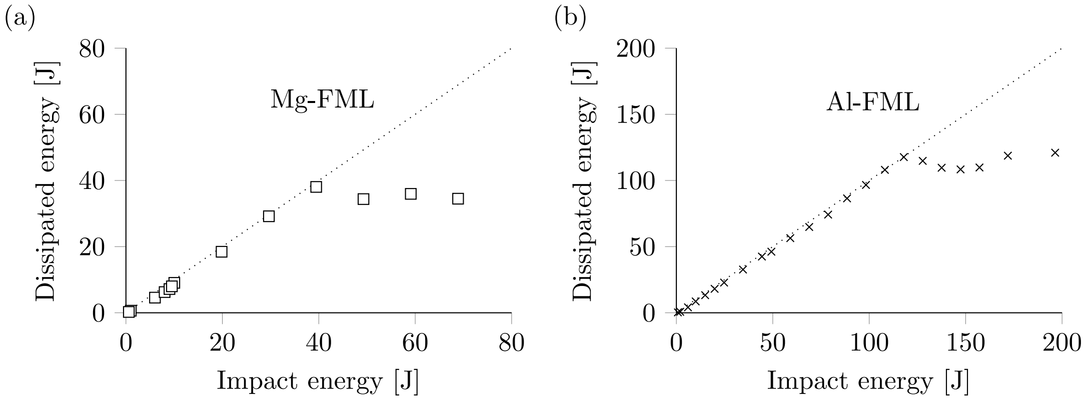

Figure 3.17: Energy profiles of (a) the Mg-FML and (b) the Al-FML. They enabled the identification of their perforation thresholds, but not of their penetration thresholds.

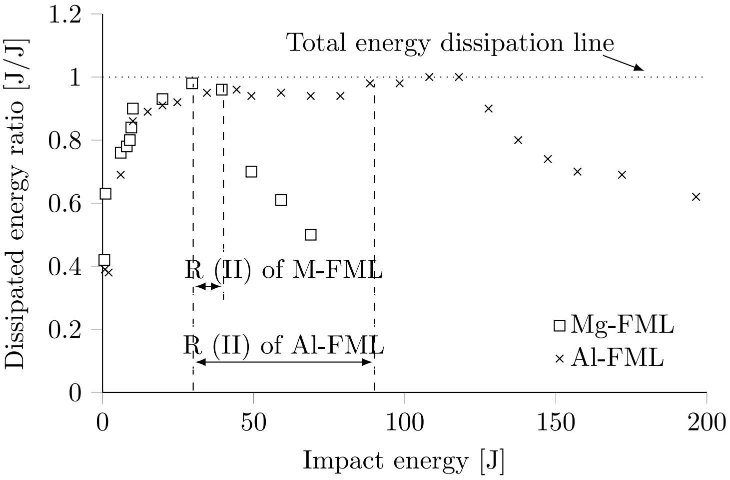

Figure 3.18: Dissipated energy ratio diagrams of the Mg-FML and the Al-FML.

threshold has been considered to be 30 J for that material. Finally, the profile of the Al-FML has established its perforation threshold at approximately 117 J. Concerning the 2.7-SRPP, the three regions were identified directly in the energy profile diagram. The penetration and the perforation thresholds were established at 63 J (OFB) and 75 J, respectively.

Peak force and central deflection

Fig. 3.19 shows the peak force evolution with impact energy for both the FMLs and the 2.7-SRPP. For the three materials peak force increased until any crack or breakage has taken place; first cracking in the Mg-FML (10 J) and Al-FML (88 J), and OFB in the 2.7-SRPP (63 J). From there on, the peak force has hardly varied until perforation. The peak force of the Al-FML has resulted approximately 4 times higher than that of the Mg-FML and 35% higher than that of the 2.7-SRPP composite.

The permanent central deflection data have been normalized by the highest value from among the three materials, corresponding to that of the Al-FML, just before perforation (see Fig. 3.20a). The recovered deflection has been represented as a percentage of the maximum deflection (see Fig. 3.20b). Below 10 J of impact energy, corresponding to the first cracking of the Mg-FML, both FMLs showed

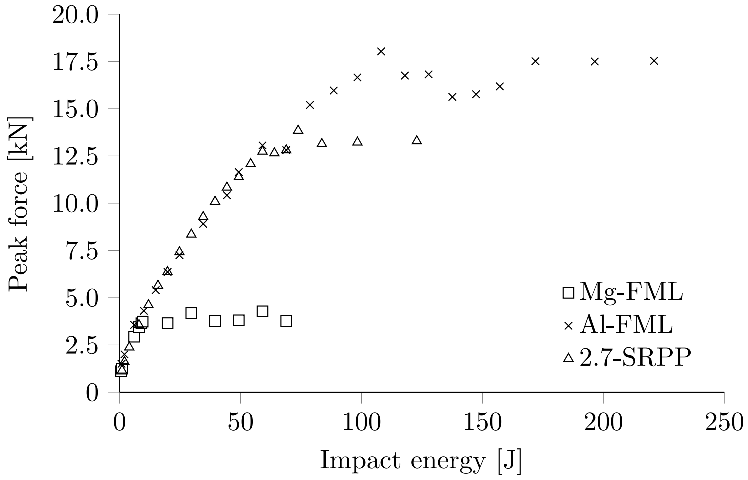

Figure 3.19: Peak force versus impact energy curves for the FMLs and the 2.7-SRPP.

almost the same permanent (see Fig. 3.20a) and recovered central deflection (see Fig. 3.20b). As an example, Fig. 3.21 shows the 6 J impact curves of both FMLs. Although the Mg-FML has reached a higher maximum deflection than the Al-FML because of its lower stiffness, it has also experienced a higher recovery of central deflection, resulting in the same permanent deflection. Beyond 10 J, whereas their permanent deflections have also resulted similar, the recovered deflection of the Mg-FML has been higher than that of the Al-FML, e.g. for 19 J (see Fig. 3.21). While the Al-FML has showed no damage, the Mg-FML has suffered the first and second cracking at around 3000 N. Once the cracking has started, the more the cracks propagated, the more the SRPP constituent was loaded. Finally, the unload slope of the Mg-FML has resulted less than that of the Al-FML because of the lower stiffness which has been reduced as a consequence of the damage caused in the magnesium sheets. Hence, the Mg-FML has experienced a higher deflection recovery when compared to the Al-FML, but they have suffered the same permanent deformation. For impact energies higher than 19 J, the recovered central deflection for Mg-FML has been 3 times higher than that of the Al-FML. This difference has been due to the SRPP which was the most decisive in the response of the laminate causing such elastic recovery, which in the case of the 2.7-SRPP is relatively significant (see Fig. 3.20b).

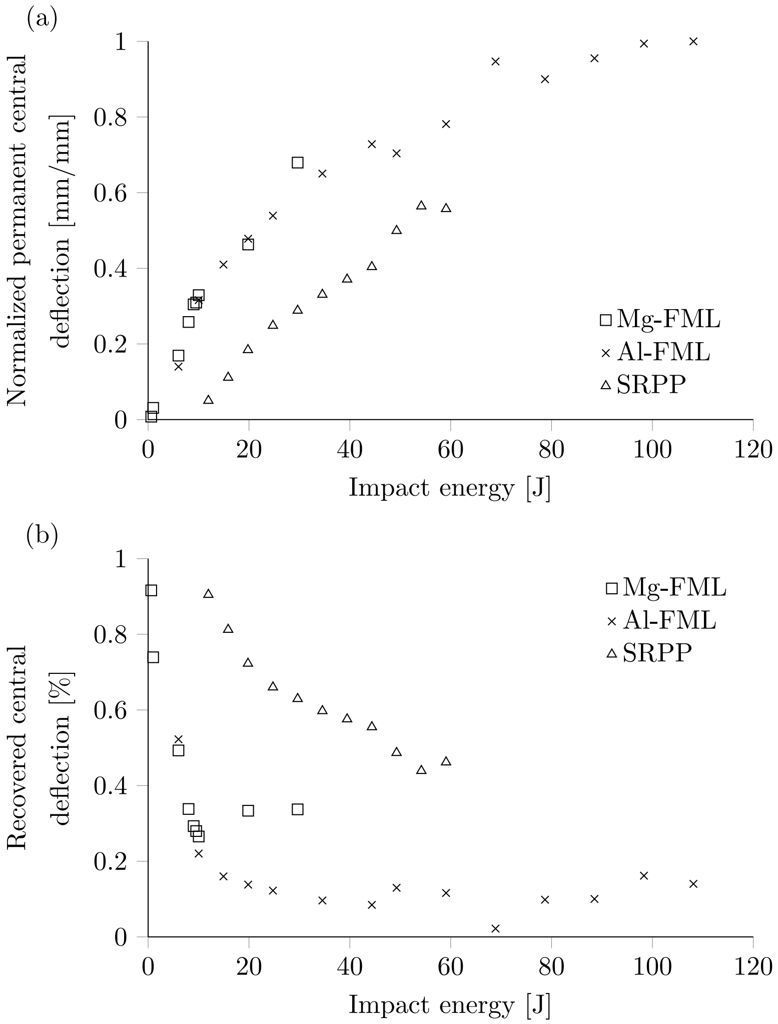

Figure 3.20: Normalized permanent central deflection (a) and recovered central deflection (b) versus impact energy of the materials.

3.2.4 Discussion

Table 3.4 summarizes the limit energies of the different failure modes and thresholds. The first and second cracking, as their names indicate, appeared sequentially for a specific force, suggesting that both laminates behaved as a membrane until such force. However, as Table 3.4 shows, the energy limit to generate the cracks for the Al-FML has resulted more than 8 times higher than that of the Mg-FML. The reason of such difference is attributed to the brittleness of magnesium in comparison with aluminium. When the magnesium sheet of the IS cracked and

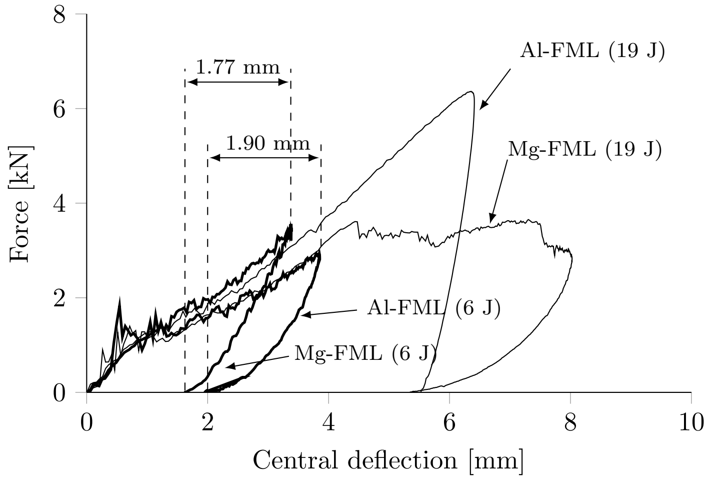

Figure 3.21: Force-central deflection curves of the Mg-FML and the Al-FML for the energy impacts of 6 J and 19 J.

started to shear fibres of the composite constituent, these fibres stopped working in tension making the rest of the fibres to be overloaded. The more the crack propagated and the dent penetrated, the higher the number of throughout-thickness sheared fibres, causing a reduction of the effective thickness working as a membrane. Moreover, the interlayer adhesion of the Mg-FML, which has resulted worse than that of the Al-FML, probably contributed to magnify the quantitative differences between the limit energies of their failure modes as well as the penetration and perforation thresholds. The peak force has also revealed significant differences as a consequence of the relatively early appearance of the first failure mode of the Mg-FML and its deficient interlayer adhesion. Values shown in Table 3.4 were normalized by their areal densities giving the values shown in Fig. 3.22. The specific perforation threshold for the Al-FML has resulted more than 2 times higher than that of the Mg-FML despite the weight reduction that the use of magnesium implies. In addition, the penetration range, where most of the energy is dissipated, has been in the Al-FML 8 times bigger than in Mg-FML. Moreover, the Al-FML has improved the impact resistance by 10% and showed an energy dissipation capacity around 5 times higher when compared to the 2.7-SRPP. The Mg-FML, also, offered the worst behaviour from a resistance and energy dissipation capacity point of view.

Table 3.4: Limit energies of the different thresholds and failure modes.

	1^{st} cracking [J]	2^{nd} cracking [J]	OFB [J]	Penetration [J]	Perforation [J]
Mg-FML	10.0	10.0	19.8	30.0	40.0
Al-FML	88.5	88.5	108.1	30.0	117.0
2.7-SRPP			63.9	63.9	75.3

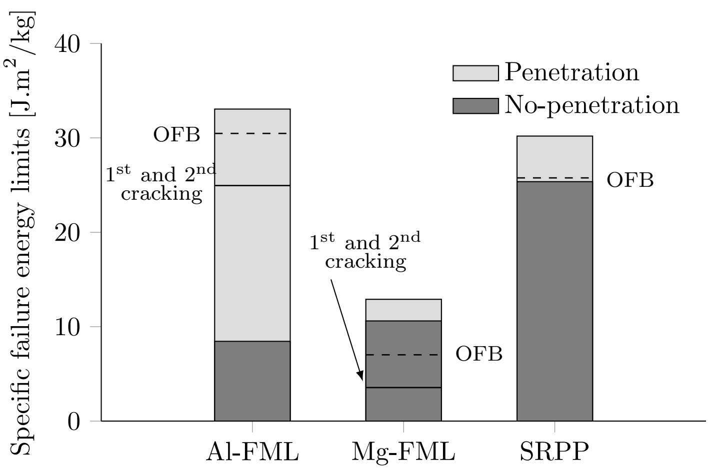

Figure 3.22: Quasi-static tensile stress-strain curves of the FMLs and the 2.7-SRPP composite.

3.3 Conclusions

In the first part of this chapter, three different SRCs have been studied; a SRPP, a SRPET and a SRPE. First of all, the SRPE has demonstrated the higher capacity to dissipate impact energy; however, its relatively low stiffness and trend to suffer wrinkling cast doubt on the suitability of this SRC to manufacture FMLs for impact applications. And, between the SRPP and the SRPET, it has been the former which has offered almost twice more penetration energy than the latter. Thus, the SRPP has been selected to manufacture SRPP-based FMLs.

In the second part of this chapter, two different SRPP-based FMLs have been studied; one with AZ31B-H24 magnesium and the other with 2024-T3 aluminium as metal constituent. The Al-FML has demonstrated a higher perforation resistance and capacity to dissipate energy impact than the Mg-FML. In fact, despite the latter presented a lower density than the former, the perforation threshold of the aluminium-based laminate has resulted more than twice than that of the aluminium-based one. Furthermore, the limit energy of the failure modes have suggested that the impact performance of these SRC-based laminates not only depends on the mechanical properties of metal and composite constituents, but also on the interaction between them when subjected to impact. Particularly, in the case of the Mg-FML, the brittleness of magnesium has produced the cracking of the IS sheets causing the shearing of fibres of the SRPP constituent, what reduced the effective thickness. Consequently, the potential that the laminate could offer when working as a membrane has assumed no advantage.

Also, the combination of SRPP with aluminium sheets can provide a FML which constitutes an improved alternative to the plain composite for impact applications. In this case, the Al-FML has proven to have higher impact resistance and capacity to dissipate impact energy when compared to the 2.7-SRPP composite. The Mg-based FML, otherwise, has resulted to have less impact resistance than the similar-thickness plain composite.

Chapter 4

Mechanical characterisation of SRPP and Al/SRPP-FML

This chapter deals with the mechanical characterisation of SRPP and Al/SRPP-FML. It is divided into two parts. In the first one, the mechanical behaviour of SRPP at different strain rates is characterised. It is also included an analysis of the stiffness evolution with strain and the hysteresis phenomenon associated to the viscous character of SRPP. In the second part, the mechanical response at different strain rates of Al/SRPP-FML is studied and the influence of SRPP as constituent material in the FML is evaluated.

4.1 Basic definitions

For both the mechanical characterisation and behaviour modelling of the plain composite, addressed this latter in Chapter 5, the coordinate system is composed of the first axe which corresponds to the warp direction and the second one, perpendicular to the first one, coincides with the weft direction in the case of balanced fabrics. The third axe is normal to the plane defined by the first and second directions, which coincides with the direction given by the thickness of the ply. Fig. 4.2 shows a general orthotropy reference frame (O, 123) with a clockwise rotation angle θ with respect to the global frame (O, xyz).

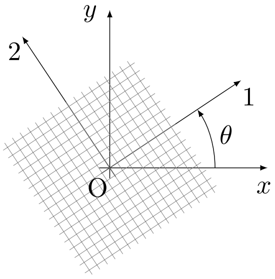

Figure 4.1: General orthotropy reference frame (O, 123) with a clockwise rotation angle θ with respect to the global frame (O, xyz).

In order to develop the theoretical models in Chapter 5 for the elementary ply, the stress is supposed to be plane, i.e. the stress σ_{33} is negligible. Furthermore, the strain and stress distributions within the thickness of the elementary ply are assumed to be uniform. The undamaged elastic stiffness matrix $\mathbf{C}^0$ is then defined as follows [Gay, 2005; Gornet and Ijaz, 2011; Herakovich, 1998]:

$$\mathbf{C}^0 = \begin{pmatrix} \dfrac{E_{11}}{1-\nu_{12}\nu_{21}} & \dfrac{\nu_{12}E_{22}}{1-\nu_{12}\nu_{21}} & 0 \\ \dfrac{E_{11}}{1-\nu_{12}\nu_{21}} & \dfrac{E_{22}}{1-\nu_{12}\nu_{21}} & 0 \\ 0 & 0 & 2G_{12} \end{pmatrix}, \tag{4.1}$$

where E_{11}, E_{22} and G_{12} are elastic constants and ν_{12} and ν_{21} are the Poisson's ratios of the material with

$$\frac{\nu_{12}}{E_{11}} = \frac{\nu_{21}}{E_{22}}. \tag{4.2}$$

In order to take into account the material degradation, based on the continuum damage mechanics approach, where the models are written at the homogenised mesoscale of the elementary ply [Hochard et al., 2001; Ladevèze, 1986, 1994], the elastic stiffness matrix $\mathbf{C}$ is

$$\begin{pmatrix} \dfrac{E_{11}^0(1-d_{11})}{1-\nu_{12}\nu_{21}} & \dfrac{\nu_{12}E_{22}}{1-\nu_{12}\nu_{21}} & 0 \\ \dfrac{E_{11}}{1-\nu_{12}\nu_{21}} & \dfrac{E_{22}^0(1-d_{22})}{1-\nu_{12}\nu_{21}} & 0 \\ 0 & 0 & 2G_{12}^0(1-d_{12}) \end{pmatrix}, \tag{4.3}$$

where E_{11}^0, E_{22}^0 and G_{12}^0 are undamaged elastic constants, d_{11} and d_{22} are respectively the damage variables in the warp and weft directions, and d_{12} the damage variable associated to the shear in direction 12. These may be gathered collectively into the damage variables vector $\mathbf{d} = [d_{11}, d_{22}, d_{12}]^{\mathrm{T}}$. Note that Poisson's ratio is assumed to experiment no degradation. In this case, eq. 4.2 takes the form:

$$\frac{\nu_{12}}{E_{11}^0} = \frac{\nu_{21}}{E_{22}^0}. \tag{4.4}$$

With the hypothesis of plane stress and according to a Voigt vectorial representation, the strain tensor in the orthotropy frame is related to the strain tensor in the global one as follows:

$$\left\{\begin{array}{c} \varepsilon_{11} \\ \varepsilon_{12} \\ 2\varepsilon_{12} \end{array}\right\} = \left(\begin{array}{ccc} \cos^2\theta & \sin^2\theta & \sin\theta\cos\theta \\ \sin^2\theta & \cos^2\theta & \sin\theta\cos\theta \\ -2\sin\theta\cos\theta & 2\sin\theta\cos\theta & \cos^2\theta - \sin^2\theta \end{array}\right) \left\{\begin{array}{c} \varepsilon_{xx} \\ \varepsilon_{yy} \\ 2\varepsilon_{xy} \end{array}\right\} \tag{4.5}$$

For the stress vector, the same relation is obtained:

$$\left\{\begin{array}{c} \sigma_{11} \\ \sigma_{12} \\ \sigma_{12} \end{array}\right\} = \left(\begin{array}{ccc} \cos^2\theta & \sin^2\theta & 2\sin\theta\cos\theta \\ \sin^2\theta & \cos^2\theta & 2\sin\theta\cos\theta \\ -\sin\theta\cos\theta & \sin\theta\cos\theta & \cos^2\theta - \sin^2\theta \end{array}\right) \left\{\begin{array}{c} \sigma_{xx} \\ \sigma_{yy} \\ \sigma_{xy} \end{array}\right\} \tag{4.6}$$

Eqs. 4.5 and 4.6 will be used in Section 4.2 and Section 4.2.2 in order to relate the global frame, associated to the test machine, and the orthotropy frame, associated to the fibres orientations.

For the study of the mechanical response of the FML, the coordinate system used is the one defined for the plain composite so that the rolling and transverse directions of the metal coincide with the warp and weft directions of the composite, respectively. As for the plain composite, the stress is supposed to be plane.

4.2 Experimental methodology

4.2.1 Characterisation methodology of the SRPP

The mechanical characterisation of the SRPP covers a study of quasi-static behaviour at different strain rates. In the particular case of balanced woven fabric composites, the longitudinal and transversal directions are assumed to have the same behaviour and damage evolution laws. Thus, the experimental campaign has consisted of the following tests:

- Quasi-static cyclic tensile tests on 1-direction oriented laminates.
- Quasi-static cyclic tensile tests on 45° oriented laminates.

It must be pointed out that, when performing cyclic tests, the number of cycles has been limited to 6 in order to remain in a domain where fatigue effects are negligible [Rozycki, 2000]. Besides, the stiffness variation with strain is analysed and its causes, which are attributed to damage generation Ladevèze [1986] and material stiffening phenomena [Galeski and Regnier, 2009; Holliday, 1971], are estimated y quantified.

Tensile tests have been performed following ASTM D638 standard [D63]. Fig. 4.11 shows the geometry and dimensions of the tensile test samples. The tests have been performed in an Instron 3369 universal test machine at 10^{-4} s^{-1}, 10^{-3} s^{-1} and 10^{-2} s^{-1}. For the load and longitudinal strain measurements, an Instron 2580-108 load cell and TML's YFLA-5 strain gauges have been used, respectively. Data acquisition has been achieved by an external National Instruments® system, which consists of a NI-9219 module mounted on a cDAQ-9178 chassis, and

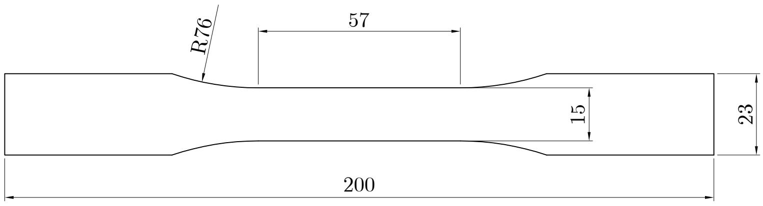

Figure 4.2: Sample geometry dimensioned according to ASTM D638 standard [D63].

LabView SignalExpress 2010 data acquisition software. The tests have been performed on 5 different samples and the properties have been established by the average values of these 5 tests.

Tests on 1-direction oriented laminates

In this case, the warp coincides with the direction in which the load is applied, i.e. the global longitudinal x direction, associated to the test machine. Thus, Eqs. 4.5 and 4.6 with $\theta = 0$ yield:

$$\sigma_{xx} = \sigma_{11} \tag{4.7}$$

$$\varepsilon_{xx} = \varepsilon_{11} \tag{4.8}$$

$$\varepsilon_{yy} = \varepsilon_{22} \tag{4.9}$$

Furthermore, if the orthotropy of the material is assumed, then $E_{11} = E_{22}$ and from eq. 4.2 it results:

$$\nu_{12} = \nu_{21} \tag{4.10}$$

The elastic behaviour law gives the following equations:

$$\sigma_{11} = E_{11}^{0}(1 - d_{11})\varepsilon_{11}^{\mathrm{e}}, \quad \sigma_{22} = 0, \quad \sigma_{12} = 0 \tag{4.11}$$

$$\sigma_{11} = -\frac{E_{11}^{0}}{\nu_{12}}\varepsilon_{22}^{\mathrm{e}} \tag{4.12}$$

Tests on 45° oriented laminates

In this case, the warp is rotated 45° with respect to the global longitudinal x direction, associated to the test machine. Thus, Eqs. 4.5 and 4.6 with $\theta = 45°$ yield:

$$\sigma_{12} = \frac{\sigma_{xx}}{2} \tag{4.13}$$

$$\varepsilon_{12} = -\frac{\varepsilon_{xx} - \varepsilon_{yy}}{2} \tag{4.14}$$

Stiffness evolution: damage and stiffening

The stiffness decrease is caused by damage generation, which in composite materials is associated to several phenomena such as fibre breakage, fibre-matrix debonding or matrix microcracking, depending on loading orientation [Ladevèze, 1986; Rozycki, 2000]. In semicrystalline polymers, another damage classes can be identified such as lamellar fragmentation and voids generation [Detrez et al., 2011]. Moreover, in these materials another phenomena implying the contrary effect, i.e a stiffness increase, can take place, e.g chains orientation [Galeski and Regnier, 2009; Holliday, 1971]. The stiffness increase caused by any phenomenon will be name stiffening.

As it will be seen, in a first stage the tensile stiffness of the SRPP decreases with the strain and, subsequently, a stiffness increase stage is initiated. Assuming an uniaxial case and defining the relation between the elastic modulus and the undamaged elastic modulus ζ as

$$\zeta = \frac{E}{E^0}, \tag{4.15}$$

the stress can be expressed by means of

$$\sigma = E^0 \zeta \varepsilon^{\mathrm{e}}. \tag{4.16}$$

Based on the approach of continuum damage mechanics (CDM) to model damage, it is proposed to reformulate the damage elastic law in order to include a new variable associated to stiffening by means of:

$$\sigma = E^0 (1-d)(1+r)\varepsilon^{\mathrm{e}}, \tag{4.17}$$

where r is the variable associated to stiffening. Equalling Eq. 4.16 and Eq. 4.17, it can be established that

$$\zeta = (1-d)(1+r) = 1 + r - d - dr = 1 - \underbrace{(d - r + dr)}_{R_{\mathrm{s}}} = 1 - R_{\mathrm{s}}, \tag{4.18}$$

where R_s is the stiffness variability ratio, which is defined as follows:

$$R_\mathrm{s} = 1 - \zeta = 1 - \frac{E}{E^0}. \tag{4.19}$$

Then, from Eq. 4.18 it can be deduced the following expression for the stiffening:

$$r = \frac{d - R_\mathrm{s}}{1 - d}. \tag{4.20}$$

Subsequently, an example of how to identify the damage and the stiffening is presented. It is assumed some random R_s data which evolves with the elastic strain (see Fig. 4.3) according to the trend that will be seen in Section 4.3. As Fig. 4.3 shows, initially, the stiffness variation ratio increases progressively from certain estimable elastic strain and, then, after reaching a maximum, it starts to decrease. This stiffness variation is caused by the damage and stiffening phenomena, which are coupled. Experimentally quantifying the influence of each phenomenon to such evolution would be of great difficulty [Stribeck, 2009], so in this research work a criterion to determine the contribution of them has been established. This criterion has been based on two hypothesises:

- The stiffening does not influence on the stiffness variability ratio until this later reaches its maximum, i.e the stiffness variability ratio is equal to the damage until then.

- The damage evolves exponentially, as it has been previously verified on most of semicrystalline polymers and composite materials [Detrez et al., 2010].

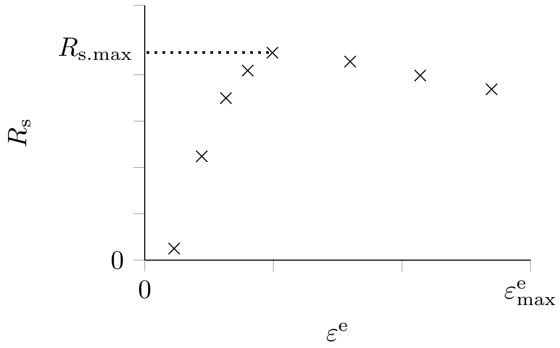

Figure 4.3: Evolution of the stiffness variation ratio with elastic strain.

Hence, to estimate the damage an exponential evolution curve is fitted to the R_s experimental data considering all points from the beginning to the maximum value $R_\text{s.max}$ (see Fig. 4.4(a)). Then, the stiffening is calculated by means of Eq. 4.20 resulting its evolution with elastic strain (see Fig. 4.4(b)).

4.2.2 Characterisation methodology of Al/SRPP-FML

In order to study of the mechanical response of the Al/SRPP-FML, two tensile tests at 10^{-4} s^{-1} and 10^{-2} s^{-1}, and a cyclic tensile test 10^{-3} s^{-1} have been performed. The tests have been performed in an Instron 3369 universal test machine. The data acquisition has been carried out in the same way that in the plain composite and the sample geometry used has been the corresponding to ASTM D638 standard [D63]. The aim of these tests is to evaluate the influence of the SRPP as constituent material in the FML.

4.3 Mechanical characterisation of the SRPP

4.3.1 1-direction tensile behaviour

Fig. 4.5 shows the 1-direction tensile behaviour obtained from the cyclic tensile tests on 1-direction oriented laminates at 10^{-4} s^{-1}, 10^{-3} s^{-1} and 10^{-2} s^{-1}. From

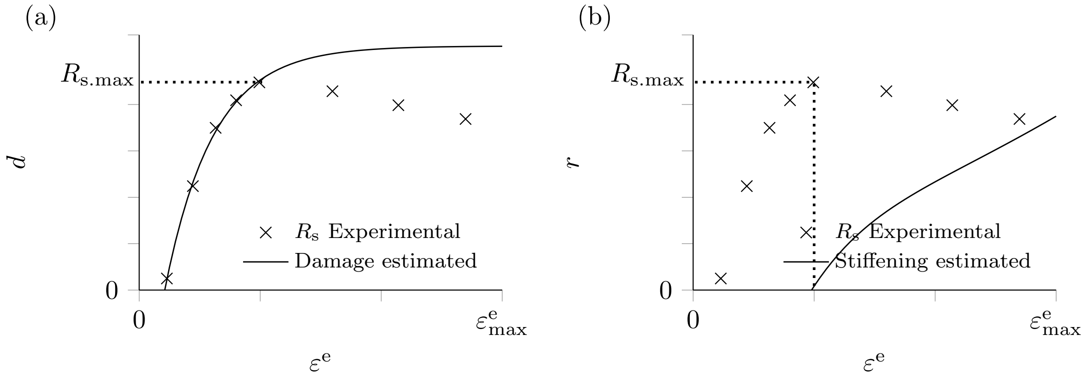

Figure 4.4: Evolution of the (a) damage estimated and the (b) stiffness from the stiffness variation ratio with elastic strain.

them, the following observations have been made:

- Existence of irreversible strains.
- Generation of non-symmetric hysteresis loops resulting from the load-unload cycles.
- Strain rate dependence.
- Variation of stiffness with the elastic strain at global scale.

Fig. 4.5 also shows that the strain rate effect is significantly perceptible not only in the hardening, but also in the accumulated irreversible strains and the shape of hysteretic loops. The higher the strain rate, the lower the irreversible strains and the thinner and taller the hysteretic loops. The undamaged elastic modulus E_{11}^0, obtained from the initial linear part of stress-strain curves within the range 2-6 MPa, is also affected by the strain rate (see Table 4.1). Concerning the stiffness, in a first stage it decreases with the strain and, subsequently, a increasing stage is initiated. All these aspects will be taken into account in the development of the tensile behaviour models in Chapter 5.

Fig. 4.6 shows the evolution of stiffness variability ratio R_s, defined in Section 4.6 (see Eq. 4.19), for the three strain rates. The stiffness decrease stage implies an increasing stiffness variability ratio and the subsequent stiffness increase stage implies a decreasing stiffness variability ratio.

Table 4.1: Undamaged elastic modulus depending on the strain rate.

	10^{-4} s^{-1}	10^{-3} s^{-1}	10^{-2} s^{-1}
E_{11}^0 [MPa]	4214.9±3.8	4284.7±5.8	4981.1±8.5

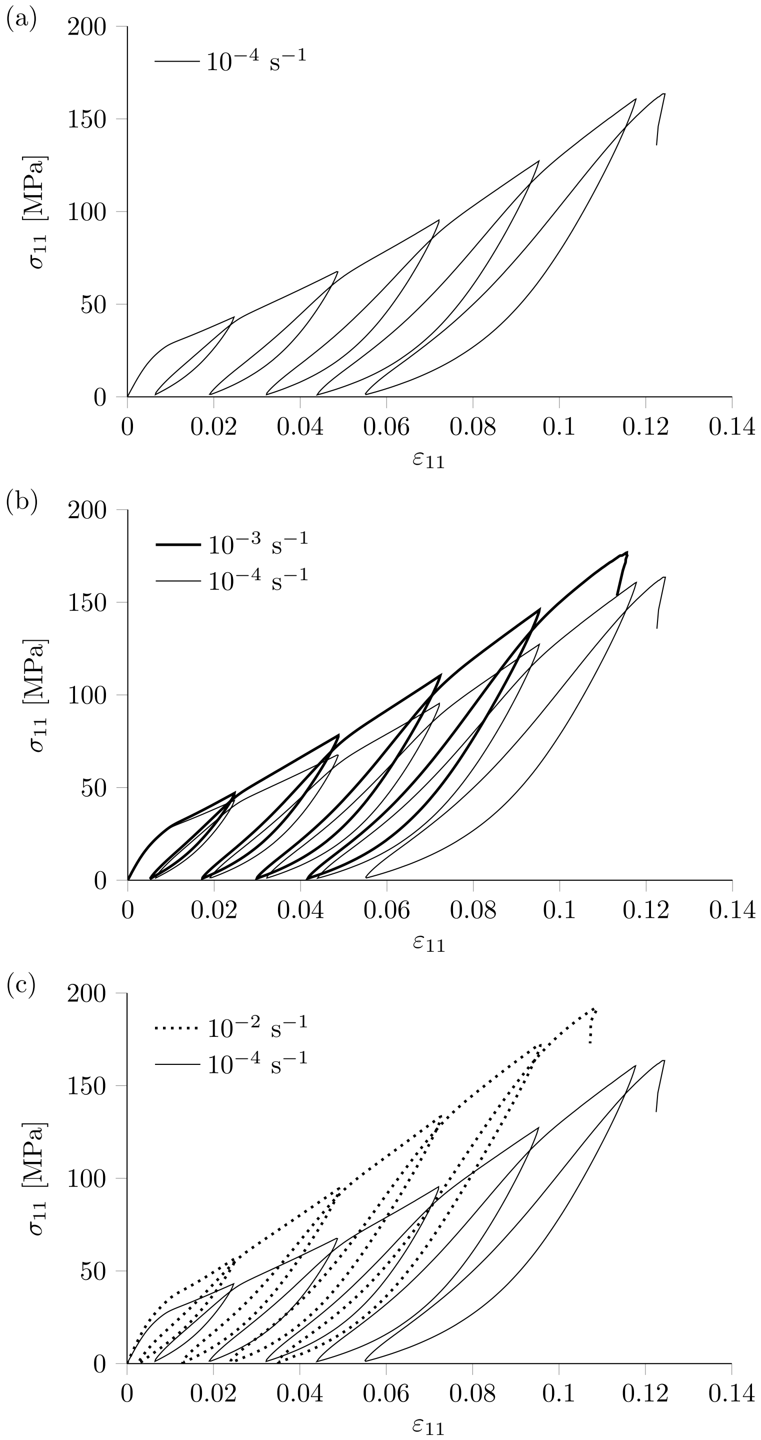

Figure 4.5: 1-direction stress-strain relation at (a) 10^{-4} s^{-1}, (b) 10^{-3} s^{-1} and (c) 10^{-2} s^{-1}.

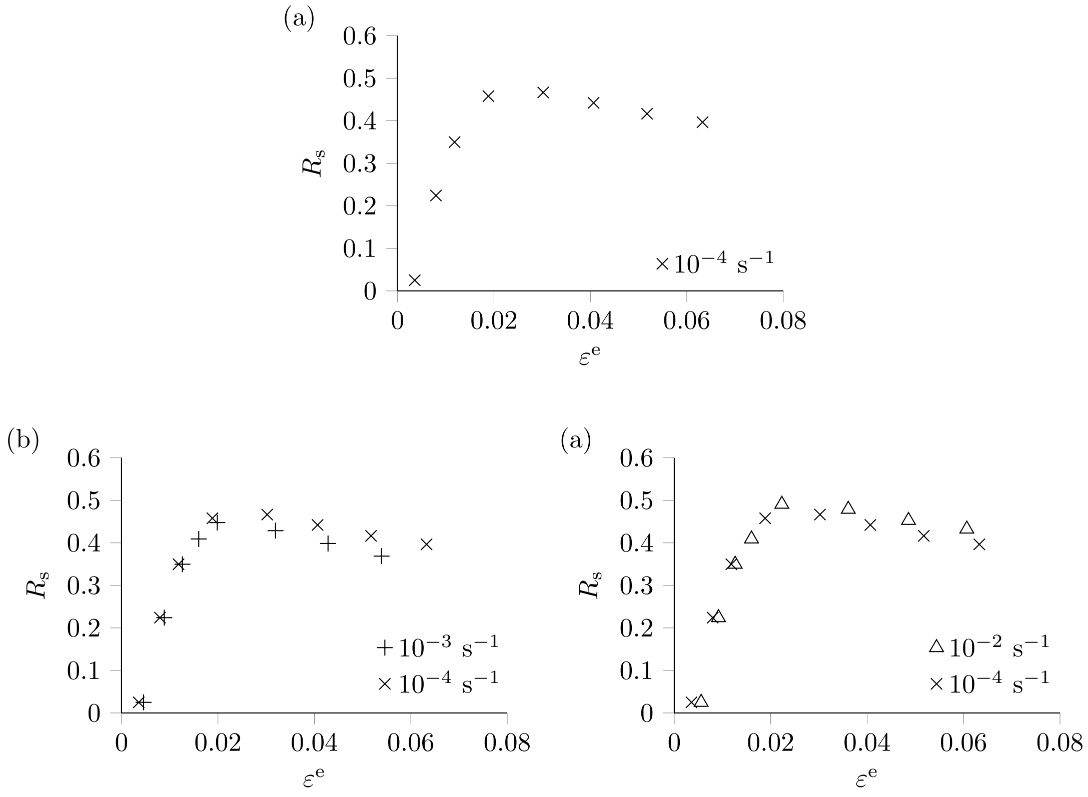

Figure 4.6: Evolution of stiffness variability ratio in tensile on 1-direction at (a) 10^{-4} s^{-1}, (b) 10^{-3} s^{-1} and (c) 10^{-2} s^{-1}.

4.3.2 Shear behaviour

Fig. 4.7 shows the shear curves obtained from the cyclic tensile tests on 45° oriented laminates at 10^{-4} s^{-1}, 10^{-3} s^{-1} and 10^{-2} s^{-1}. It must be remarked that these tests have not been performed until the breakage, since from certain deformation level the angle formed by the principal directions became significantly different of 45°, which is essential to decouple the shear mode. From them, the following observations have been made:

- Existence of irreversible strains.
- Generation of symmetric hysteresis loops resulting from the load-unload cycles.
- Strain rate dependence.

- Decrease (loss) of stiffness with the elastic strain at the global scale.

Fig. 4.7 also shows that the strain rate effect is perceptible not only in the hardening, but also in the cumulated irreversible strains and the size of hysteretic loops. The higher the strain rate, the lower the irreversible strains and the larger the hysteretic loops. This latter means that the higher the strain rate, the higher the dissipated energy by viscous phenomena. The undamaged elastic modulus G_{12}^0, obtained from the initial linear part of stress-strain curves within the range 2-6 MPa, is also affected by the strain rate (see Table 4.2). Concerning the stiffness, for every strain rate it decreases with the strain.

Fig. 4.8 shows the evolution of stiffness variability ratio R_s for the three strain rates. R_s decreases with strain as a consequence of damage generation.

Table 4.2: Undamaged shear elastic modulus depending on the strain rate.

	10^{-4} s^{-1}	10^{-3} s^{-1}	10^{-2} s^{-1}
G_{12}^0 [MPa]	1119.1±3.1	1120.4±5.1	1295.3±7.2

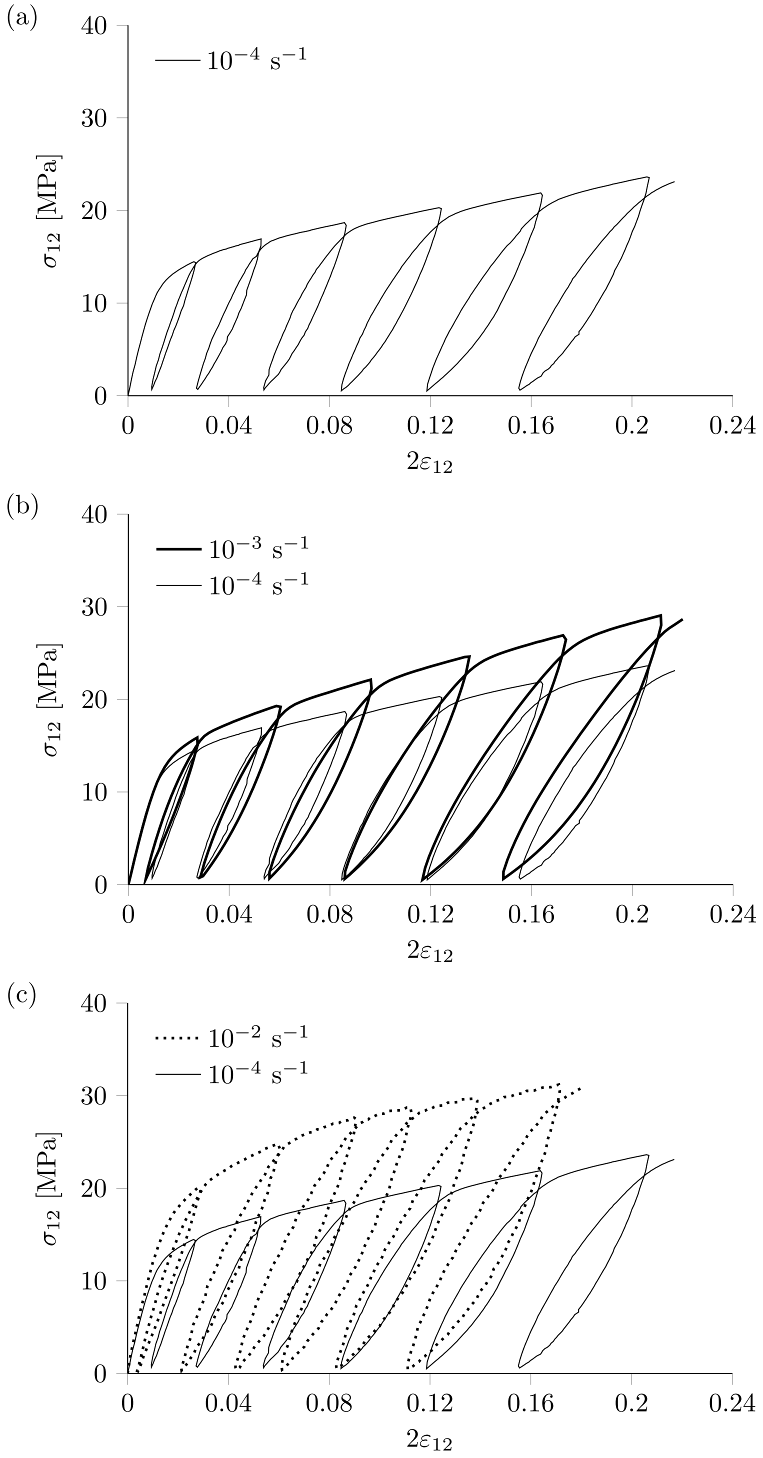

Figure 4.7: Shear stress-strain relation at (a) 10^{-4} s^{-1}, (b) 10^{-3} s^{-1} and (c) 10^{-2} s^{-1}.

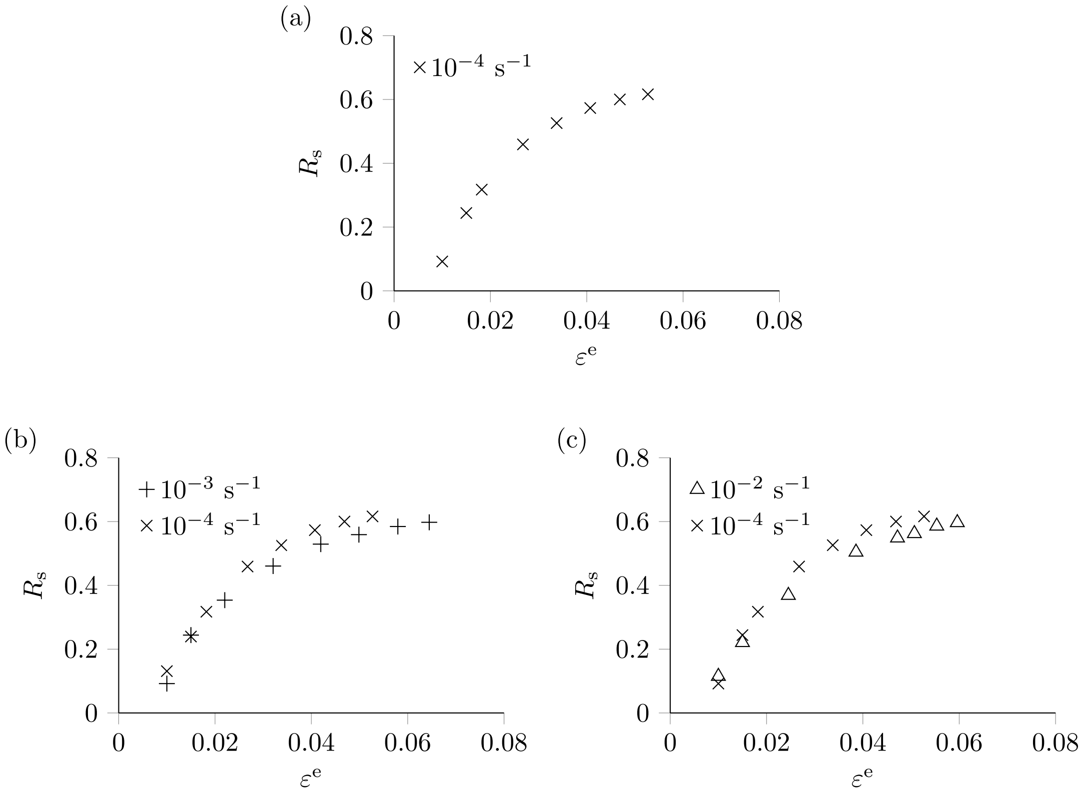

Figure 4.8: Evolution of stiffness variability ratio in shear at (a) 10^{-4} s^{-1}, (b) 10^{-3} s^{-1} and (c) 10^{-2} s^{-1}.

4.4 Mechanical response of Al/SRPP-FML

In this section, the mechanical response at different strain rates of Al/SRPP-FML is studied and the influence of SRPP as constituent material in the FML is evaluated. Fig. 4.9 shows the tensile stress-strain curve at different strain rates. As it can be seen, the FML presents a rate-dependent mechanical response. Assuming that the behaviour of aluminium does not depend significantly on strain rate [Seidt and Gilat, 2013], the appreciated rate-dependent response of the FML can be associated to the influence of the SRPP. Moreover, such influence is also reflected in the unload-reload cycles, in which hysteresis phenomena are detected (see Fig. 4.10).

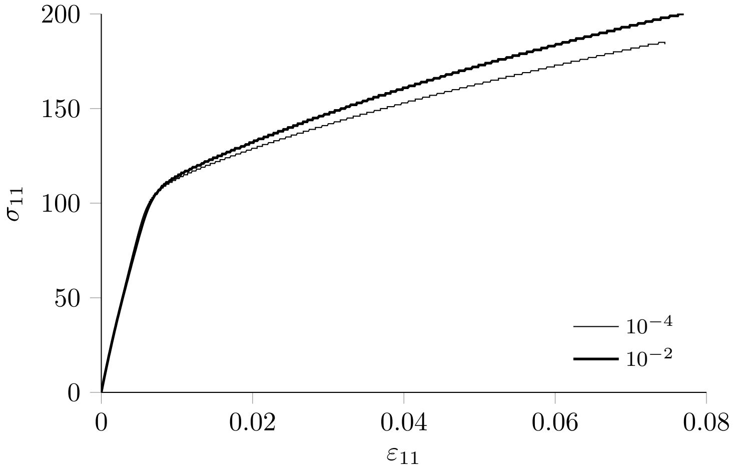

Figure 4.9: Tensile tests of Al/SRPP-FML at 10^{-4} s^{-1} and 10^{-2} s^{-1}.

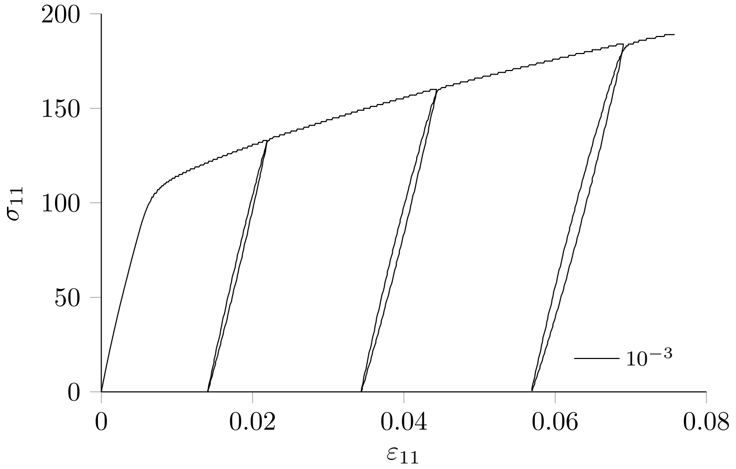

Figure 4.10: Cyclic tensile test of Al/SRPP-FML at 10^{-3} s^{-1}.

4.5 Conclusions

In the first part of this chapter, the SRPP has been characterised. The SRPP reveals that, both in tensile and shear, it presents irreversible strains when deformed, generates hysteresis loops when submitted to load-unload cycles, its stiffness varies with the elastic strain at global scale and its behaviour is rate-dependent.

In the second part of this chapter, the tensile mechanical response at different strain rates of Al/SRPP-FML is studied. It is demonstrated that the influence of the SRPP, as constituent material, in the FML is significant since makes the laminate behave according to a rate-dependent response. Moreover, the influence of the SRPP is also revealed based on the presences of hysteresis phenomena within the unload-reload cycles. This implies that the rate-dependent mechanical behaviour of the SRPP must be considered to model the mechanical response of the Al/SRPP-FML.

Chapter 5

Theoretical modelling of SRPP

This chapter addresses the mechanical behaviour modelling of the SRPP. A constitutive model of the quasi-static cyclic behaviour is formulated within the framework of thermodynamics of irreversible processes. This considers plasticity and histeresis phenomena, as well as stiffness variation caused by damage and stiffening. The model is validated for different strain-rates.

5.1 Continuum mechanics formulation

The models are written at the mesoscale of the layer which establishes a good compromise between the scales of the constitutive materials and the structure. A plane-stress state is assumed and only small strains are taken into account. The orthotropy frame defined in Chapter 4 is used.

The material model consists of two different models interacting each other. These are formulated separately. On the one hand, a elastoplastic model associated to the enveloping of the cyclic stress-strain curve is presented. On the other hand, to reproduce the stress-strain relation corresponding to hysteresis loops a non-standard viscoelastic model is formulated by using fractional operators. To deal with both the reversible and the irreversible effects, the classical split of the total strain $\boldsymbol{\varepsilon}$ is assumed to be

$$\boldsymbol{\varepsilon} = \boldsymbol{\varepsilon}^{\mathrm{e}} + \boldsymbol{\varepsilon}^{\mathrm{p}}, \tag{5.1}$$

where $\boldsymbol{\varepsilon}^{\mathrm{e}}$ stands for the elastic strain Voigt vector and $\boldsymbol{\varepsilon}^{\mathrm{p}}$ stands for the irreversible strain Voigt vector, and they are defined as

$$\begin{cases} \boldsymbol{\varepsilon}^{\mathrm{e}} = [\varepsilon^{\mathrm{e}}_{11}\ \varepsilon^{\mathrm{e}}_{22}\ \varepsilon^{\mathrm{e}}_{12}]^{\mathrm{T}} \\ \boldsymbol{\varepsilon}^{\mathrm{p}} = [\varepsilon^{\mathrm{p}}_{11}\ \varepsilon^{\mathrm{p}}_{22}\ \varepsilon^{\mathrm{p}}_{12}]^{\mathrm{T}} \end{cases}$$

In the following sections, the models associated to both the enveloping (Section 5.1.1) and the hysteresis loops (Section 5.1.2) are developed.

5.1.1 Model I. The envelope

The free energy potential and the elastic law

Assuming isothermal conditions and following the formalism of the thermodynamics of irreversible processes [De Souza Neto et al., 2008], the specific free energy, also so-called Helmholtz free energy per unit mass, is assumed to be a function

$$\psi(\boldsymbol{\varepsilon}, \boldsymbol{\varepsilon}^{\mathrm{p}}, \mathbf{d}, \mathbf{r}, \bar{\varepsilon}^{\mathrm{p}}) \tag{5.2}$$

of the total strain $\boldsymbol{\varepsilon}$, the plastic strain $\boldsymbol{\varepsilon}^{\mathrm{p}}$, the internal variables associated to damage $\mathbf{d}$ and stiffening $\mathbf{r}$, and the internal variables corresponding to hardening phenomenon $\bar{\varepsilon}^{\mathrm{p}}$. It is assumed that the free energy can be split as

$$\begin{aligned} \psi(\boldsymbol{\varepsilon}, \boldsymbol{\varepsilon}^{\mathrm{p}}, \mathbf{d}, \mathbf{r}, \bar{\varepsilon}^{\mathrm{p}}) &= \psi^{\mathrm{ed}}(\boldsymbol{\varepsilon} - \boldsymbol{\varepsilon}^{\mathrm{p}}, \mathbf{d}, \mathbf{r}) + \psi^{\mathrm{p}}(\bar{\varepsilon}^{\mathrm{p}}) = \\ &= \psi^{\mathrm{ed}}(\boldsymbol{\varepsilon}^{\mathrm{e}}, \mathbf{d}, \mathbf{r}) + \psi^{\mathrm{p}}(\bar{\varepsilon}^{\mathrm{p}}) \end{aligned} \tag{5.3}$$

into a sum of an elastic-damage contribution, ψ^{ed}, and a contribution due to hardening, ψ^{p}. Thus, the Helmholtz free energy expression is chosen to be

$$\rho\psi = \rho\psi(\boldsymbol{\varepsilon} - \boldsymbol{\varepsilon}^{\mathrm{p}}, \mathbf{d}, \mathbf{r}, \bar{\varepsilon}^{\mathrm{p}}) = \frac{1}{2}(\boldsymbol{\varepsilon} - \boldsymbol{\varepsilon}^{\mathrm{p}}) : \mathbf{C}(\mathbf{d}, \mathbf{r}) : (\boldsymbol{\varepsilon} - \boldsymbol{\varepsilon}^{\mathrm{p}}) + h(\bar{\varepsilon}^{\mathrm{p}}), \tag{5.4}$$

in which the damage variables vector $\mathbf{d}$ and the stiffness variables vector $\mathbf{r}$ affect the material stiffness tensor $\mathbf{C}$ [Desmorat, 2006], $\bar{\varepsilon}^{\mathrm{p}}$ is the accumulated plastic strain and $h(\bar{\varepsilon}^{\mathrm{p}})$ is the energy associated to hardening. Its differentiation yields

$$\dot{\psi} = \frac{\partial \psi}{\partial \varepsilon^{\mathrm{e}}} : \dot{\boldsymbol{\varepsilon}}^{\mathrm{e}} + \frac{\partial \psi}{\partial \mathbf{d}} \dot{\mathbf{d}} + \frac{\partial \psi}{\partial \mathbf{r}} \dot{\mathbf{r}} + \frac{\partial \psi}{\partial \bar{\varepsilon}^{\mathrm{p}}} \dot{\bar{\varepsilon}}^{\mathrm{p}}. \tag{5.5}$$

Substituting Eq. 5.5 into the Clausius-Duhem inequality results

$$\left(\boldsymbol{\sigma} - \rho \frac{\partial \psi}{\partial \boldsymbol{\varepsilon}^{\mathrm{e}}} \right) : \dot{\boldsymbol{\varepsilon}}^{\mathrm{e}} + \boldsymbol{\sigma} : \dot{\boldsymbol{\varepsilon}}^{\mathrm{p}} - \rho \frac{\partial \psi}{\partial \mathbf{d}} : \dot{\mathbf{d}} - \rho \frac{\partial \psi}{\partial \mathbf{r}} : \dot{\mathbf{r}} - \rho \frac{\partial \psi}{\partial \bar{\varepsilon}^{\mathrm{p}}} : \dot{\bar{\varepsilon}}^{\mathrm{p}} \geq 0. \tag{5.6}$$

From the last three terms, the thermodynamic force associated to the damage, stiffening and hardening thermodynamic forces are extracted and, respectively, defined as

$$\mathbf{Y} \equiv -\rho \frac{\partial \psi}{\partial \mathbf{d}}, \tag{5.7}$$

$$\mathbf{Z} \equiv -\rho \frac{\partial \psi}{\partial \mathbf{r}}, \tag{5.8}$$

$$\kappa \equiv -\rho \frac{\partial \psi}{\partial \bar{\varepsilon}^{\mathrm{p}}}, \tag{5.9}$$

so that the requirement of non-negative dissipation can be reduced to

$$\Upsilon(\boldsymbol{\sigma}, \mathbf{Y}, \mathbf{Z}, \kappa; \dot{\boldsymbol{\varepsilon}}^{\mathrm{p}}, \dot{\mathbf{d}}, \dot{\mathbf{r}}, \dot{\bar{\varepsilon}}^{\mathrm{p}}) \geq 0, \tag{5.10}$$

where the dissipation function Υ is defined by

$$\Upsilon(\boldsymbol{\sigma}, \mathbf{Y}, \mathbf{Z}, \kappa; \dot{\boldsymbol{\varepsilon}}^{\mathrm{p}}, \dot{\mathbf{d}}, \dot{\mathbf{r}}, \dot{\bar{\varepsilon}}^{\mathrm{p}}) \equiv \boldsymbol{\sigma} : \dot{\boldsymbol{\varepsilon}}^{\mathrm{p}} - \mathbf{Y}\dot{\mathbf{d}} - \mathbf{Z}\dot{\mathbf{r}} - \kappa \dot{\bar{\varepsilon}}^{\mathrm{p}}. \tag{5.11}$$

Considering the elastic contribution represented by the first term of Eq. 5.4, the general corresponding elastic law is given by

$$\boldsymbol{\sigma} \equiv \rho \frac{\partial \psi}{\partial \boldsymbol{\varepsilon}^{\mathrm{e}}} = \mathbf{C}(\mathbf{d}, \mathbf{r}) : \boldsymbol{\varepsilon}^{\mathrm{e}}, \tag{5.12}$$

where $\boldsymbol{\varepsilon}^{\mathrm{e}}$ will be obtained based on a elastic predictor/return mapping scheme [De Souza Neto et al., 2008].

Yield function, plastic flow rule and hardening law

According to the plasticity phenomena identified in both the principal and shear directions, an anisotropic yield criterion is proposed subsequently. This yield criterion considers the presence of damage by introducing the effective stress, which is defined as

$$\tilde{\boldsymbol{\sigma}} = \left\{ \begin{array}{c} \dfrac{\sigma_{11}}{(1-d_{11})} \\ \dfrac{\sigma_{22}}{(1-d_{22})} \\ \dfrac{\sigma_{12}}{(1-d_{12})} \end{array} \right\}, \tag{5.13}$$

within the expression of the yield surface, which is formulated as

$$\Phi(\tilde{\boldsymbol{\sigma}}, \sigma_{\mathrm{y}}) = q(\tilde{\boldsymbol{\sigma}}) - \sigma_{\mathrm{y}}, \tag{5.14}$$

where $q(\tilde{\boldsymbol{\sigma}})$ is the equivalent stress and σ_{y} is the hardening function. Generalising the expression used by Ladevèze and LeDantec [1992], the following definition of the equivalent stress is proposed:

$$q(\tilde{\boldsymbol{\sigma}}) = \sqrt{(\tilde{\sigma}_{12}^2 + a_1^2\tilde{\sigma}_{11}^2 + a_2^2\tilde{\sigma}_{22}^2)}, \tag{5.15}$$

where a_1 and a_2 are material parameters. Besides, the hardening function is assumed to be

$$\sigma_{\mathrm{y}} = \sigma_{\mathrm{y}0} + \kappa(\bar{\varepsilon}^{\mathrm{p}}), \tag{5.16}$$

where $\sigma_{\mathrm{y}0}$ is the initial shear yield stress.

In the determination of the equivalent stress the parameters a_1 and a_2 assign a weight to the loads in principal directions. These are defined as the relation between the shear yield evolution (hardening function) and the tensile yield evolution corresponding to direction 1 and direction 2, respectively. Thus, a_1 and a_2 depend on the accumulated plastic strain $\bar{\varepsilon}^{\mathrm{p}}$, which is defined as

$$\bar{\varepsilon}^{\mathrm{p}} = \int_0^t \sqrt{\left(4\left(\dot{\varepsilon}_{12}^{\mathrm{p}}\right)^2 + \frac{1}{a_1^2}\left(\dot{\varepsilon}_{11}^{\mathrm{p}}\right)^2 + \frac{1}{a_2^2}\left(\dot{\varepsilon}_{22}^{\mathrm{p}}\right)^2\right)}\,\mathrm{d}t. \tag{5.17}$$

As the material herein studied is a balanced woven fabric composite, the mechanical properties in the principal directions are the same and, hence, $a_1(\bar{\varepsilon}^{\mathrm{p}})$ and $a_2(\bar{\varepsilon}^{\mathrm{p}})$ are equal. To determine the evolution of these parameters it must be proceed as follows (taking as an example the case of $a_1(\bar{\varepsilon}^{\mathrm{p}})$):

- Firstly, a_1 is calculated for $\bar{\varepsilon}^{\mathrm{p}} = 0$.
- Then, it is assumed an increment of the accumulated plastic strain $\Delta\bar{\varepsilon}^{\mathrm{p}}$ based on the value of a_1 calculated in the previous step.
- a_1 is calculated for the new stage.
- These steps are repeated iteratively.

Finally, the accumulated plastic strain is calculated solving the Eq. 5.17.

Concerning the plastic flow rule, assuming a an associative plasticity model, which implies that the yield function, Φ, is taken as the flow potential [De Souza Neto et al., 2008; Simo and Hughes, 1998], i.e.

$$\Psi = \Phi, \tag{5.18}$$

the corresponding flow vector is given by

$$\mathbf{N} \equiv \frac{\partial \Phi}{\partial \boldsymbol{\sigma}} = \frac{\partial}{\partial \boldsymbol{\sigma}} \left[\sqrt{(\tilde{\sigma}_{12}^2 + a_1^2\tilde{\sigma}_{11}^2 + a_2^2\tilde{\sigma}_{22}^2)} \right] = \frac{1}{q(\tilde{\boldsymbol{\sigma}})} \left\{ \begin{array}{c} a_1^2\tilde{\sigma}_{11} \\ a_2^2\tilde{\sigma}_{22} \\ \tilde{\sigma}_{12} \end{array} \right\} \tag{5.19}$$

and the flow rule results in

$$\dot{\boldsymbol{\varepsilon}}^{\mathrm{p}} = \dot{\gamma}\frac{1}{q(\tilde{\boldsymbol{\sigma}})} \left\{ \begin{array}{c} a_1^2\tilde{\sigma}_{11} \\ a_2^2\tilde{\sigma}_{22} \\ \tilde{\sigma}_{12} \end{array} \right\} \tag{5.20}$$

where $\dot{\gamma}$ is the plastic multiplier rate.

5.1.2 Model II. The hysteresis loops

As it has been introduced, in order to reproduce the stress-strain relation corresponding to hysteresis loops, a non-standard viscoelastic damage model is written by using fractional operators. The damage during unloading is assumed to remain constant until further positive loading is applied and causes further damage accumulation. Following the same reasoning, the stiffening is also assumed to remain constant during such phase. In an effort to make easier the reading, the terms associated to the damage and stiffening has been omitted in the formulation developed in this section; however, they are reintroduced at the end of the mathematical development and, of course, considered in the model.

The model used is a fractional standard linear solid (F-SLS), also known as the fractional Zener model (see Fig. 5.1). Differently of the non-fractional Zener model, the fractional one presents a generalised viscous element (called spring-pot and represented by a diamond-shape element), which replaces the dashpot [Koeller, 1984]. The F-SLS model is a particular case of the fractional generalised Maxwell model, which in turn generalises the (non-fractional) generalised Maxwell model (see Appendix A.1) [Koeller, 1984].

The free energy potential and the fractional viscoelastic damage law

The F-SLS model consists of a Hookean elastic spring and a fractional Maxwell branch (see Appendix A.1) connected in parallel (see Fig. 5.1).

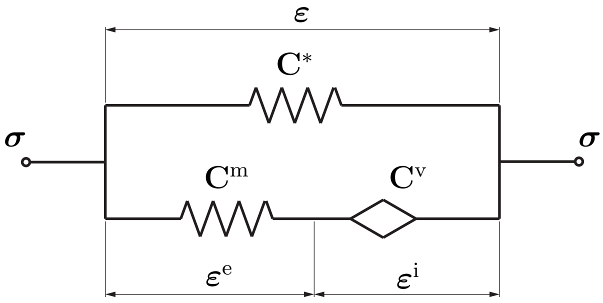

Figure 5.1: Fractional solid linear standard model.

Assuming isothermal conditions, the state variables are the strain $\boldsymbol{\varepsilon}$ and the inelastic strain $\boldsymbol{\varepsilon}^{\mathrm{i}}$. The Helmholtz free energy $\rho\psi$ is given by

$$\rho\psi(\boldsymbol{\varepsilon},\boldsymbol{\varepsilon}^{\mathrm{i}}) = \frac{1}{2}\boldsymbol{\varepsilon} : \mathbf{C}^{*} : \boldsymbol{\varepsilon} + \frac{1}{2}(\boldsymbol{\varepsilon}-\boldsymbol{\varepsilon}^{\mathrm{i}}) : \mathbf{C}^{\mathrm{m}} : (\boldsymbol{\varepsilon}-\boldsymbol{\varepsilon}^{\mathrm{i}}), \tag{5.21}$$

where $\mathbf{C}^{*}$ is a fourth order elasticity tensor. Its differentiation then yields

$$\dot{\psi} = \frac{\partial\psi}{\partial\boldsymbol{\varepsilon}} : \dot{\boldsymbol{\varepsilon}} + \frac{\partial\psi}{\partial\boldsymbol{\varepsilon}^{\mathrm{i}}} : \dot{\boldsymbol{\varepsilon}}^{\mathrm{i}}. \tag{5.22}$$

Substituting Eq. 5.22 into the Clausius-Duhem inequality yields

$$\left(\boldsymbol{\sigma} - \rho\frac{\partial\psi}{\partial\boldsymbol{\varepsilon}}\right) : \dot{\boldsymbol{\varepsilon}} - \rho\frac{\partial\psi}{\partial\boldsymbol{\varepsilon}^{\mathrm{i}}} : \dot{\boldsymbol{\varepsilon}}^{\mathrm{i}} \geq 0. \tag{5.23}$$

Making use of Eq. 5.21 the following state law is obtained:

$$\boldsymbol{\sigma} = \rho\frac{\partial\psi}{\partial\boldsymbol{\varepsilon}} = \mathbf{C}^{*} : \boldsymbol{\varepsilon} + \mathbf{C}^{\mathrm{m}} : (\boldsymbol{\varepsilon}-\boldsymbol{\varepsilon}^{\mathrm{i}}) = \mathbf{C}^{*} : \boldsymbol{\varepsilon} + \boldsymbol{\sigma}^{\mathrm{m}}, \tag{5.24}$$

where $\boldsymbol{\sigma}^{\mathrm{m}}$ is the stress corresponding to the Maxwell branch. Then, the dissipation yields

$$\Upsilon(\boldsymbol{\sigma};\dot{\boldsymbol{\varepsilon}}^{\mathrm{i}}) = \mathbf{C}^{\mathrm{V}} : \mathrm{D}_t^{\alpha}\boldsymbol{\varepsilon}^{\mathrm{i}} : \dot{\boldsymbol{\varepsilon}}^{\mathrm{i}}, \tag{5.25}$$

where $\mathbf{C}^{\mathrm{v}}$ is the fourth order viscosity tensor and α, being $0 \leq \alpha \leq 1$, is the order of the fractional derivative.

In order to satisfy the Clausius-Duhem inequality, the dissipation must be greater or equal to zero. To verify so, following the observation by Lion [1997] that a spring-pot can be interpreted in terms of a continuous superposition of Maxwell elements in parallel, which was obtained from the power-law spectrum derived by Tschoegl [1989], the spring-pot in the fractional model can be replaced by N discrete Maxwell elements in parallel (see Fig. 5.2).

Denoting $z_k > 0$ the relaxation time for the element k, the discrete stiffness and viscosity tensors are denoted by $\mathbf{C}_k^{\mathrm{v}}$ and $z_k\mathbf{C}_k^{\mathrm{v}}$, respectively, and the internal

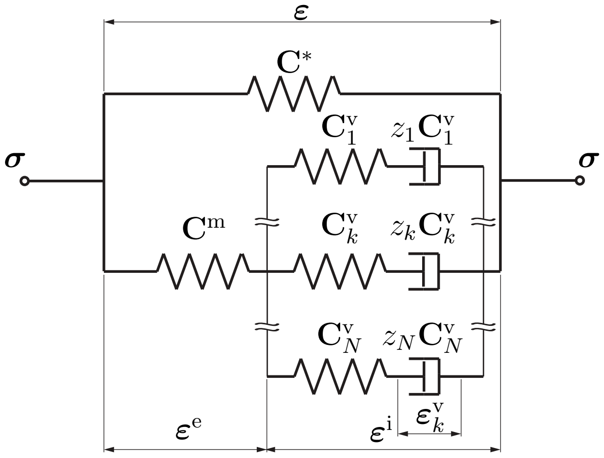

Figure 5.2: Fractional solid linear standard model based on N discret Maxwell model.

strains of the dashpots as $\boldsymbol{\varepsilon}_k^{\mathrm{v}}$. The Helmholtz free energy $\rho\psi$ is given by

$$\begin{aligned}\rho\psi(\boldsymbol{\varepsilon},\boldsymbol{\varepsilon}^{\mathrm{i}},\boldsymbol{\varepsilon}_k^{\mathrm{v}}) = \frac{1}{2}\boldsymbol{\varepsilon} : \mathbf{C} : \boldsymbol{\varepsilon} + \frac{1}{2}(\boldsymbol{\varepsilon}-\boldsymbol{\varepsilon}^{\mathrm{i}}) : \mathbf{C}^{\mathrm{m}} : (\boldsymbol{\varepsilon}-\boldsymbol{\varepsilon}^{\mathrm{i}}) + \\ + \frac{1}{2}\sum_{k=1}^{N}(\boldsymbol{\varepsilon}^{\mathrm{i}}-\boldsymbol{\varepsilon}_k^{\mathrm{v}}) : \mathbf{C}_k^{\mathrm{v}} : (\boldsymbol{\varepsilon}^{\mathrm{i}}-\boldsymbol{\varepsilon}_k^{\mathrm{v}}).\end{aligned} \tag{5.26}$$

Its differentiation then yields

$$\begin{aligned}\dot{\psi} = \big(\mathbf{C}^* : \boldsymbol{\varepsilon} + \mathbf{C}^{\mathrm{m}} : (\boldsymbol{\varepsilon}-\boldsymbol{\varepsilon}^{\mathrm{i}})\big) : \dot{\boldsymbol{\varepsilon}} + \\ + \left(\sum_{k=1}^{N}\mathbf{C}_k^{\mathrm{v}} : (\boldsymbol{\varepsilon}^{\mathrm{i}}-\boldsymbol{\varepsilon}_k^{\mathrm{v}}) - \mathbf{C}^{\mathrm{m}} : (\boldsymbol{\varepsilon}-\boldsymbol{\varepsilon}^{\mathrm{i}})\right) : \dot{\boldsymbol{\varepsilon}}^{\mathrm{i}} - \\ - \sum_{k=1}^{N}\mathbf{C}_k^{\mathrm{v}} : (\boldsymbol{\varepsilon}^{\mathrm{i}}-\boldsymbol{\varepsilon}_k^{\mathrm{v}}) : \dot{\boldsymbol{\varepsilon}}_k^{\mathrm{v}}.\end{aligned} \tag{5.27}$$

Substituting Eq. 5.27 into the Clausius-Duhem inequality yields

$$\begin{aligned}\big(\boldsymbol{\sigma} - \mathbf{C}^* : \boldsymbol{\varepsilon} + \mathbf{C}^{\mathrm{m}} : (\boldsymbol{\varepsilon}-\boldsymbol{\varepsilon}^{\mathrm{i}})\big) : \dot{\boldsymbol{\varepsilon}} + \left(\mathbf{C}^{\mathrm{m}} : (\boldsymbol{\varepsilon}-\boldsymbol{\varepsilon}^{\mathrm{i}}) - \sum_{k=1}^{N}\mathbf{C}_k^{\mathrm{v}} : (\boldsymbol{\varepsilon}^{\mathrm{i}}-\boldsymbol{\varepsilon}_k^{\mathrm{v}})\right) : \dot{\boldsymbol{\varepsilon}}^{\mathrm{i}} + \\ + \sum_{k=1}^{N}\mathbf{C}_k^{\mathrm{v}} : (\boldsymbol{\varepsilon}^{\mathrm{i}}-\boldsymbol{\varepsilon}_k^{\mathrm{v}}) : \dot{\boldsymbol{\varepsilon}}_k^{\mathrm{v}} \geq 0.\end{aligned} \tag{5.28}$$

In the previous expression, the coefficient of $\dot{\boldsymbol{\varepsilon}}$ must vanish, giving the state law for the discrete system

$$\boldsymbol{\sigma} = \mathbf{C}^{*} : \boldsymbol{\varepsilon} + \mathbf{C}^{\mathrm{m}} : (\boldsymbol{\varepsilon} - \boldsymbol{\varepsilon}^{\mathrm{i}}). \tag{5.29}$$

According to the equilibrium conditions, it occurs the same with the coefficient of $\dot{\boldsymbol{\varepsilon}}^{\mathrm{i}}$, resulting

$$\mathbf{C}^{\mathrm{m}} : (\boldsymbol{\varepsilon} - \boldsymbol{\varepsilon}^{\mathrm{i}}) = \sum_{k=1}^{N} \mathbf{C}_k^{\mathrm{v}} : (\boldsymbol{\varepsilon}^{\mathrm{i}} - \boldsymbol{\varepsilon}_k^{\mathrm{v}}). \tag{5.30}$$

Considering a single Maxwell element the stresses in the spring and the dashpot are equal, the following relation is obtained:

$$z_k \dot{\boldsymbol{\varepsilon}}_k^{\mathrm{v}} = \boldsymbol{\varepsilon}^{\mathrm{i}} - \boldsymbol{\varepsilon}_k^{\mathrm{v}}. \tag{5.31}$$

Introducing Eq. 5.30 and Eq. 5.31 into Eq. 5.28, the dissipation yields

$$\Upsilon(\boldsymbol{\sigma}^{\mathrm{m}}; \dot{\boldsymbol{\varepsilon}}^{\mathrm{i}}) = \sum_{k=1}^{N} (\boldsymbol{\varepsilon} - \boldsymbol{\varepsilon}_k^{\mathrm{v}}) : \frac{\mathbf{C}_k^{\mathrm{v}}}{z_k} : (\boldsymbol{\varepsilon} - \boldsymbol{\varepsilon}_k^{\mathrm{v}}), \tag{5.32}$$

which satisfies the condition of non-negativity of the dissipation. Thus, after discretising the spring-pot by Maxwell elements in parallel, it has been shown that the discrete fractional Maxwell model satisfies the Clausius-Duhem inequality. Once demonstrated the admissibility of the model, introducing the damage and stiffening variables, omitted in the mathematical development, makes the dissipation to be

$$\Upsilon(\boldsymbol{\sigma}^{\mathrm{m}}, \mathbf{Y}, \mathbf{Z}; \dot{\boldsymbol{\varepsilon}}^{\mathrm{i}}, \dot{\mathbf{d}}, \dot{\mathbf{r}}) = \mathbf{C}^{\mathrm{V}} : \mathrm{D}_t^{\alpha} \boldsymbol{\varepsilon}^{\mathrm{i}} : \dot{\boldsymbol{\varepsilon}}^{\mathrm{i}} + \mathbf{Y}\dot{\mathbf{d}} + \mathbf{Z}\dot{\mathbf{r}}, \tag{5.33}$$

resulting the state law

$$\boldsymbol{\sigma} = \rho \frac{\partial \psi}{\partial \boldsymbol{\varepsilon}} = \mathbf{C}^{*}(\mathbf{d}, \mathbf{r}) : \boldsymbol{\varepsilon} + \mathbf{C}^{\mathrm{m}} : (\boldsymbol{\varepsilon} - \boldsymbol{\varepsilon}^{\mathrm{i}}). \tag{5.34}$$

Considering that

$$\mathbf{C}^{\mathrm{m}} : (\boldsymbol{\varepsilon} - \boldsymbol{\varepsilon}^{\mathrm{i}}) = \mathbf{C}^{\mathrm{v}} : \mathrm{D}_t^{\alpha} \boldsymbol{\varepsilon}^{\mathrm{i}}, \tag{5.35}$$

according to F-SLS model (see Fig. 5.1) and after working appropriately with Eq. 5.34 and reorganising the terms, the state law can be represented as a function exclusively of the total strain $\boldsymbol{\varepsilon}$, yielding

$$\begin{aligned} &\boldsymbol{\sigma} + \left(\mathbf{C}^{\mathrm{m}}\right)^{-1} : \mathbf{C}^{\mathrm{v}} : \mathrm{D}_t^{\alpha}\boldsymbol{\sigma} = \\ &= \mathbf{C}^{*}(\mathbf{d},\mathbf{r}) : \boldsymbol{\varepsilon} + \left(\mathbf{C}^{\mathrm{m}}\right)^{-1} : \left(\mathbf{C}^{*}(\mathbf{d},\mathbf{r}) + \mathbf{C}^{\mathrm{m}}\right) : \mathbf{C}^{\mathrm{v}} : \mathrm{D}_t^{\alpha}\boldsymbol{\varepsilon}. \end{aligned} \tag{5.36}$$

5.2 Cyclic shear behaviour law

5.2.1 Elastoplastic modelling of the envelope

The free energy potential and the elastoplastic damage law

Considering pure shear conditions, the Helmholtz's free energy for the enveloping of the cyclic stress-strain curve results

$$\rho\psi = \rho\psi(\varepsilon_{12} - \varepsilon_{12}^{\mathrm{p}}, d_{12}, \bar{\varepsilon}^{\mathrm{p}}) = \frac{1}{2}2G_{12}^{0}(1 - d_{12})(\varepsilon_{12} - \varepsilon_{12}^{\mathrm{p}})^{2} + h(\bar{\varepsilon}^{\mathrm{p}}), \tag{5.37}$$

where G_{12}^{0}, d_{12} and $\bar{\varepsilon}^{\mathrm{p}}$ stand for the undamaged elastic modulus, the damage variable associated to loss of stiffness and the accumulated plastic strain, respectively. Using the split of strain

$$\varepsilon_{12}^{\mathrm{e}} = \varepsilon_{12} - \varepsilon_{12}^{\mathrm{p}}, \tag{5.38}$$

Eq. 5.37 yields

$$\rho\psi = \frac{1}{2}2G_{12}^{0}(1 - d_{12})(\varepsilon_{12}^{\mathrm{e}})^{2} + h(\bar{\varepsilon}^{\mathrm{p}}). \tag{5.39}$$

After differentiating this expression and substituting into the Clausius-Duhem inequality, the model for the shear Cauchy's stress σ_{12}, the thermodynamic force Y_{12}, associated to the shear damage variable; and the thermodynamic force κ, associated to the accumulated plastic strain $\bar{\varepsilon}^{\mathrm{p}}$, are obtained:

$$\sigma_{12} = \rho\frac{\partial\psi}{\partial\varepsilon_{12}} = 2G_{12}^{0}(1 - d_{12})(\varepsilon_{12}^{\mathrm{e}}) \tag{5.40}$$

$$Y_{12} = -\rho \frac{\partial \psi}{\partial d_{12}} = \frac{1}{2} 2G^0_{12} (\varepsilon^{\mathrm{e}}_{12})^2 \tag{5.41}$$

$$\kappa = \rho \frac{\partial \psi}{\partial \bar{\varepsilon}^{\mathrm{p}}} = \rho \frac{\partial h(\bar{\varepsilon}^{\mathrm{p}})}{\partial \bar{\varepsilon}^{\mathrm{p}}} = \kappa(\bar{\varepsilon}^{\mathrm{p}}), \tag{5.42}$$

The dissipation, for its part, is given by

$$\Upsilon^{\mathrm{in}}_{12} = Y_{12} \dot{d}_{12} + \kappa \dot{\bar{\varepsilon}}^{\mathrm{p}}, \tag{5.43}$$

which must be positive in order to fulfil the Clausius-Duhem inequality.

Experimental evolution laws

In this section, the hardening, shear damage and shear stiffening evolution laws are determined. To do so, the irreversible strain $\varepsilon^{\mathrm{p}}_{12}$ and the stiffness variability ratio $R_{\mathrm{s}.12}$ for every cycle of the shear stress-strain curve must be obtained. $\varepsilon^{\mathrm{p}}_{12}$ is necessary to identify the hardening function and $R_{\mathrm{s}.12}$ is required to determine the damage and stiffening evolution laws. This latter is obtained from the average slope within the loop G_{12} and the initial undamaged slope G^0_{12}.

According to Fig. 4.8, $R_{\mathrm{s}.12}$ increases continuously until saturating, differently of the tensile stiffness variability ratio $R_{\mathrm{s}.11}$ as in Chapter 4 was shown. Thus, an absence of stiffening phenomenon is considered. This implies that $R_{\mathrm{s}.12}$ is equal to the shear damage, so that according to Eq. 4.19 and Eq. 4.20,

$$R_{\mathrm{s}.12} = 1 - \frac{G_{12}}{G^0_{12}} = d_{12}. \tag{5.44}$$

Assuming that damage during unloading remains constant until further positive loading is applied and causes further damage accumulation, the parameter $\bar{Y}_{12}$ is defined to describe the shear damage development. It is based on the maximum value reached by the thermodynamic force associated to damage Y_{12} along the previous loading history;

$$\bar{Y}_{12} = \max_{\tau \le t} \left(\sqrt{Y_{12}(\tau)} \right). \tag{5.45}$$

Then, the shear damage evolution law is defined as

$$d_{12} = f_{12}(\bar{Y}_{12}), \tag{5.46}$$

where f_{12} is the damage evolution function. From experimental data, an exponential evolution has seemed to be a proper form for the shear damage evolution curve;

$$d_{12} = f_{12}(\bar{Y}_{12}) = d_{12}^{\mathrm{s}} \left\langle 1 - \mathrm{e}^{-\beta_{12}\left(\bar{Y}_{12} - \sqrt{Y_{12}^{0}}\right)} \right\rangle_{+} \quad \text{if} \quad d_{12} < 1 \quad \text{and} \quad \bar{Y}_{12} < \sqrt{Y_{12}^{\mathrm{c}}}, \tag{5.47}$$

where $\langle\rangle_+$ is the Macaulay bracket, Y_{12}^{c} is the damage critical thermodynamic force; Y_{12}^{0}, the damage initiation thermodynamic force; d_{12}^{s}, the damage saturation; and β_{12}, a coefficient related to damage saturation rate.

Concerning the hardening law, a potential evolution has seemed to be a proper form to reproduce the hardening curve:

$$\sigma_{\mathrm{y}} = \sigma_{\mathrm{y0}} + \kappa(\bar{\varepsilon}^{\mathrm{p}}) = \sigma_{\mathrm{y0}} + K(\bar{\varepsilon}^{\mathrm{p}})^{m} \tag{5.48}$$

where K and m are material parameters.

Table 5.1 collects the material parameters of the shear evolution laws for the three strain rates and Fig. 5.3 shows the (a) hardening and (b) shear damage experimental data at 10^{-4} s^{-1}, 10^{-3} s^{-1} and 10^{-2} s^{-1}, and their respective approximations.

At this point, the shear elastoplastic model is completely defined. Fig. 5.4 shows the response of the model for the three strain rates. The model reproduces accurately the envelopes of the shear stress-strain curves; however, it considers that the unloading is linear. In the following section, this imprecision of the model is resolved using the fractional viscoelastic model to reproduce the hysteresis loops.

Table 5.1: Hardening and shear damage parameters at 10^{-4} s^{-1}, 10^{-3} s^{-1} and 10^{-2} s^{-1}.

$\dot{\varepsilon}_{12}$ [s^{-1}]	Hardening parameters			Damage parameters		
	K	m	σ_{y0}	d_{12}^{s}	β_{12}	Y_{12}^{0}
10^{-4}	29.42	0.4931	11.82	0.655	2.60	0.185
10^{-3}	48.73	0.6033	13.72	0.633	2.06	0.124
10^{-2}	33.79	0.3678	16.42	0.660	1.70	0.150

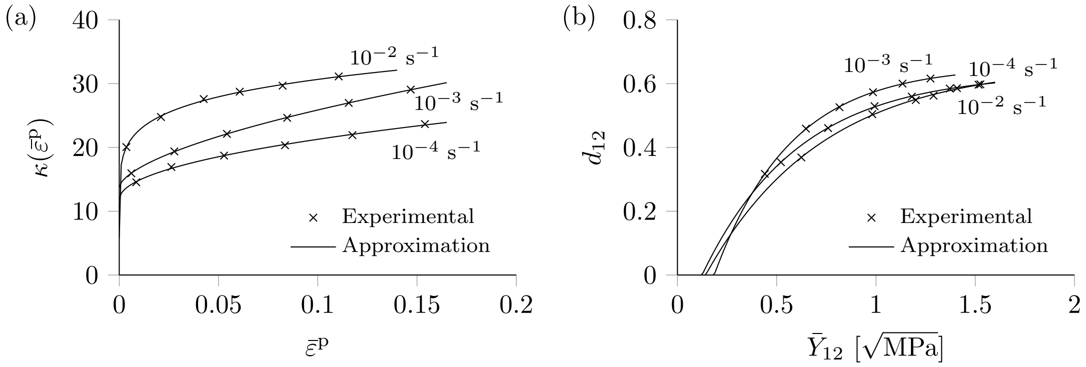

Figure 5.3: (a) Hardening and (b) shear damage laws at 10^{-4} s^{-1}, 10^{-3} s^{-1} and 10^{-2} s^{-1}.

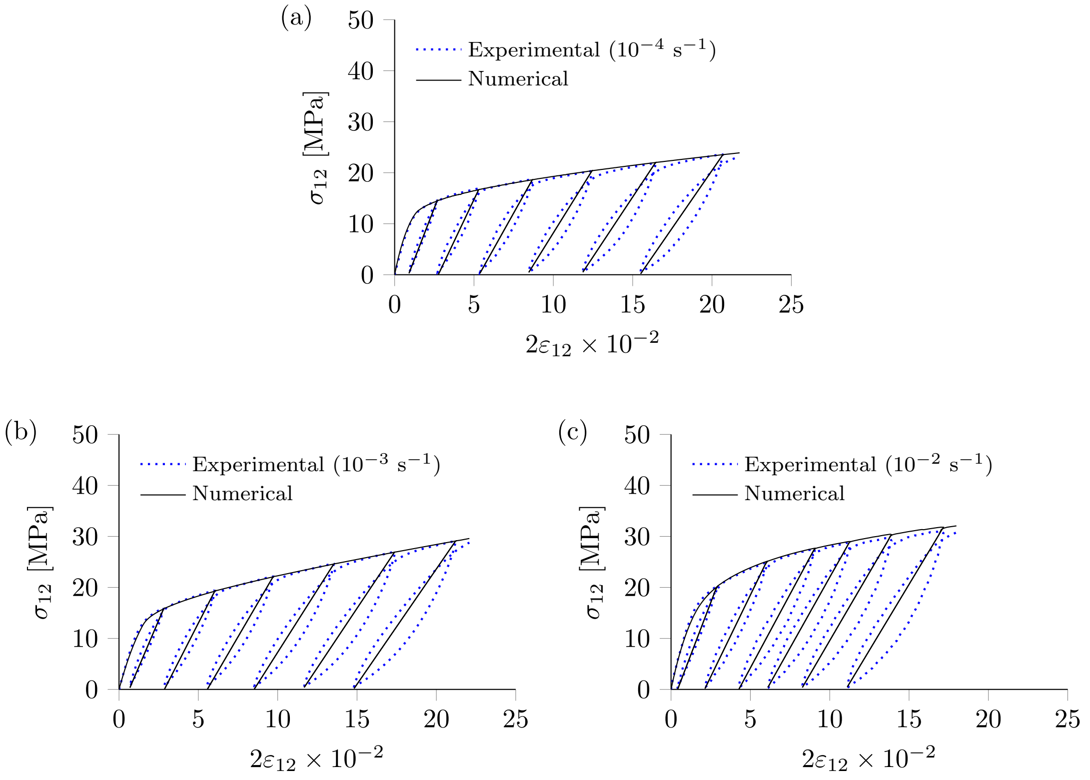

Figure 5.4: Numerical-experimental correlation in shear at (a) 10^{-4} s^{-1}, (b) 10^{-3} s^{-1} and (c) 10^{-2} s^{-1} considering the elastoplastic model.

5.2.2 Fractional viscoelastic modelling of the hysteresis loops

The free energy potential and the fractional viscoelastic law

Given the pure shear conditions, the rheological model can be represented as Fig. 5.5 shows.

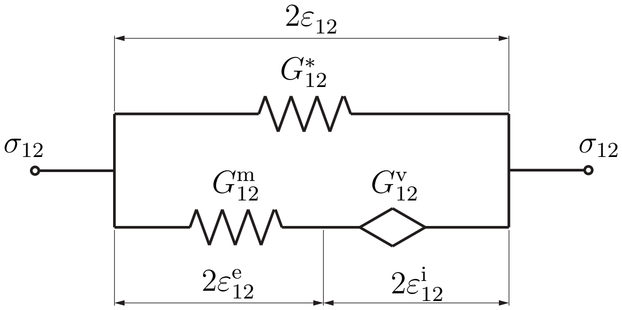

Figure 5.5: Rheological representation of the shear F-SLS model.

The Helmholtz's free energy for the hysteresis loops results

$$\rho\psi(\varepsilon_{12},\varepsilon^{\mathrm{i}}_{12}) = \frac{1}{2}G^{*}_{12}\varepsilon^{2}_{12} + \frac{1}{2}G^{\mathrm{m}}_{12}(\varepsilon_{12}-\varepsilon^{\mathrm{i}}_{12})^{2}, \tag{5.49}$$

where G^{*}_{12} and G^{m}_{12} are material parameters. After differentiating this expression and substituting into the Clausius-Duhem inequality, the following non-standard model for the Cauchy's shear stress σ_{12} is proposed;

$$\sigma_{12} = \rho\frac{\partial\psi}{\partial\varepsilon_{12}} = G^{*}_{12}\varepsilon_{12} + G^{\mathrm{m}}_{12}(\varepsilon_{12}-\varepsilon^{\mathrm{i}}_{12}). \tag{5.50}$$

Then, considering that

$$G^{\mathrm{m}}_{12}(\varepsilon_{12}-\varepsilon^{\mathrm{i}}_{12}) = G^{\mathrm{v}}_{12}\mathrm{D}^{\alpha_{12}}_{t}\varepsilon^{\mathrm{i}}_{12}, \tag{5.51}$$

after working appropriately with Eq. 5.76 and reorganising the terms, the state law can be represented as a function exclusively of the total strain ε_{12}, yielding

$$\sigma_{12}+\frac{G^{\mathrm{v}}_{12}}{G^{\mathrm{m}}_{12}}\mathrm{D}^{\alpha_{12}}_{t}\sigma_{12} = G^{*}_{12}\varepsilon_{12} + \frac{G^{*}_{12}+G^{\mathrm{m}}_{12}}{G^{\mathrm{m}}_{12}}G^{\mathrm{v}}_{12}\mathrm{D}^{\alpha_{12}}_{t}\varepsilon_{12}, \tag{5.52}$$

where $\mathrm{D}_t^{\alpha_{12}}$ is the fractional derivative of order α_{12}, being $0 < \alpha_{12} < 1$. The dissipation during the unloading, for its part, is given by

$$\Upsilon_{12}^{\mathrm{in}} = G_{12}^{\mathrm{v}} \mathrm{D}_t^{\alpha_{12}} \varepsilon_{12}^{\mathrm{i}} \cdot \dot{\varepsilon}_{12}^{\mathrm{i}}, \tag{5.53}$$

which must also be positive in order to fulfil the Clausius-Duhem inequality. According to the positiveness of the term of the dissipation (see Section 5.1.2), this models verifies the Clausius-Duhem inequality.

Numerical evaluation of the fractional model

The numerical evaluation of the fractional derivative of the strain and the stress in Eq. 5.52 has been achieved using of the L1-algorithm, following in the footsteps of Mateos et al. [2013]. Using Eg 2.12, the following expressions to calculate the fractional derivatives of such variables are obtained: for the strain,

$$\begin{aligned} {}_0^{\mathrm{L1}}\mathrm{D}_t^{\alpha_{12}} \varepsilon_{12}(t) =& \frac{(t/N)^{-\alpha_{12}}}{\Gamma(2-\alpha_{12})} \left[\frac{1-\alpha_{12}}{N^{\alpha_{12}}} \varepsilon_{12}(0) + \right. \\ & \left. \sum_{j=0}^{N-1} \left[\varepsilon_{12}\left(t - j\frac{t}{N}\right) - \varepsilon_{12}\left(t - (j+1)\frac{t}{N}\right) \right] \left[(j+1)^{1-\alpha_{12}} - j^{1-\alpha_{12}} \right] \right], \end{aligned} \tag{5.54}$$

and for the stress,

$$\begin{aligned} {}_0^{\mathrm{L1}}\mathrm{D}_t^{\alpha_{12}} \sigma_{12}(t) =& \frac{(t/N)^{-\alpha_{12}}}{\Gamma(2-\alpha_{12})} \left[\frac{1-\alpha_{12}}{N^{\alpha_{12}}} \sigma_{12}(0) + \right. \\ & \left. \sum_{j=0}^{N-1} \left[\sigma_{12}\left(t - j\frac{t}{N}\right) - \sigma_{12}\left(t - (j+1)\frac{t}{N}\right) \right] \left[(j+1)^{1-\alpha_{12}} - j^{1-\alpha_{12}} \right] \right], \end{aligned} \tag{5.55}$$

where N is the number of evaluation points.

Parameters identification and model implementation

In order to obtain the values for the parameters of the fractional model, an optimisation problem has been formulated aimed at minimising the error function

δ_e, which has been calculated adding all the individual data point errors in the interval considered. During the optimisation process, the state law (see Eq. 5.52) has been used. The error function δ_e, which is calculated from the error δ_e^m at the time t_m, has been defined as:

$$\delta_\mathrm{e} = \sum_{m=0}^{n} \delta_\mathrm{e}^m = \sum_{m=0}^{n} \left(\bar{\sigma}_{12}^m - \sigma_{12}^m\right)^2, \tag{5.56}$$

where $\bar{\sigma}_{12}^m$ and σ_{12}^m are the tensile stress value obtained from experimental tests and from the mathematical model, respectively, both evaluated at time t_m. The parameters of the model, G_{12}^*, G_{12}^m, G_{12}^v and α_{12}, can be then be obtained by minimising the error. Then, the implementation of the model (consisted of the elastoplatic and fractional viscoelastic formulations) is carried out following the scheme appearing in Algorithm 1, which is included in Appendix C.1.

Numerical results

In this section, the numerical results obtained with the fractional model for the three strain rates are presented. To do so, firstly, the suitability of the F-SLS model as a generalised one has been checked, considering the possibility that a particular case of such model was valid. Several trials of parameters identification of the F-SLS model have led G_{12}^m to acquire a value very similar to the shear modulus G_{12} as best alternative to reproduce every loop. Thus, it has been considered that G_{12}^m corresponds with G_{12}, which means that it is necessary to identify exclusively G_{12}^*, G_{12}^v and α_{12}.

Fig. 5.6 shows the evolution of the values of the parameters identified for each loop at 10^{-4} s^{-1}, 10^{-3} s^{-1} and 10^{-2} s^{-1} and the numerical approximations defined based on the accumulated plastic strain and Table 5.2 collects the form of the approximation functions used as well as the coefficients of such functions. The values identified for the parameters denote that a master curve for the three strain rates can be deduced.

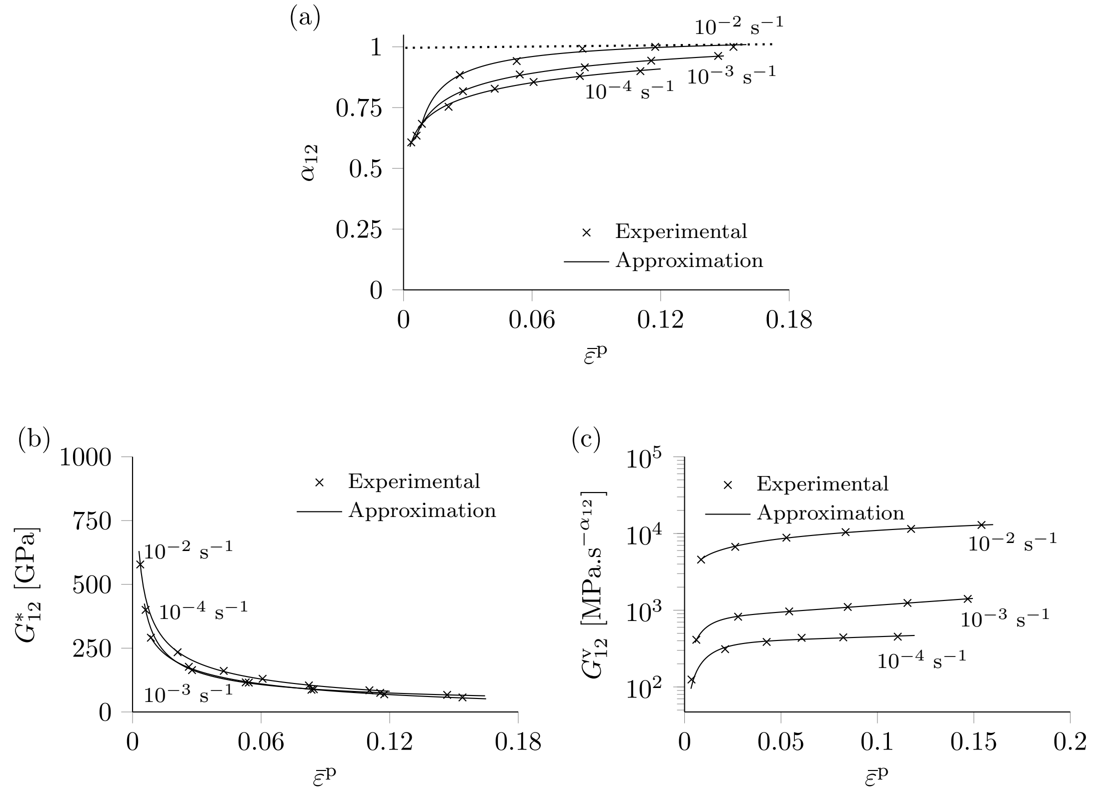

Figure 5.6: Experimental evolution and numerical approximation of (a) α_{12}, (b) G^*_{12} and (c) G^{v}_{12} depending on the accumulated plastic strain in shear at 10^{-4} s^{-1}, 10^{-3} s^{-1} and 10^{-2} s^{-1}.

Table 5.2: Coefficients of the numerical approximations of the evolution of the material parameters G^*_{12}, α_{12} and G^{v}_{12} of F-SLS model in shear.

$\dot{\varepsilon}_{12}$ [s^{-1}]	$G^*_{12} = a^*_{12}(\bar{\varepsilon}^{\mathrm{p}})^{b^*_{12}} + c^*_{12}$			$\alpha_{12} = a^{\alpha}_{12}(\bar{\varepsilon}^{\mathrm{p}})^{b^{\alpha}_{12}} + c^{\alpha}_{12}$			$G^{\mathrm{v}}_{12} = a^{\mathrm{v}}_{12}(1 - \exp(-b^{\mathrm{v}}_{12}\bar{\varepsilon}^{\mathrm{p}}))\exp(c^{\mathrm{v}}_{12}(\bar{\varepsilon}^{\mathrm{p}})^{1/2})$		
	a^*_{12}	b^*_{12}	c^*_{12}	a^{α}_{12}	b^{α}_{12}	c^{α}_{12}	a^{v}_{12}	b^{v}_{12}	c^{v}_{12}
10^{-4}	302.8	34.53	62.83	-0.01	-0.67	1.06	4832	152.8	2.54
10^{-3}	451.6	56.44	78.29	-0.21	-0.22	1.29	547.4	161.2	2.44
10^{-2}	601.0	68.62	106.0	-1.84	-0.04	2.91	305.5	109.1	1.25

5.2.3 Numerical-experimental correlation

Fig 5.7 shows the numerical-experimental correlation for the the three strain rates. As it can be seen, the model has the ability to reproduce accurately the envelope as well as the hysteresis loops in every cases. The root-mean-square error (RMSE) at 10^{-4} s^{-1}, 10^{-3} s^{-1} and 10^{-2} s^{-1} is 1.01%, 1.28% and 1.94%, respectively.

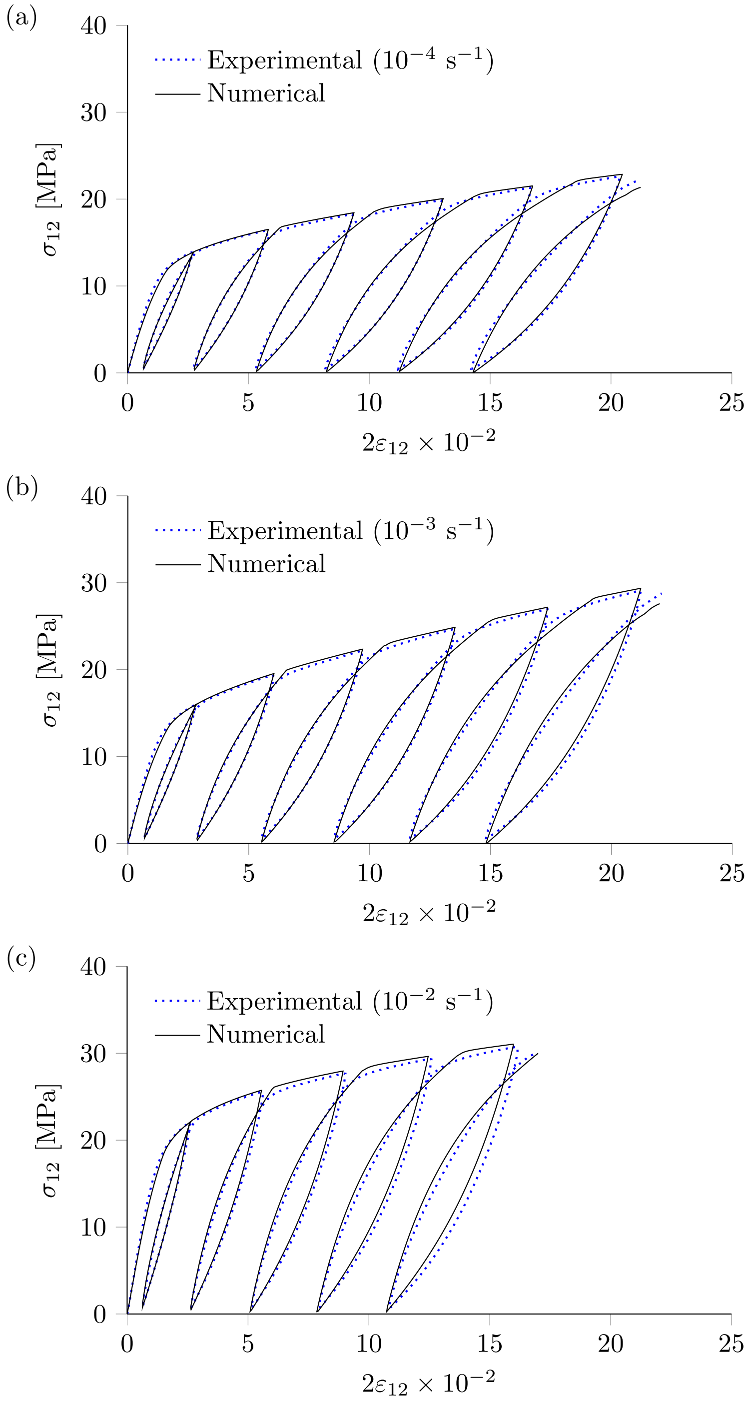

Figure 5.7: Experimental-numerical correlation of the shear stress-strain relation at 10^{-4} s^{-1}, 10^{-3} s^{-1} and 10^{-2} s^{-1}.

5.3 Cyclic tensile behaviour law

5.3.1 Elastoplastic modelling of the envelope

The free energy potential and the elastic damage law

Considering tensile conditions in direction 1, the Helmholtz's free energy for the enveloping of the cyclic stress-strain curve results

$$\rho\psi = \rho\psi(\varepsilon_{11}-\varepsilon_{11}^{\mathrm{p}}, d_{11}, r_{11}, \bar{\varepsilon}^{\mathrm{p}}) = \frac{1}{2}E_{11}^{0}(1-d_{11})(1+r_{11})(\varepsilon_{11}-\varepsilon_{11}^{\mathrm{p}})^2+h(\bar{\varepsilon}^{\mathrm{p}}), \quad (5.57)$$

where E_{11}^{0}, d_{11}, r_{11} and $\bar{\varepsilon}^{\mathrm{p}}$ stand for the undamaged elastic modulus, the damage variable associated to loss of stiffness, the stiffening variable and the accumulated plastic strain, respectively. Using the split of strain

$$\varepsilon_{11}^{\mathrm{e}} = \varepsilon_{11} - \varepsilon_{11}^{\mathrm{p}}, \quad (5.58)$$

Eq. 5.57 yields

$$\rho\psi = \frac{1}{2}E_{11}^{0}(1-d_{11})(1+r_{11})(\varepsilon_{11}^{\mathrm{e}})^2 + h(\bar{\varepsilon}^{\mathrm{p}}). \quad (5.59)$$

After differentiating this expression and substituting into the Clausius-Duhem inequality, the model for the tensile Cauchy's stress σ_{11}, the thermodynamic force Y_{11}, associated to the tensile damage variable; the thermodynamic force Z_{11}, associated to the tensile stiffening variable; and the thermodynamic force κ, associated to the accumulated plastic strain $\bar{\varepsilon}^{\mathrm{p}}$, are obtained:

$$\sigma_{11} = \rho\frac{\partial\psi}{\partial\varepsilon_{11}} = E_{11}^{0}(1-d_{11})(1-r_{11})(\varepsilon_{11}^{\mathrm{e}}) \quad (5.60)$$

$$Y_{11} = -\rho\frac{\partial\psi}{\partial d_{11}} = \frac{1}{2}E_{11}^{0}(1+r_{11})(\varepsilon_{11}^{\mathrm{e}})^2 \quad (5.61)$$

$$Z_{11} = -\rho\frac{\partial\psi}{\partial r_{11}} = -\frac{1}{2}E_{11}^{0}(1-d_{11})(\varepsilon_{11}^{\mathrm{e}})^2 \quad (5.62)$$

$$\kappa = \rho\frac{\partial\psi}{\partial\bar{\varepsilon}^{\mathrm{p}}} = \rho\frac{\partial h(\bar{\varepsilon}^{\mathrm{p}})}{\partial\bar{\varepsilon}^{\mathrm{p}}} = \kappa(\bar{\varepsilon}^{\mathrm{p}}), \tag{5.63}$$

The dissipation is given by

$$\Upsilon_{11}^{\mathrm{in}} = Y_{11}\dot{d}_{11} + Z_{11}\dot{r}_{11} + \kappa\dot{\bar{\varepsilon}}^{\mathrm{p}}, \tag{5.64}$$

which must be positive in order to fulfil the Clausius-Duhem inequality.

Experimental evolution laws

In this section, tensile damage and stiffening evolution laws, as well as the evolution of the tensile yield $\sigma_{\mathrm{y.11}}$ and the parameter a_1 are determined (remember that the hardening function has already been defined in Section 5.2.1). To do so, the irreversible strain $\varepsilon_{11}^{\mathrm{p}}$ and the stiffness variability ratio R_{s11} for every cycle of the shear stress-strain curve must be obtained. $\varepsilon_{11}^{\mathrm{p}}$ is necessary to obtain the evolution of $\sigma_{\mathrm{y.11}}$ and a_1; it results when the stress becomes zero. R_{s11} is required to determine the damage and stiffening evolution laws; it is obtained from the average slope within the loop E_{11} and the initial undamaged slope E_{11}^{0}.

According to Fig. 4.6, the evolution of $R_{\mathrm{s.11}}$ indicates that in direction 1 the material presents both damage and stiffening. Hence, the damage and stiffening evolution laws has been obtained according to the criterion stabilised in Section 4.2.1. Firstly, the damage evolution law has been estimated, making possible the calculation of the damage in each loop M by means of

$$d_{11}^{M} = f_{11}^{M}(Y_{11}^{M}), \tag{5.65}$$

which allows to obtain the stiffening stage in each loop, which is necessary to determine the corresponding stiffening law based on the expression defined for this purpose (see Eq. 4.20). This is

$$r_{11}^{M} = \frac{d_{11}^{M} - R_{\mathrm{s11}}^{\ M}}{1 - d_{11}^{M}}. \tag{5.66}$$

Assuming that damage during unloading remains constant until further positive loading is applied and causes further damage accumulation, the parameter $\bar{Y}_{11}$ is defined to describe the damage development. It is based on the maximum value reached by the thermodynamic damage force along the previous loading history;

$$\bar{Y}_{11} = \max_{\tau \leq t} \left(\sqrt{Y_{11}(\tau)} \right). \tag{5.67}$$

Then, the damage evolution law is defined as

$$d_{11} = f_{11}(\bar{Y}_{11}), \tag{5.68}$$

where f_{11} is the damage evolution function. From experimental data, an exponential evolution has seemed to be a proper form for the tensile damage evolution law;

$$d_{11} = f_{11}(\bar{Y}_{11}) = d_{11}^{\mathrm{s}} \left\langle 1 - \mathrm{e}^{-\beta_{11}\left(\bar{Y}_{11} - \sqrt{Y_{11}^{0}}\right)} \right\rangle_{+} \quad \text{if} \quad d_{11} < 1 \quad \text{and} \quad \bar{Y}_{11} < \sqrt{Y_{11}^{\mathrm{c}}}, \tag{5.69}$$

where $\langle \rangle_+$ is the Macaulay bracket, Y_{11}^{c} is the damage critical thermodynamic force; Y_{11}^{0}, the damage initiation thermodynamic force; d_{11}^{s}, the damage saturation; and β_{11}, a coefficient related to damage saturation rate.

Assuming that stiffening during unloading remains constant until further positive loading is applied and causes further stiffening, the parameter $\bar{Z}_{11}$ is defined to describe the stiffening development. It is based on the maximum value reached by the thermodynamic stiffening force along the previous loading history;

$$\bar{Z}_{11} = \max_{\tau \leq t} \left(\sqrt{Z_{11}(\tau)} \right). \tag{5.70}$$

Then, the stiffening evolution law is defined as

$$r_{11} = g_{11}(\bar{Z}_{11}), \tag{5.71}$$

where g_{11} is the stiffening evolution function. From experimental data, an exponential evolution was found to be a good approach for the tensile stiffening evolution law;

$$r_{11} = g_{11}(\bar{Z}_{11}) = r_{11}^{\mathrm{s}} \left\langle 1 - \mathrm{e}^{-\gamma_{11}\left(\bar{Z}_{11} - \sqrt{Z_{11}^{0}}\right)} \right\rangle_{+}, \tag{5.72}$$

where Z_{11}^{0} is the stiffening initiation thermodynamic force; r_{11}^{s}, a material parameter; and γ_{11}, another material parameter.

Concerning the evolution of $\sigma_{y.11}$, a potential evolution has seemed to be a proper form to reproduce the corresponding curve:

$$\sigma_{y.11} = \sigma_{y0.11} + K_{11}(\bar{\varepsilon}^{\mathrm{p}})^{m_{11}}, \tag{5.73}$$

where $\sigma_{y0.11}$, K_{11} and m_{11} are material parameters.

Concerning the evolution of a_1, an exponential form has seemed to be a proper form to reproduce the corresponding curve:

$$a_1 = a + b\exp(-c\bar{\varepsilon}^{\mathrm{p}}), \tag{5.74}$$

where a, b and c are material parameters.

Fig. 5.8 shows the (a) damage and (b) stiffening experimental data as well as their respective evolution laws and Table 5.3 collects the value of the parameters of such laws for the three strain rates.

Fig. 5.9 shows the (a) tensile yield experimental data as well as its respective evolution law $\sigma_{\mathrm{y}.11}(\bar{\varepsilon}^{\mathrm{p}})$ and (b) the evolution of $a_1(\bar{\varepsilon}^{\mathrm{p}})$, which has been deduced from $\sigma_{\mathrm{y}}(\bar{\varepsilon}^{\mathrm{p}})$ (hardening function) and $\sigma_{\mathrm{y}.11}(\bar{\varepsilon}^{\mathrm{p}})$. Table 5.4 collects the value of the parameters of $\sigma_{\mathrm{y}.11}(\bar{\varepsilon}^{\mathrm{p}})$ and $a_1(\bar{\varepsilon}^{\mathrm{p}})$.

At this point, the tensile elastoplastic model is completely defined. Fig. 5.10 shows the response of the model at the three strain rates. The model reproduces accurately the envelopes of the tensile stress-strain curves; however, it considers that the unload is linear. In the following section, this imprecision of the model is resolved using the fractional viscoelastic model to reproduce the hysteresis loops.

Table 5.3: Value of the parameters of the damage and stiffening evolution laws for the three strain rates.

$\dot{\varepsilon}_{11}$ [s^{-1}]	Damage parameters			Stiffening parameters		
	d_{11}^{s}	β_{11} [MPa$^{-1/2}$]	Y_{11}^0 [MPa$^{1/2}$]	r_{11}^{s}	γ_{11} [MPa$^{-1/2}$]	Z_{11}^0 [MPa$^{1/2}$]
10^{-4}	0.55	2.43	0.14	0.48	1.05	0.64
10^{-3}	0.52	2.72	0.19	0.45	1.28	0.68
10^{-2}	0.53	2.50	0.21	0.46	0.45	0.81

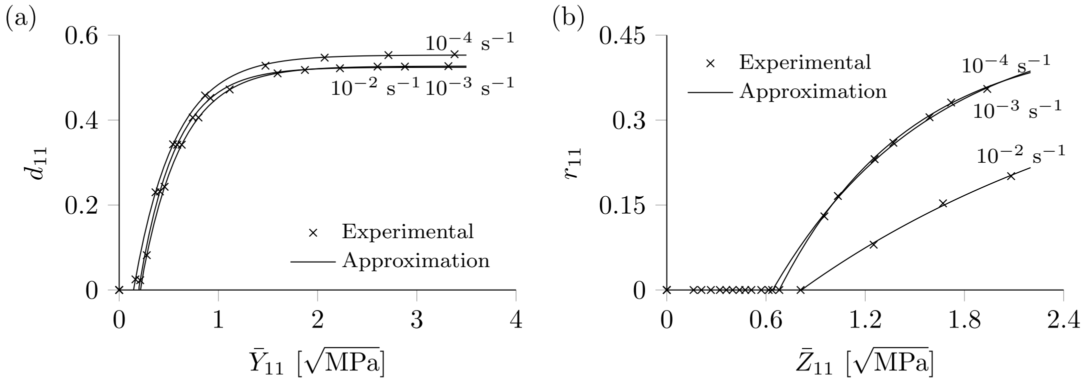

Figure 5.8: (a) Damage and (b) stiffening tensile evolution laws in direction 1 for the three strain rates.

Table 5.4: Value of the parameters of the tensile yield and $a_1(\bar{\varepsilon}^{\mathrm{p}})$ evolution laws for the three strain rates.

$\dot{\varepsilon}_{11}$ [s^{-1}]	$\sigma_{y.11} = \sigma_{y0.11} + K_{11}(\bar{\varepsilon}^{\mathrm{p}})^{m_{11}}$			$a_1 = a + b\exp(-c\bar{\varepsilon}^{\mathrm{p}})$		
	$\sigma_{\mathrm{y0.11}}$	K_{11}	m_{11}	a	b	c
10^{-4}	37.73	6244	1.351	0.1507	0.2231	7.039
10^{-3}	38.24	4221	1.156	0.1862	0.2003	10.12
10^{-2}	46.94	3446	0.988	0.1554	0.214	10.28

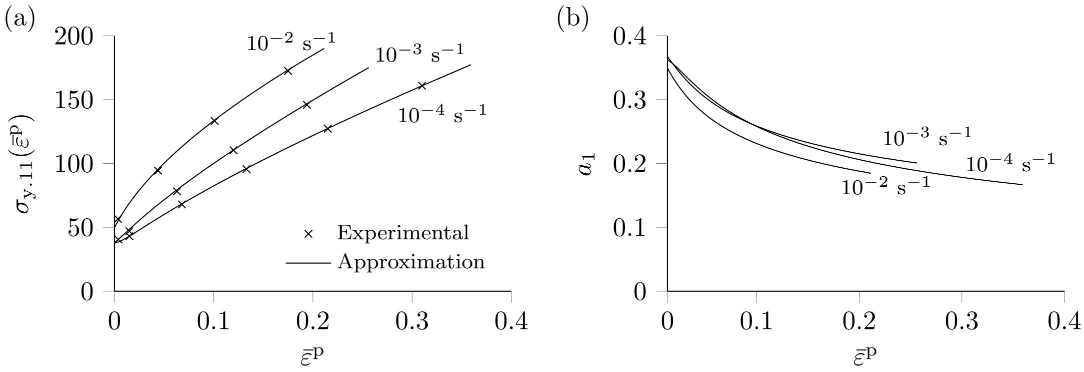

Figure 5.9: (a) Tensile yield and (b) $a_1(\bar{\varepsilon}^p)$ evolution laws in direction 1 for the three strain rates.

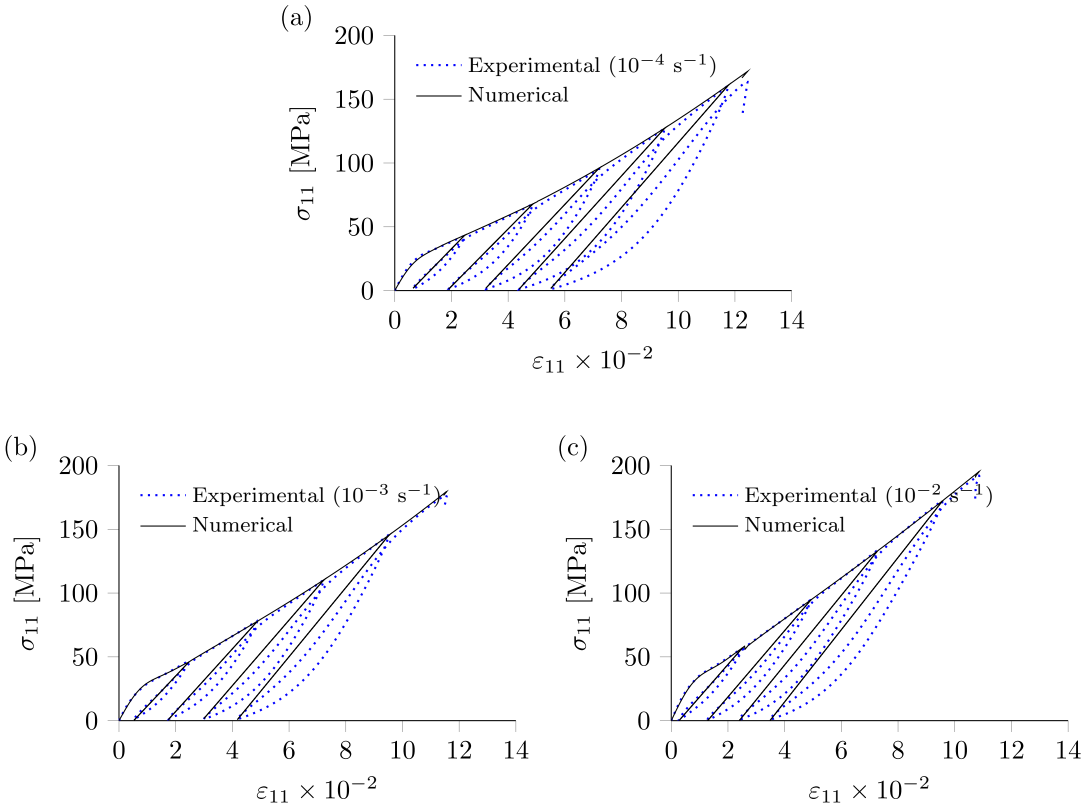

Figure 5.10: Numerical-experimental correlation in tensile in 1-direction at (a) 10^{-4} s^{-1}, (b) 10^{-3} s^{-1} and (c) 10^{-2} s^{-1} considering the elastoplastic damage model, which predicts the envelope of each curve.

5.3.2 Fractional viscoelastic modelling of the hysteresis loops

The free energy potential and the fractional viscoelastic law

Given the tensile conditions, the rheological model can be represented as Fig. 5.11 shows.

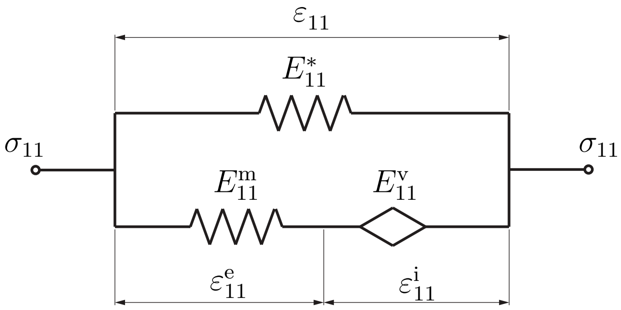

Figure 5.11: Rheological representation of the shear F-SLS model.

The Helmholtz's free energy for the hysteresis loops results

$$\rho\psi(\varepsilon_{11},\varepsilon^{\mathrm{i}}_{11}) = \frac{1}{2}E^{*}_{11}\varepsilon^{2}_{11} + \frac{1}{2}E^{\mathrm{m}}_{11}(\varepsilon_{11} - \varepsilon^{\mathrm{i}}_{11})^{2}, \tag{5.75}$$

where E^{*}_{11} and E^{m}_{11} are material parameters.

After differentiating Eq. 5.75 and substituting into the Clausius-Duhem inequality, the following non-standard model for the Cauchy's tensile stress σ_{11} is proposed;

$$\sigma_{11} = \rho\frac{\partial\psi}{\partial\varepsilon_{11}} = E^{*}_{11}\varepsilon_{11} + E^{\mathrm{m}}_{11}(\varepsilon_{11} - \varepsilon^{\mathrm{i}}_{11}). \tag{5.76}$$

Then, considering that

$$E^{\mathrm{m}}_{11}(\varepsilon_{11} - \varepsilon^{\mathrm{i}}_{11}) = E^{\mathrm{v}}_{11}\mathrm{D}^{\alpha}_{t}\varepsilon^{\mathrm{i}}, \tag{5.77}$$

after working appropriately with Eq. 5.76 and reorganising the terms, the state law can be represented as a function exclusively of the toal strain ε_{11}, yielding

$$\sigma_{11}+\frac{E_{11}^{\mathrm{v}}}{E_{11}^{\mathrm{m}}}\mathrm{D}_t^{\alpha}\sigma_{11}=E_{11}^{*}\varepsilon_{11}+\frac{E_{11}^{*}+E_{11}^{\mathrm{m}}}{E_{11}^{\mathrm{m}}}E_{11}^{\mathrm{v}}\mathrm{D}_t^{\alpha}\varepsilon_{11}, \tag{5.78}$$

where D_t^{α} is the fractional derivative of order α, being $0<\alpha<1$. The dissipation during the unloading, for its part, is given by

$$\Upsilon_{11}^{\mathrm{in}}=E_{11}^{\mathrm{v}}\mathrm{D}_t^{\alpha}\varepsilon_{11}^{\mathrm{i}}\cdot\dot{\varepsilon}_{11}^{\mathrm{i}}, \tag{5.79}$$

which must also be positive in order to fulfil the Clausius-Duhem inequality. According to the positiveness of the term of the dissipation (see Section 5.1.2), this models verifies the Clausius-Duhem inequality.

The formulation associated to the tensile behaviour which has been developed until now is based on a elastoplastic model (for the envelope) and a fractional model (for the hysteresis loops). However, according to Fig. 4.5, the stress-strain relation of the reloads, which is non-linear, can be approximated by a linear form, whose slope changes with the strain, as it can be seen subsequently. Form now on, this reloading slope will be referred to as E_{11}^{r} and will be used to model the reloads based on a linear elastic model.

Numerical evaluation of the fractional model

As in the shear case, the L1-algorithm has been used to achieve the numerical evaluation of the fractional derivative of the strain and the stress in Eq. 5.78. Then, using Eq. 2.12, the following expressions to calculate the fractional derivatives of such variables are obtained: for the strain,

$$\begin{aligned}{}_{0}^{\mathrm{L1}}\mathrm{D}_t^{\alpha_{11}}\varepsilon_{11}(t)=&\frac{(t/N)^{-\alpha_{11}}}{\Gamma(2-\alpha_{11})}\left[\frac{1-\alpha_{11}}{N^{\alpha_{11}}}\varepsilon_{11}(0)+\right.\\&\left.\sum_{j=0}^{N-1}\left[\varepsilon_{11}\left(t-j\frac{t}{N}\right)-\varepsilon_{11}\left(t-(j+1)\frac{t}{N}\right)\right]\left[(j+1)^{1-\alpha_{11}}-j^{1-\alpha_{11}}\right]\right],\end{aligned} \tag{5.80}$$

and for the stress,

$$
\begin{aligned}
{}^{\mathrm{L1}}_{\ 0}\mathrm{D}_t^{\alpha_{11}}\sigma_{11}(t) =& \frac{(t/N)^{-\alpha_{11}}}{\Gamma(2-\alpha_{11})}\left[\frac{1-\alpha_{11}}{N^{\alpha_{11}}}\sigma_{11}(0) + \right.\\
& \left. \sum_{j=0}^{N-1}\left[\sigma_{11}\left(t - j\frac{t}{N}\right) - \sigma_{11}\left(t-(j+1)\frac{t}{N}\right)\right]\left[(j+1)^{1-\alpha_{11}} - j^{1-\alpha_{11}}\right]\right],
\end{aligned}
\tag{5.81}
$$

where N is the number of evaluation points.

Parameters identification and model implementation

In order to obtain the values for the parameters of the fractional model, another optimisation problem similar to that of the shear case has been formulated. In this case, Eq. 5.52 has been used. The type of error function used has been the same:

$$
\delta_{\mathrm{e}} = \sum_{m=0}^{n}\delta_{\mathrm{e}}^{m} = \sum_{m=0}^{n}\left(\bar{\sigma}_{11}^{m} - \sigma_{11}^{m}\right)^2, \tag{5.82}
$$

where $\bar{\sigma}_{11}^{m}$ and σ_{11}^{m} are the tensile stress values obtained from experimental tests and from the mathematical model, respectively, both evaluated at time t_m. The parameters of the model, E_{11}^{*}, E_{11}^{m}, E_{11}^{v} and α_{11} can be then be obtained by minimising the error. Then, the implementation of the model (consisted of the elastoplatic, fractional viscoelastic and linear elastic formulations for the envelope, the unloads and the reloads, respectively) is carried out following the scheme appearing in Algorithm 1, which is included in Appendix C.1.

Numerical results

In this section, the numerical results obtained with the fractional model for the three strain rates are presented. To do so, firstly, the suitability of the F-SLS model as a generalised one has been checked, considering the possibility that a particular case of such model was valid. Several trials of parameters identification of the F-SLS model have led E_{11}^{*} and α to become zero and one, respectively, as best alternative to reproduce every semi-loop. This means that non-fractional Maxwell model has been selected to model the unloading semi-loops, which has supposed that only the identification of E^{m}_{11} and E^{v}_{11} is needed.

Fig. 5.12 shows the value of the parameters identified for each semi-loop at 10^{-4} s^{-1}, 10^{-3} s^{-1} and 10^{-2} s^{-1} and the numerical approximations defined based on the tensile plastic strain. Table 5.5 collects the form of the approximation functions used as well as the coefficients of such functions. The values identified for the parameters denote that a master curve for the three strain rates can be deduced.

Fig 5.13 shows the evolution of E^{r}_{11} with $\varepsilon^{\mathrm{p}}_{11}$ and Table 5.6 shows the coefficients of their numerical approximations. E^{r}_{11} evolves linearly and the higher the strain rate, the higher its value.

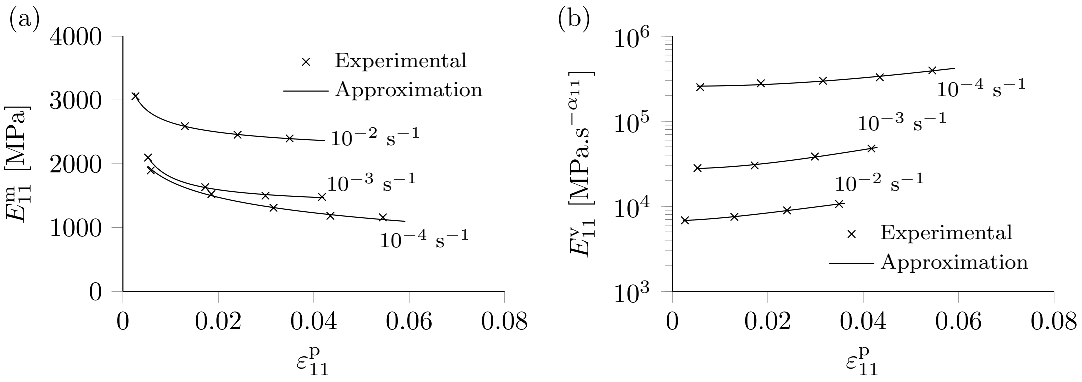

Figure 5.12: Experimental evolution and numerical approximation of (a) $E^{\mathrm{m}}_{\mathrm{u}.11}$ and (b) $E^{\mathrm{v}}_{\mathrm{u}.11}$ depending on the accumulated plastic strain in tensile in 1-direction at 10^{-4} s^{-1}, 10^{-3} s^{-1} and 10^{-2} s^{-1}.

Table 5.5: Coefficients of the numerical approximations of the evolution of the material parameters $E^{\mathrm{m}}_{\mathrm{u}.11}$ and $E^{\mathrm{v}}_{\mathrm{u}.11}$ of the Maxwell model for the 1-direction tensile behaviour.

$\dot{\varepsilon}_{11}$ [s^{-1}]	$E^{\mathrm{m}}_{11} = a^{\mathrm{m}}_{11}\exp(-b^{\mathrm{m}}_{11}\bar{\varepsilon}^{\mathrm{p}}) + c^{\mathrm{m}}_{11}$			$E^{\mathrm{v}}_{11} = a^{\mathrm{v}}_{11}(\varepsilon^{\mathrm{p}}_{11})^{b^{\mathrm{v}}_{11}} + c^{\mathrm{v}}_{11}$		
	a^{m}_{11}	b^{m}_{11}	c^{m}_{11}	a^{v}_{11}	b^{v}_{11}	c^{v}_{11}
10^{-4}	1100	-47.86	1066	9.88×10^{7}	2.27	2.578×10^{4}
10^{-3}	1137	-111.3	1465	1.25×10^{7}	2.022	2.751×10^{4}
10^{-2}	907.2	-113.7	2386	8.11×10^{5}	1.592	6.758×10^{3}

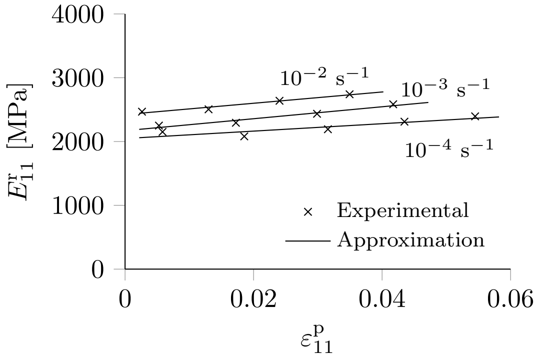

Figure 5.13: Experimental evolution and numerical approximation of $E_{\mathrm{r}.11}$ depending on the tensile plastic strain $\varepsilon^{\mathrm{p}}_{11}$ in tensile in 1-direction at 10^{-4} s^{-1}, 10^{-3} s^{-1} and 10^{-2} s^{-1}.

Table 5.6: Coefficients of the numerical approximations of the evolution of the reloading slope $E_{\mathrm{r}.11}$ with $\bar{\varepsilon}^{\mathrm{p}}$ in tensile in 1-direction at 10^{-4} s^{-1}, 10^{-3} s^{-1} and 10^{-2} s^{-1}.

$\dot{\varepsilon}_{11}$ [s^{-1}]	$E^{\mathrm{r}}_{11} = a^{\mathrm{r}}_{11}(\varepsilon^{\mathrm{p}}_{11}) + b^{\mathrm{r}}_{11}$	
	a^{r}_{11}	b^{r}_{11}
10^{-4}	5813	2047
10^{-3}	9373	2170
10^{-2}	8842	2423

5.3.3 Numerical-experimental correlation

Fig 5.14 shows the numerical-experimental correlation for the the three strain rates. As it can be seen, the model has the ability to reproduce accurately the envelope as well as the unloads in every cases. Concerning the reloads, a slightly difference increasing with strain rate is appreciated between the prediction and the experimental data. Such difference is caused by a progressive loss of linearity in the reloads when strain rate is increased. The root-mean-square error (RMSE) at 10^{-4} s^{-1}, 10^{-3} s^{-1} and 10^{-2} s^{-1} is 7.36%, 8.03% and 9.12%, respectively.

5.4 Conclusions

In this chapter, a constitutive model of the cyclic quasi-static behaviour of the SRPP is formulated within the framework of thermodynamics of irreversible processes. The proposed model consists of two parts or submodels: one associ-

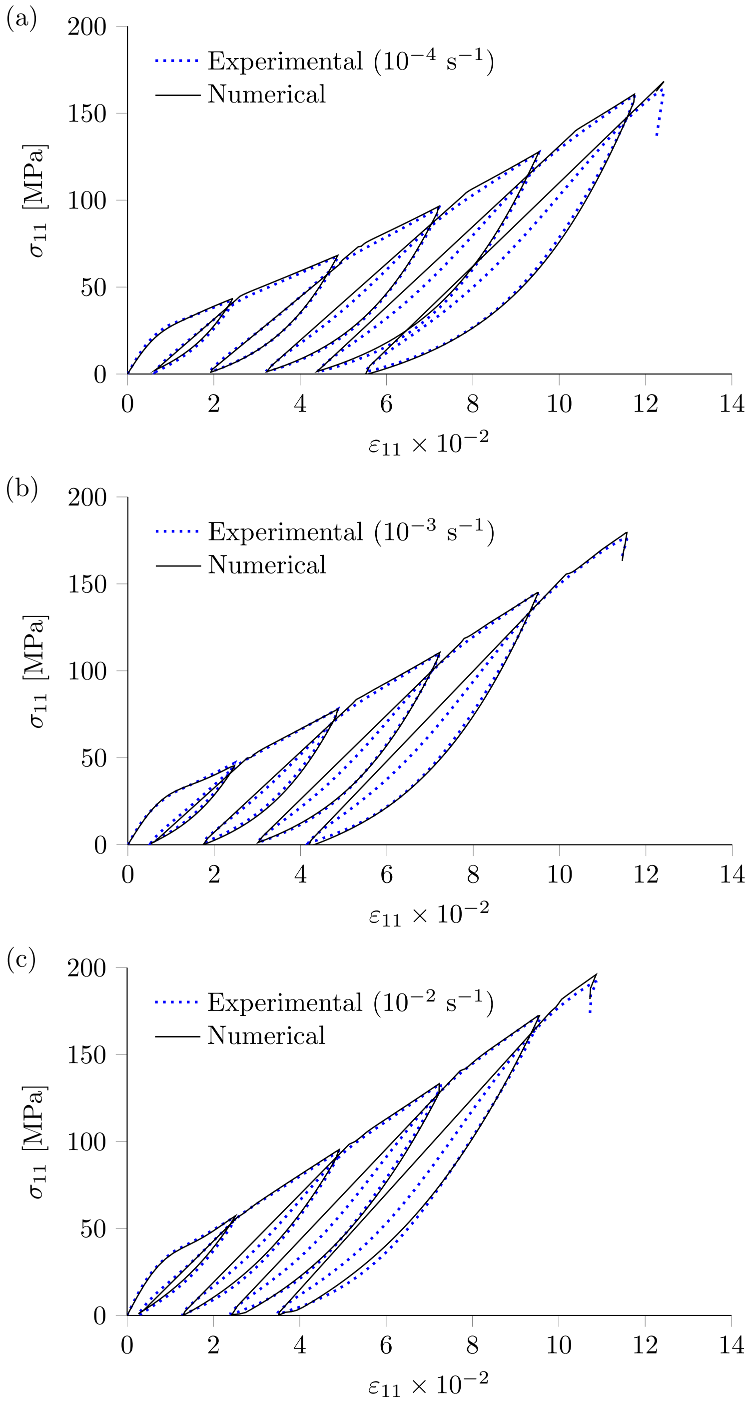

Figure 5.14: Experimental-numerical correlation of the tensile stress-strain relation in 1-direction at (a) 10^{-4} s^{-1}, (b) 10^{-3} s^{-1} and (c) 10^{-2} s^{-1}.

ated to the envelopes of the stress-strain relations of both tensile and shear and another one formulated to reproduce independently the hysteresis phenomena appearing in both tensile and shear.

The model of the envelopes is based on an elastoplastic formulation which considers the stiffness variation caused by damage generation (in both tensile and shear) and stiffening caused by chains orientation (in tensile). The model of the hysteresis loops is based on a fractional solid linear standard (F-SLS) formulation in the shear case, and a combination of a F-SLS (unloading part of the loop) and an elastic (reloading part of the loop) formulations in the tensile case.

The numerical-experimental correlation has demonstrated that the model is capable of predicting accurately both the cyclic tensile and shear behaviours of the SRPP, so that can be stated that the use of the combination of an elasto-plastic model and a fractional viscoelastic one is valid to predict the quasi-static behaviour of plain SRCs.

Chapter 6

General conclusions and future work

6.1 Conclusions

This research work has dealt with the mechanical behaviour of SRC-based FMLs. Firstly, the most appropriate SRC-FML, between an Al-based FML and a Mg-based FML, for low-velocity impact applications in terms of energy dissipation capacity has been chosen (Chapter 3). Secondly, the mechanical behaviour of the composite constituent, SRPP, has been characterised and its influence in the mechanical response of the FML has been evaluated (Chapter 4). Finally, given the relevance of the of the SRPP in this last issue, a material model of the SRPP has been formulated (Chapter 5).

In the first part of Chapter 3, the low-velocity impact behaviour of three different SRCs have been studied: a SRPP, a SRPET and a SRPE. On the one hand, the SRPE have demonstrated the highest energy dissipation capacity due to the relatively large deformation of the material; however, this seems to be associated to an inappropriate compaction temperature which causes a wrinkling phenomenon. On the other hand, the SRPP and the SRPET have qualitatively shown the same kind of response; nevertheless, quantitatively, the SRPP has demonstrated almost twice penetration energy than the SRPET. These results suggest rejecting the SRPE as alternative for the FMLs and selecting the SRPP as the material that shows the most appropriate response under low-velocity impacts due to its capacity to dissipate impact energy at perforation. In the second part the chapter, two different SRPP-based FMLs have been studied; one with AZ31B-H24 magnesium and another one with 2024-T3 aluminium as metal constituents. The Al-FML has demonstrated higher perforation resistance and energy dissipation capacity than the Mg-FML. In fact, despite the latter presents lower density than the former, the perforation threshold of the Al-based laminate has resulted more than twice the one of the Mg-based FML.

In the first part of Chapter 4, the SRPP has been characterised at different strain rates. The SRPP has revealed that, when submitted to both tensile and shear stress solicitations, presents irreversible strains when deformed, hysteresis phenomena when submitted to load-unload cycles, a rate-dependent behaviour and a stiffness varying with the strain. In the second part of Chapter 4, the tensile mechanical response at different strain-rates of Al/SRPP-FML has been studied and the influence of the SRPP as constituent material in the FML has been evaluated. The FML has demonstrated a rate-dependent behaviour. Besides, when submitted to load-unload cycles, it showed hysteresis loops. These phenomena are attributed to the presence of the SRPP, which affects significantly to the mechanical behaviour of the FML. This implies that the rate-dependent mechanical behaviour of the SRPP must be considered to model the mechanical response of the Al/SRPP-FML.

In Chapter 5, a constitutive model within the framework of thermodynamics of irreversible processes of the mechanical behaviour of the SRPP has been formulated. The numerical-experimental correlation has demonstrated that the model is capable of predicting accurately both the cyclic tensile and shear behaviours of the SRPP. It can be stated that the use of the combination of an elastoplastic model and a fractional viscoelastic one may be valid to predict the quasi-static behaviour of another SRCs.

6.2 Future work

In the present work, the low-velocity impact behaviour of three SRCs (SRPP, SRPET and SRPE) and two SRPP-FMLs: one based on aluminium and another one based on magnesium have been studied. After selecting the Al/SRPP-FML as object of study, the influence of the SRPP, as composite constituent, in the mechanical response of the FML is evaluated based on strain rate. Given the significant effect of the composite, it is determined the necessity of characterising and modelling its mechanical behaviour in a first step in order to predict accurately the mechanical response of the SRC-FMLs.

While it is true that the Al/SRPP-FML has been selected according to some criteria, it should be studied another alternative SRC-FMLs consisting of another SRCs such as SRPET or SRPE.

This thesis ends proposing a constitutive model of the quasi-static cyclic behaviour of the SRPP considering hysteresis phenomena and stiffness varying with strain. The evolution with the plastic strain of the values of the model parameters for the three strain rates studied denotes that master curves can be deduced and, hence, a rate-dependent model can be determined. However, to predict the response of SRC-FML when submitted to low-velocity impact solicitations, a rate-dependent model would be necessary of the behaviour of the SRPP. For this, the mechanical behaviour of the SRPP should be characterised at higher strain rates than the ones used in this thesis.

The modelling methodology implies the combination of a elastoplastic model for the envelope and a fractional viscoelastic model for the hysteresis loops of the stress-strain relation. It should be checked the validity of the proposed model for other SRCs.

The model is capable of predicting the stress-strain response both in tensile and in pure shear conditions by using an anisotropic yield criteria proposed specifically for composites presenting yield phenomenon in fibre directions. It should be checked the validity of the that criterion for multiaxial solicitations. To do so, it would be necessary experimental data provided by a cruciform multiaxial testing machine or if possible a tensile testing machine preventing from significant distortion of the angle defined by the fibres of the fabric.

References

ASTM D638-14, Standard Test Method for Tensile Properties of Plastics. xiv, 58, 62

Directive 2000/53/EC of the European Parliament and of the Council on end-of life vehicles. *Official Journal of the European Communities*, 2000. 17, 18

The Plastiky Expedition; catamaran made of SRPET produced by Comfil ApS. http://www.theplastiki.com/, 2010. 19

Don & Low Company. Armordon™ (Self-Reinforced Polypropylene, SRPP) http://www.donlow.co.uk/Armordon, 2015. 19

Lacks Enterprises, Inc. Chromtec® – Composite wheel systems. http://www.lacksenterprises.com/, 2015. 10

Comfil ApS. Comfil® (self-reinforced poly(ethylene) terephthalate, SRPET) http://www.comfil.biz/products/srp.php, 2015. xvii, 32

Propex Fabrics, Inc. Curv® (self-reinforced polypropylene, SRPP) http://www.propexbrands.com/, 2015. xvii, 19, 32

Lankhorst Pure Composites b.v. PURE® (self-reinforced polypropylene, SRPP) http://www.pure-composites.com/, 2015. 19

Milliken & Company. Tegris® (self-reinforced polypropylene, SRPP) http://www.milliken.com/en-us/pands/Pages/composites.aspx, 2015. 19

Scope Metals Ltd., 2015. xvii, 41

Collano Adhesives. Collano$^{®}$ (Hot melt adhesive film) http://www.collano.com/, 2015. xvii, 38, 41

Magnesium Electron, Ltd., 2015. xvii, 41

H.M. Srivastara A.A. Kilbas and J.J. Trujillo. *Theory and aplications of fractional differential equations*. Boston, 2006. 25

M.R. Abdullah and W.J. Cantwell. The impact resistance of polypropylene-based fibre-metal laminates. *Composites Science and Technology*, 66(11-12): 1682–1693, 2006a. ISSN 0266-3538. xi, 3, 16, 20, 21

M.R. Abdullah and W.J. Cantwell. The impact resistance of fiber-metal laminates based on glass fiber reinforced polypropylene. *Polymer Composites*, 27(6):700–708, 2006b. 3, 20

M.R. Abdullah and W.J. Cantwell. The high velocity impact response of self-reinforced polypropylene fibre metal laminates. In *Damage and Fracture of Composite Materials and Structures*, volume 17 of *Advanced Structured Materials*, pages 219–240. Springer Berlin Heidelberg, 2012. ISBN 978-3-642-23658-7. xi, 20, 21

N.H. Abel. Solution de quelques problèmes à laide dint égrales définies. *Ouvres complétes*, 1:16–18, 1881. 25

K. Adolfsson, M. Enelund, and P. Olsson. On the fractional order model of viscoelasticity. *Mechanics of Time-Dependent Materials*, 9(1):15–34, 2005. 23

M. Aktas, C. Atas, B.M. Iten, and R. Karakuzu. An experimental investigation of the impact response of composite laminates. *Composite Structures*, 87(4): 307–313, 2009. ISSN 0263-8223. 33

B. Alcock, N.O. Cabrera, N.-M. Barkoula, J. Loos, and T. Peijs. The mechanical properties of unidirectional all-polypropylene composites. *Composites Part A: Applied Science and Manufacturing*, 37(5):716–726, 2006. ISSN 1359-835X. 17

B. Alcock, N.O. Cabrera, N.-M. Barkoula, A.B. Spoelstra, J. Loos, and T. Peijs. The mechanical properties of woven tape all-polypropylene composites. *Composites Part A: Applied Science and Manufacturing*, 38(1):147–161, 2007. ISSN 1359-835X. 17

R. Alderliesten, C. Rans, and R. Benedictus. The applicability of magnesium based fibre metal laminates in aerospace structures. *Composites Science and Technology*, 68(14):2983–2993, 2008. ISSN 0266-3538. 12, 40

O. Allix, P. Ladeveze, L. Gornet, D. Leveque, and L. Perret. A computational damage mechanics approach for laminates: Identification and comparison with experimental results. *Damage Mechanics in Engineering Materials, Studies in Applied Mechanics*, pages 481–500, 1998. 21

J. Aurrekoetxea, M. Sarrionandia, M. Mateos, and L. Aretxabaleta. Repeated low energy impact behaviour of self-reinforced polypropylene composites. *Polymer Testing*, 30(2):216–221, 2011. ISSN 0142-9418. 3, 18, 22

R.L. Bagley and P.J. Torvik. Fractional calculus - a different approach to the analysis of viscoelastically damped structures. *AIAA journal*, 21(5):741–748, 1983. 23

R.L. Bagley and P.J. Torvik. On the fractional calculus model of viscoelastic behaviour. *Journal of Rheology*, 30(1):133–155, 1986. 23

D.M. Bigg. The impact behavior of thermoplastic sheet composites. *Journal of Reinforced Plastics and Composites*, 13(4):339–354, 1994. 17

C. Bois. *Mesure et prévision de lévolution des endommagements dans les composites stratifiés.* PhD thesis, Universite de la Méditerranée Aix-Marseille II, 2003. 22, 126

L.R. Le Bourlegat, C.A. Damato, D.F. Da Silva, E.C. Botelho, and L.C. Pardini. Processing and mechanical characterization of titanium-graphite hybrid laminates. *Journal of Reinforced Plastics and Composites*, 29(22):3392–3400, 2010. 13, 16

N.O. Cabrera, C.T. Reynolds, B. Alcock, and T. Peijs. Non-isothermal stamp forming of continuous tape reinforced all-polypropylene composite sheet. *Composites Part A: Applied Science and Manufacturing*, 39(9):1455–1466, 2008. ISSN 1359-835X. 18

W.J. Cantwell, G. Wade, J.F. Guillen, G.R.-V.N. Jones, and P. Compston. The high velocity impact response of novel fiber metal laminates. volume 250, pages 1–11, 2001. 20

W.J. Cantwell, N. Jones, G.A. Wade, G. Reyes, J.F. Guillen, and P. Compston. The impact response of novel fibre metal laminates. *High Performance Structures and Materials*, 4:33–45, 2002. 20

N.J. Capiati and R.S. Porter. The concept of one polymer composites modelled with high density polyethylene. *Journal of Materials Science*, 10:1671–1677, 1975. ISSN 0022-2461. 18

M. Caputo. Linear models of dissipaton whose q is almost frequency independet ii. *Geophys. J. Royal astr. Soc.*, 13:529–539, 1967. 25

M. Caputo. *Elasticitá e dissipazione*. Zanichelli, Bologna, 1969. 23

M. Caputo and F. Mainardi. Linear models of dissipation in anelastic solids. *La Rivista del nuovo cimento*, 1(2):161–198, 1971. 23

R.M. Christensen. Chapter I - Viscoelastic Stress Strain Constitutive Relations. In R.M. Christensen, editor, *Theory of Viscoelasticity (SECOND EDITION)*, pages 1–34. Academic Press, second edition edition, 1982. ISBN 978-0-12-174252-2. 123

P. Compston, W.J. Cantwell, C. Jones, and N. Jones. Impact perforation resistance and fracture mechanisms of a thermoplastic based fiber-metal laminate. *Journal of Materials Science Letters*, 20(7):597–9, 2001. ISSN 0261-8028. 16, 17

P. Compston, W.J. Cantwell, M.J. Cardew-Hall, S. Kalyanasundaram, and L. Mosse. Comparison of surface strain for stamp formed aluminum and an aluminum-polypropylene laminate. *Journal of Materials Science*, 39(19):6087–6088, 2004. ISSN 0022-2461. 18

P. Cortés and W.J. Cantwell. Interfacial fracture properties of carbon fiber reinforced peek/titanium fiber-metal laminates. *Journal of Materials Science Letters*, 21(23):1819–1823, 2002. 13

P. Cortés and W.J. Cantwell. The tensile and fatigue properties of carbon fiber-reinforced peek-titanium fiber-metal laminates. *Journal of Reinforced Plastics and Composites*, 23(15):1615–1623, 2004. 13, 16

P. Cortés and W.J. Cantwell. The mechanical properties of high temperature fibre-metal laminates. *Advanced Materials and Processes*, 163(4):31, 2005. 13, 16

P. Cortés and W.J. Cantwell. The prediction of tensile failure in titanium-based thermoplastic fibre-metal laminates. *Composites Science and Technology*, 66 (13):2306–2316, 2006a. 13, 16

P. Cortés and W.J. Cantwell. The fracture properties of a fibre-metal laminate based on magnesium alloy. *Composites Part B: Engineering*, 37(2-3):163–170, 2006b. ISSN 13598368. xi, 11, 12, 13

P. Cortés and W.J. Cantwell. Structure-properties relations in titanium-based thermoplastic fiber-metal laminates. *Polymer Composites*, 27(3):264–270, 2006c. 13, 16

P. Cortés and W.J. Cantwell. The impact properties of high-temperature fiber-metal laminates. *Journal of Composite Materials*, 41(5):613–632, 2007. xi, 14, 15, 16

P. Cortés, W.J. Cantwell, and K.S.C. Kuang. The fracture properties of a smart fiber metal laminate. *Polymer Composites*, 28(4):534–544, 2007. 15, 16

P. Cortés, W.J. Cantwell, K.S.C. Kuang, and S.T. Quek. The morphing properties of a smart fiber metal laminate. *Polymer Composites*, 29(11):1263–1268, 2008. 15, 16

P. Cosson. *Contribution à la modélisation du comportement mécanique des solides viscoélastiques par des opérateurs différentiels d'ordre non entier*. PhD thesis, École Centrale de Nantes, 1995. 23

H. Davis. *The theory of linear operators from the standpoint of differential equations of infinite order*. The Principia Press, Bloomington, Indiana, 1936. 127

E.A. De Souza Neto, D. Perić, and D.R.J. Owen. *Computational Methods for Plasticity: Theory and Applications*. John Wiley & Sons, Inc., 2008. 72, 73, 75

R. Desmorat. Positivite de la dissipation intrinsèque d'une classe de modeles d'endommagement anisotropes non standards. *Comptes Rendus Mécacanique*, 2006. 72

F. Detrez, S. Cantournet, and R. Séguéla. A constitutive model for semi-crystalline polymer deformation involving lamellar fragmentation. *Comptes Rendus Mécanique*, 338(12):681–687, 2010. ISSN 1631-0721. 61

F. Detrez, S. Cantournet, and R. Séguéla. Plasticity/damage coupling in semi-crystalline polymers prior to yielding: Micromechanisms and damage law identification. *Polymer*, 52(9):1998–2008, 2011. ISSN 0032-3861. 60

J.F. Deü and D. Matignon. Simulation of fractionally damped mechanical systems by means of a newmark-diffusive scheme. *Computers and Mathematics with Applications*, 59(5):1745–1753, 2010. 24

M. Enelund and P. Olsson. Damping described by fading memory - analysis and application to fractional derivative models. *International Journal of Solids and Structures*, 36(7):939–970, 1999. 23

L. Euler. De progressionibus transcendentibus, sev quarum termini generales algebraice dari nequevent. *Commentarii academiae scientiarum Petropolitanae*, 5:36–57, 1738. 24

P. Feraboli and K.T. Kedward. A new composite structure impact performance assessment program. *Composites Science and Technology*, 66(10):1336–1347, 2006. ISSN 0266-3538. 32, 33

W. Flügge. *Viscoelasticity*. 1967. 123

J.B.J. Fourier. *Théorie analytique de la chaleur*. Didot, Paris, 1822. 25

A. Galeski and G. Regnier. Part I Polymers: Nano- and Micromechanics of Crystalline Polymers. In József Karger-Kocsis and Stokyo Fakirov, editors, *Nano- and Mircro- Mechanics of Polymer Blends and Composites*, pages 1–58. Hanser, 2009. ISBN 978-3-446-41323-8. 58, 60

A.C. Galucio, J.F. De´u, and R. Ohayon. Finite element formulation of viscoelastic sandwich beams using fractional derivative operators. *Computational Mechanics*, 33(4):282–291, 2004. 24

D. Gay. *Matériaux composites*. Hermes, 5 edition, 2005. 56

A. Gemant. A method of analyzing experimental results obtained from elasto-viscous bodies. *Journal of Applied Physics*, 7(8):311–317, 1936. 23

A. Gemant. On fractional differentials. *Philos. Mag.*, 25:540–549, 1938. 23

L. Gornet and H. Ijaz. High cycle fatigue damage model for delamination crack growth in cf/epoxy composite laminates. *International Journal of Damage Mechanics*, 20(5):783–807, 2011. 56

L.E. Govaert and T. Peijs. Tensile strength and work of fracture of oriented polyethylene fibre. *Polymer*, 36(23):4425–4431, 1995. 19

L.E. Govaert, E.L. D'Hooghe, and T. Peijs. A micromechanical approach to the viscoelasticity of unidirectional hybrid composites. *Composites*, 22(2):113–119, 1991. 19

L.E. Govaert, C.W.M. Bastiaansen, and P.J.R. Leblans. Stress-strain analysis of oriented polyethylene. *Polymer*, 34(3):534–540, 1993. 19

J. Gresham, W.J. Cantwell, M. Cardew-Hall, P. Compston, and S. Kalyanasundaram. Drawing behaviour of metal-composite sandwich structures. *Composite Structures*, 75(1-4):305–312, 2006. ISSN 02638223. 18

A. K. Grünwald. Ûber "begrenzte" derivationen und deren anwendung. *Z. Math. und Phys.*, 12:441–480, 1867. 25

D. Halm and A. Dragon. An anisotropic model of damage and frictional sliding for brittle materials. *European Journal of Mechanics, A/Solids*, 17(3):439–460, 1998. 22

T. He and R.S. Porter. Melt transcrystallization of polyethylene on high modulus polyethylene fibers. *Journal of Applied Polymer Science*, 35(7):1945–1953, 1988. 18

C.T. Herakovich. *Mechanics of Fibrous Composites*. John Wiley & Sons, Inc., 1998. 56

F. Hild, A. Burr, and F.A. Leckie. Matrix cracking and debonding of ceramic-matrix composites. *International Journal of Solids and Structures*, 33(8):1209–1220, 1996. 22

F. Hild, A. Burr, and P. Feillard. On the mechanical behavior of fiber-reinforced composites. *Composite Structures*, 39(3-4):273–282, 1997. 21, 22

R. Hilfer. *Applications of fractional calculus in physics*. Singapur, 2000. 25

P.J Hine and I.M Ward. Hot compaction of woven poly(ethylene terephthalate) multifilaments. *Journal of Applied Polymer Science*, 91(4):2223–2233, 2004. 19

P.J. Hine, I.M. Ward, R.H. Olley, and D.C. Basset. The hot compaction of high modulus melt-spun polyethylene fibres. *Journal of Materials Science*, 28(2): 316–324, 1993. ISSN 0022-2461. 18

Ch. Hochard, P.A. Aubourg, and J.P. Charles. Modelling of the mechanical behaviour of woven-fabric cfrp laminates up to failure. *Composites Science and Technology*, 61(2):221–230, 2001. 22, 56

L. Holliday. The stiffness of polymers in relation to their structure. *Pure and Applied Chemistry*, 26(3-4):545–582, 1971. 58, 60

J.M. Quenisset J.M. Bribis and R. Naslain. Pseudo-plastic behavior of 2d carbon-carbon composite material. In *Proceedings of JNC5*, pages 313–328, Paris, 1985. 22

A.F. Johnson, A.K. Pickett, and P. Rozycki. Computational methods for predicting impact damage in composite structures. *Composites Science and Technology*, 61(15):2183–2192, 2001. 22

W.S. Johnson, E. Li, and J.L. Miller. High temperature hybrid titanium composite laminates: An early analytical assessment. *Applied Composite Materials*, 3 (6):379–390, 1996. 13

S. Kalyanasundaram, P. Compston, and J. Gresham. A methodology for real time surface strain measurement for stamping through non-contact optical strain measurement system. *Key Engineering Materials*, 344:855–861, 2007. 18

S. Kalyanasundaram, S. DharMalingam, S. Venkatesan, and A. Sexton. Effect of process parameters during forming of self-reinforced pp-based fiber metal laminate. *Composite Structures*, 97(0):332–337, 2013. ISSN 0263-8223. 18

A. Kmetty, T. Barany, and J. Karger-Kocsis. Self-reinforced polymeric materials: A review. *Progress in Polymer Science*, 35(10):1288–1310, 2010. ISSN 0079-6700. 17

R.C. Koeller. Applications of fractional calculus to the theory of viscoelasticity. *Journal of Applied Mechanics, Transactions ASME*, 51(2):299–307, 1984. 23, 76

Fv. Lacroix, M. Werwer, and K. Schulte. Solution impregnation of polyethylene fibre/polyethylene matrix composites. *Composites Part A: Applied Science and Manufacturing*, 29(4):371–376, 1998. ISSN 1359-835X. 18

Fv. Lacroix, H.Q. Lu, and K. Schulte. Wet powder impregnation for polyethylene composites: preparation and mechanical properties. *Composites Part A: Applied Science and Manufacturing*, 30(3):369–373, 1999. ISSN 1359-835X. 18

S.F. Lacroix. *Traité du calcul différentiel et du calcul intégral*. Gauthier-Villars, Paris, 1819. 25

P. Ladevèze. Sur la mécanique de l'endommagement des composites. In *Proceedings of the JNC 5*, page 667683, Paris, 1986. Pluralis. 21, 56, 58, 60

P. Ladevèze. Inelastic strains and damage; chapter 4 in damage mechanics of composite materials. *Composite Materials*, 1994. 56

P. Ladevèze. A damage computational approach for composites: basic aspects and micromechanical relations. 1995. 21

P. Ladevèze and E. LeDantec. Damage modelling of the elementary ply for laminated composites. *Composites Science and Technology*, 43(3):257–267, 1992. ISSN 0266-3538. 21, 22, 74

P.S. Laplace. *Théorie analytique des probabilités. Imprimeur-Libraire pour les Mathématiques.* Paris, 1812. 25

G.W. Leibniz and J. Bernouilli. Briefwechsel zwischen g. leibniz und j. bernouilli. *A. Asher & Comp. Leibnizens gesammelte Werke, Lebinizens mathematische Schriften, Erste Abtheilung, Band III,*, page 225, 1850a. 24

G.W. Leibniz and J. Bernouilli. Briefwechsel zwischen g. leibniz und j. bernouilli. *A. Asher & Comp. Leibnizens gesammelte Werke, Lebinizens mathematische Schriften, Erste Abtheilung, Band III,*, page 228, 1850b. 24

G.W. Leibniz and G. L'Hôpital. *Briefwechsel zwischen G. Leibniz und G. de L'Hôpital 301*, volume II of *301-302.* Pertz, G. H. and Gerhardt, C. J., 1849. 24

J. Lemaitre and R. Desmorat. Engineering damage mechanics. *Springer*, 2005. 22

A.V. Letnikov. Theory of differentiation of fractional order. *Moscow Matem. Sbornik*, 3:1–66, 1868. 25

E. Li and W.S. Johnson. An investigation into the fatigue of a hybrid titanium composite laminate. *Journal of Composites Technology and Research*, 20(1): 3–12, 1998. 14, 16

A. Lion. On the thermodynamics of fractional damping elements. *Continuum Mechanics and Thermodynamics*, 9(2):83–96, 1997. 77

R.L. Magin. *Fractional calculus in bioengineering*. Begell house, United States, Redding, Connecticut, 2006. 25

F. Mainardi. *Fractional calculus and waves in linear viscoelasticity*. Imperial College Press, London, 2010. 25

J.F. Maire. *Etude théorique et expérimentale du comportement de matériaux composites en contraintes planes*. PhD thesis, Université de Franche-Comté, 1992. 22

S. Marguet. *Contribution à la modélisation du comportemen mécanique des structures sandwichs soumises à limpact*. PhD thesis, Ecole Centrale de Nantes, 2007. 22

S. Marguet, P. Rozycki, and L. Gornet. A rate dependent constitutive model for carbon-fiber reinforced plastic woven fabrics. *Mechanics of Advanced Materials and Structures*, 14(8):619–631, 2007. 22

S.P.C. Marques and G.J. Creus. Laplace transform solutions. In *Computational Viscoelasticity*, pages 37–49. Springer Berlin Heidelberg, 2012. ISBN 978-3-642-25310-2. 126

M. Mateos. *Hysteretic and damage behaviour modelling of composite materials by fractional operators*. PhD thesis, École Centrale de Nantes, 2014. 22

M. Mateos, H. Zabala, L. Aretxabaleta, L. Gornet, and P. Rozycki. Hysteretic shear behaviour of fibre-reinforced composites. In *Proceedings of the 10th National Conference of Composite Materials (MATCOMP13), Algeciras, Spain*, 2013. 85

Y. Meerten, Y. Swolfs, J. Baets, L. Gorbatikh, and I. Verpoest. Penetration impact testing of self-reinforced composites. *Composites Part A: Applied Science and Manufacturing*, 68:289–295, 2015. 38

M.A. Meyers, P. Chen, A.Y. Lin, and Y. Seki. Biological materials: Structure and mechanical properties. *Progress in Materials Science*, 53(1):1–206, 2008. ISSN 0079-6425. 8

K.S. Miller and B. Ross. *An introduction to the fractional calculus and fractional differential equations*. New York, 1993. 25, 130

L. Mosse, W. Cantwell, M.J. Cardew-Hall, P. Compston, and S. Kalyanasundaram. A study of the effect of process variables on the stamp forming of rectangular cups using fibre-metal laminate systems. *Advanced Materials Research*, 6-8:649–656, 2005a. 18

L. Mosse, P. Compston, W.J. Cantwell, M. Cardew-Hall, and S. Kalyanasundaram. The effect of process temperature on the formability of polypropylene based fibre-metal laminates. *Composites Part A: Applied Science and Manufacturing*, 36(8):1158–66, 2005b. ISSN 1359-835X. 18

L. Mosse, P. Compston, W.J. Cantwell, M. Cardew-Hall, and S. Kalyanasundaram. Stamp forming of polypropylene based fibre-metal laminates: The effect of process variables on formability. *Journal of Materials Processing Technology*, 172(2):163–8, 2006. ISSN 0924-0136. 18

P.G. Nutting. A new general law of deformation. *Journal of the Franklin Institute*, 191(5):679–685, 1921. 23

L. Stainier O. Westphal, L. Gornet and P. Rozycki. Thermomechanical analysis of fatigue degradations in carbon/epoxy laminates. In *Proceedings of the 15th European Conference on Composite Materials - ECCM15*, page 2428, 2012. 22

K.B. Oldham and J. Spanier. *The fractional calculus*. 1974. 25, 26, 130

J. Padovan. Computational algorithms for fe formulations involving fractional operators. *Computational Mechanics*, 2(4):271–287, 1987. 24

T. Pärnänen, R. Alderliesten, C. Rans, T. Brander, and O. Saarela. Applicability of AZ31B-H24 magnesium in Fibre Metal Laminates - An experimental impact research. *Composites Part A: Applied Science and Manufacturing*, 43(9):1578–1586, 2012. ISSN 1359-835X. xi, 12, 13, 14, 40

T. Peijs. Composites for recyclability. *Materials Today*, 6(4):30–35, 2003. 18

I. Podlubny. *Fractional differential equations*. San Diego, 1999. 25, 26, 130

J. Pora and J. Hinrichsen. Material and technology developments for the airbus a380. In *Proceedings of the 22nd International SAMPE Europe Conference of the society for the Advancement of Materials and Process Engineering*, Paris, 2001. 9

C. Qin, N. Soykeabkaew, N. Xiuyuan, and T. Peijs. The effect of fibre volume fraction and mercerization on the properties of all-cellulose composites. *Carbohydrate Polymers*, 71(3):458–467, 2008. cited By (since 1996)58. 18

J. Rasburn, P.J. Hine, I.W. Ward, R.H. Olley, D.C. Bassett, and M.A. Kabeel. The hot compaction of polyethylene terephthalate. *Journal of Materials Science*, 30(3):615–622, 1995. 19

G. Reyes and W.J. Cantwell. Interfacial fracture in fibre-metal laminates based on glass fibre reinforced polypropylene. *Advanced Composites Letters*, 7(4): 97–102, 1998. 20

G. Reyes and W.J. Cantwell. The mechanical properties of fibre-metal laminates based on glass fibre reinforced polypropylene. *Composites Science and Technology*, 60(7):1085–94, 2000. ISSN 0266-3538. 20

G. Reyes and W.J. Cantwell. The high velocity impact response of composite and fml-reinforced sandwich structures. *Composites Science and Technology*, 64(1):35–54, 2004. ISSN 0266-3538. 16

G. Reyes and S. Gupta. Forming properties of a thermoplastic lightweight fiber-metal laminate. volume 1, pages 189–202, 2005. 18, 20

G. Reyes and S. Gupta. Manufacturing and mechanical properties of thermoplastic hybrid laminates based on DP500 steel. *Composites Part A: Applied Science and Manufacturing*, 40(2):176–183, 2009. 15, 16

G. Reyes and H. Kang. Mechanical behavior of lightweight thermoplastic fiber-metal laminates. *Journal of Materials Processing Technology*, 186(1-3):284–290, 2007. ISSN 0924-0136. 16, 20

M.O.W. Richardson and M.J. Wisheart. Review of low-velocity impact properties of composite materials. *Composites Part A: Applied Science and Manufacturing*, 27(12):1123–1131, 1996. ISSN 1359-835X. 17

G.F.B. Riemann. *Collected works of Bernhard Riemann*. Dover, New York, 1953. 25

M. Riesz. L'intégrale de riemann-liouville et le problème de cauchy. *Acta Mathematica*, 81(1):1–222, 1949. 26

P. Rojanapitayakorn, P.T. Mather, A.J. Goldberg, and R.A. Weiss. Optically transparent self-reinforced poly(ethylene terephthalate) composites: molecular orientation and mechanical properties. *Polymer*, 46(3):761–773, 2005. ISSN 0032-3861. 19

P. Rozycki. *Contribution au développement de lois de comportement pour matériaux composites soumis à l'impact*. PhD thesis, Université de Valenciènnes et du Hainaut-Cambresis, 2000. 21, 22, 58, 60

A.A. Kilbas S. Samko and O. Marichev. *Fractional Integrals and derivatives: Theory and Applications*. Gordon and Breach Science, Yverdon, 1993. 25, 130

A. Schmidt and L. Gaul. Finite element formulation of viscoelastic constitutive equations using fractional time derivatives. *Nonlinear Dynamics*, 29(1-4):37–55, 2002. 24

A. Schmidt and L. Gaul. On the numerical evaluation of fractional derivatives in multi-degree-of-freedom systems. *Signal Processing*, 86(10):2592–2601, 2006. 24

G.W. Scott-Blair and J.E. Caffyn. Vi. an application of the theory of quasi-properties to the treatment of anomalous strain-stress relations. *The London, Edinburgh, and Dublin Philosophical Magazine and Journal of Science*, 40(300): 80–94, 1949. 23

J.D. Seidt and A. Gilat. Plastic deformation of 2024-t351 aluminum plate over a wide range of loading conditions. *International Journal of Solids and Structures*, 50(10):1781–1790, 2013. ISSN 0020-7683. 68

A. Sexton, W.Cantwell, and S. Kalyanasundaram. Stretch forming studies on a fibre metal laminate based on a self-reinforcing polypropylene composite. *Composite Structures*, 94(2):431–437, 2012. ISSN 0263-8223. 18

J.C. Simo and T.J.R. Hughes. *Computational Inelasticity*. Springer-Verlag New York, 1998. 75

N.Y. Sonin. On differentiation with arbitrary index. *Moscow Matem. Sbornik*, 6 (1):1–38, 1869. 25

N. Soykeabkaew, N. Arimoto, T. Nishino, and T. Peijs. All-cellulose composites by surface selective dissolution of aligned ligno-cellulosic fibres. *Composites Science and Technology*, 68(10-11):2201–2207, 2008. 18

N. Stribeck. Part {IV} Nano- and Microcomposites: Characterization: Deformation Behavior of Nanocomposites Studied by X-Ray Scattering: Instrumentation and Methodology. In József Karger-Kocsis and Stokyo Fakirov, editors, *Nano- and Mircro- Mechanics of Polymer Blends and Composites*, pages 267–299. Hanser, 2009. ISBN 978-3-446-41323-8. 61

N.W. Tschoegl. *The Phenomenological Theory of Linear Viscoelastic Behavior - An Introduction*. Springer Berlin Heidelberg, 1989. 77

A. Vlot. Impact properties of fibre metal laminates. *Composites Engineering*, 3 (10):911–927, 1993a. ISSN 0961-9526. 10

A. Vlot. *Low-velocity Impact Loading on Fibre Reinforced Aluminium Laminates (ARALL and GLARE) and Other Aircraft Sheet Materials*. Delft University of Technology, Faculty of Aerospace Engineering, 1993b. 11, 16

A. Vlot. *Fibre metal laminates: an introduction*. Springer, 2001a. 9

A. Vlot. *Glare: history of the development of a new aircraft material*. Springer, 2001b. 9

I.M. Ward and P.J. Hine. The science and technology of hot compaction. *Polymer*, 45(5):1423–1437, 2004. 18

L. Yuan and O.P. Agrawal. A numerical scheme for dynamic systems containing fractional derivatives. *Journal of Vibration and Acoustics, Transactions of the ASME*, 124(2):321–324, 2002. 24

J.M. Zhang and T. Peijs. Self-reinforced poly(ethylene terephthalate) composites by hot consolidation of bi-component pet yarns. *Composites Part A: Applied Science and Manufacturing*, 41(8):964–972, 2010. ISSN 1359-835X. 19

J.M. Zhang, C.T. Reynolds, and T. Peijs. All-poly(ethylene terephthalate) composites by film stacking of oriented tapes. *Composites Part A: Applied Science and Manufacturing*, 40(11):1747–1755, 2009. ISSN 1359-835X. 18, 19

J.M Zhang, Z. Mousavi, N. Soykeabkaew, P. Smith, T. Nishino, and T. Peijs. All-aramid composites by partial fiber dissolution. *ACS Applied Materials and Interfaces*, 2(3):919–926, 2010. 18

Appendix A

A.1 Viscoelastic models

Viscoelasticity is the property of materials that exhibit both viscous and elastic characteristics when undergoing deformation [Flügge, 1967]. Viscoelastic materials, such as amorphous polymers, semicrystalline polymers, biopolymers and, by extension, polymer matrix composite materials can be modelled in order to determine their stress and strain or force and displacement interactions as well as their temporal dependencies [Christensen, 1982].

An ideal helicoidal spring, perfectly linear elastic and massless, represents Hooke model (see Fig. A.1), which is expressed by means of:

$$\sigma(t) = E\varepsilon(t) \tag{1}$$

where E is the elasticity modulus.

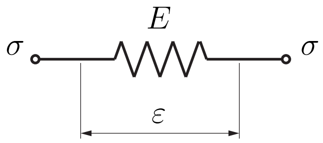

Figure A.1: Hookean elastic spring; elastic model.

The dashpot (see Fig. A.2) is an ideal viscous element that extends at a rate proportional to the applied stress, according to Newton equation:

$$\sigma(t) = \eta \frac{\mathrm{d}\varepsilon(t)}{\mathrm{d}t} \tag{2}$$

where η is the viscosity coefficient.

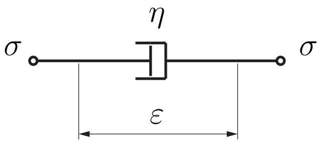

Figure A.2: Newtonian viscous dashpot; viscous model.

Combining springs and dashpots we obtain different models of viscoelastic behaviour. The simplest viscoelastic models are those formulated by J. C. Maxwell and Lord Kelvin.

The Kelvin model combines a spring and a dashpot in parallel (see Fig. A.3(a)), whereas the Maxwell model is the combination of a spring and a dashpot in series (see Fig. A.3(b)).

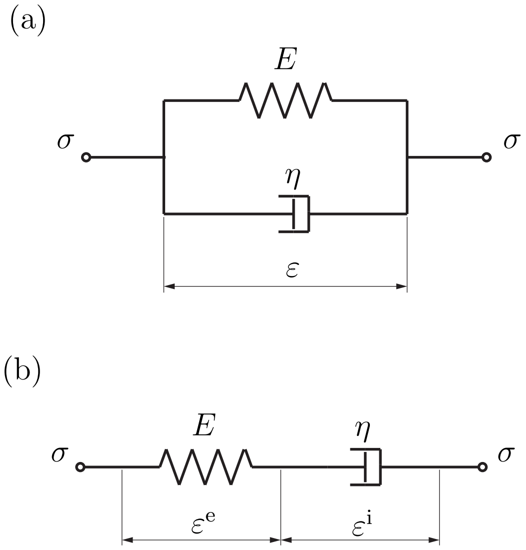

Figure A.3: (a) Kelvin and (b) Maxwell viscoelastic models.

Maxwell and Kelvin models are adequate for qualitative and conceptual analyses, but sometimes poor for the quantitative representation of the behaviour of real materials.

In order to get a more realistic response by the model, the number of parameters must be increased by combining a number of springs and dashpots. A systematic way to do that is to build generalized Maxwell and Kelvin models. The generalized Maxwell model is composed of $n+1$ constituent elements in parallel, being n Maxwell models and an isolated spring (to warrant solid behaviour) (see Fig. A.4(a)), while the generalized Kelvin model is composed of n Kelvin units in series plus an isolated spring (see Fig. A.4(b)).

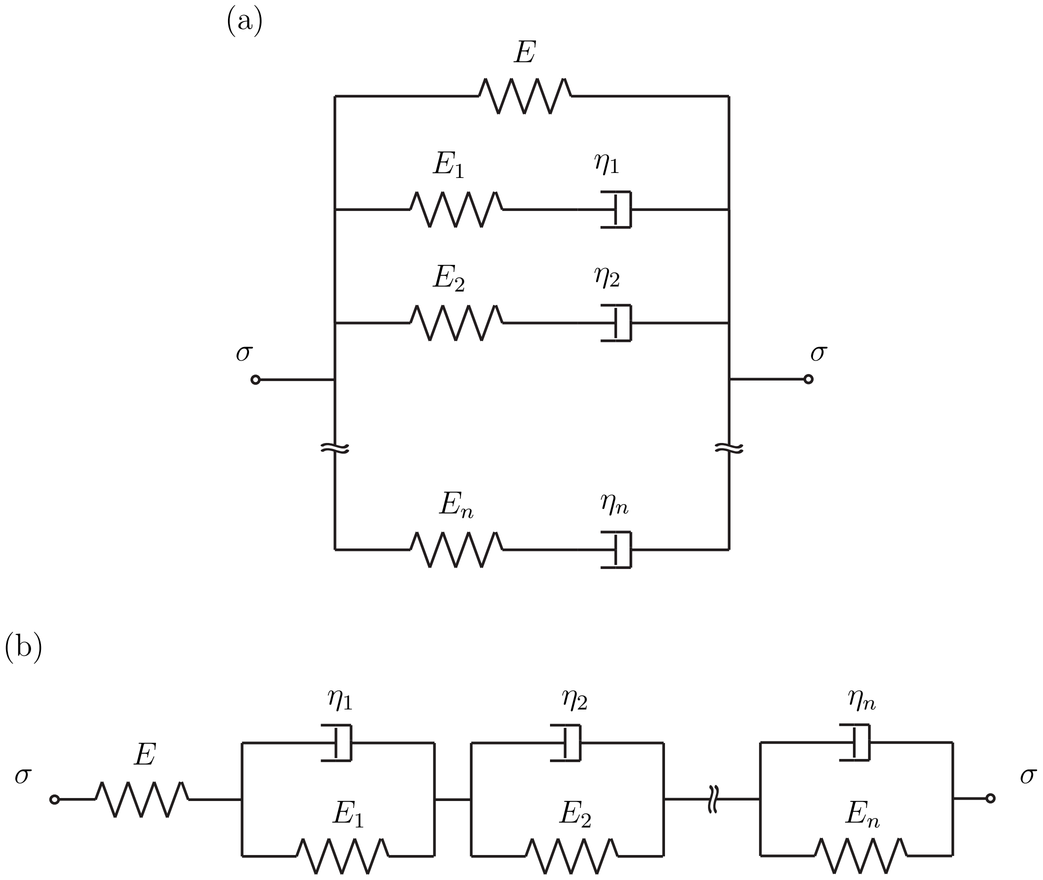

Figure A.4: Generalized (a) Maxwell and (b) Kelvin viscoelastic models.

The classic general differential representation of rheological models is [Marques and Creus, 2012]

$$\sum_{i=0}^{h} p_i \frac{\partial^i \sigma}{\partial t^i} = \sum_{i=0}^{k} p_j \frac{\partial^j \varepsilon}{\partial t^j} \tag{3}$$

where p_i and q_j are material constants dependent on the viscoelastic model, being i and j the derivation orders, entire, of the derivatives of stress and stress, respectively, with respect to time.

The generalized Maxwell and Kelvin models are the more complete among the classical rheological models. They allow to model the viscous mechanical behaviour of polymer and polymer matrix composite materials considering effects such as hysteretic phenomena [Bois, 2003].

Appendix B

B.1 Euler's Gamma function

In fractional calculus, the complete Euler's Gamma function $\Gamma(z)$ is a fundamental function which is defined by an Euler integral of second kind:

$$\Gamma(z) = \int_0^{\infty} t^{z-1} \mathrm{e}^{-t} \mathrm{d}t \tag{4}$$

This function is defined in the whole complex plane except for zero and negative integers, where it has poles. Integrating by parts Eq. 4 leads to the following recurrence relationship:

$$\Gamma(z+1) = z\Gamma(z) \tag{5}$$

Since $\Gamma(1) = 1$ by Eq. 4, Eq. 5 then provides the generalisation of factorial $z!$:

$$\Gamma(z+1) = z! \tag{6}$$

B.2 Definitions of fractional operators

As stated before, fractional calculus is a generalisation to non-integer order of the integration and differentiation operator, which will be in general called integro-differentiation operator within this work. The notation that will be used is the one proposed by Davis [1936] which denotes the integro-differential operator of a function $f(x)$ by:

$$ {}_{a}\mathrm{D}_{b}^{\alpha} f(x) $$

where subscripts a and b denote the lower and upper limits or terminals of the integral, respectively, which defines the integro-differentiation of order α. In general, the use of subscripts becomes crucial in order to avoid ambiguities and in the cases of no ambiguity they may be omitted, as it will be seen later in this work.

For positive values of α the integro-differential operator produces a fractional derivative, whereas for negative values, the integro-differential operator produces a fractional integral. In this case the following notation may be used:

$$ {}_{a}\mathrm{I}_{b}^{\alpha} f(x) $$

Thus, the following relation is obtained:

$$ {}_{a}\mathrm{D}_{b}^{-\alpha} f(x) = {}_{a}\mathrm{I}_{b}^{\alpha} f(x) \tag{7} $$

Fractional operators fulfill the following properties:

Property 1 *If $f(x)$ is an analytic function of the real or complex variable z, the derivative ${}_{a}\mathrm{D}_{z}^{\alpha} f(z)$ is an analytic function of α and z.*

Property 2 *Fractional differentiation ${}_{a}\mathrm{D}_{x}^{\alpha} f(x)$ must produce the same result as ordinary differentiation for positive integer values n of α and the same as ordinary n-fold integration for negative integer values n of α.*

Property 3 *After fractional integro-differentiation of order zero the function remains unchanged:*

$$ {}_{a}\mathrm{D}_{x}^{0} f(x) = f(x) \tag{8} $$

Property 4 *Fractional operators are linear:*

$$ {}_a\mathrm{D}_x^{\alpha} \sum_{i=1}^{N} a_i f_i(x) = \sum_{i=1}^{N} a_i \, {}_a\mathrm{D}_x^{\alpha} f_i(x) \tag{9}$$

Property 5 *The composition rule for integration of arbitrary order holds:*

$$ {}_a\mathrm{I}_x^{\beta} \left({}_a\mathrm{I}_x^{\alpha} f(x) \right) = {}_a\mathrm{I}_x^{\alpha+\beta} f(x) = {}_a\mathrm{I}_x^{\alpha} \left({}_a\mathrm{I}_x^{\beta} f(x) \right) \qquad \alpha, \beta \geq 0 \tag{10}$$

or alternatively,

$$ {}_a\mathrm{D}_x^{-\beta} \left({}_a\mathrm{D}_x^{-\alpha} f(x) \right) = {}_a\mathrm{D}_x^{-\alpha-\beta} f(x) = {}_a\mathrm{D}_x^{-\alpha} \left({}_a\mathrm{D}_x^{-\beta} f(x) \right) \qquad \alpha, \beta \geq 0 \tag{11}$$

Property 6 *The composition rule for differentiation and integration of arbitrary order holds:*

$$ {}_a\mathrm{D}_x^{\beta} \left({}_a\mathrm{I}_x^{\alpha} f(x) \right) = {}_a\mathrm{D}_x^{\beta-\alpha} f(x) \qquad \alpha, \beta \geq 0 \tag{12}$$

Thus, if $\beta = \alpha$, then:

$$ {}_a\mathrm{D}_x^{\alpha} \left({}_a\mathrm{I}_x^{\alpha} f(x) \right) = f(x), \;\; {}_a\mathrm{I}_x^{\alpha} \left({}_a\mathrm{D}_x^{\alpha} f(x) \right) \neq f(x) \qquad \alpha \geq 0 \tag{13}$$

i.e. *the fractional derivative operator* D^{α} *is left-inverse and not right-inverse to the fractional integral operator* I^{α} *with* α *a non-integer number. The same could be said for integer order numbers* n*.*

Property 7 *The composition rule for differentiation of arbitrary order does not generally hold but in the case of hybrid differentiation with* n *a positive integer* *and α non-integer, the following property holds:*

$$ {}_a\mathrm{D}_x^{\alpha}\left({}_a\mathrm{D}_x^{n} f(x)\right) = {}_a\mathrm{D}_x^{n+\alpha} f(x) - \sum_{k=0}^{n-1} \frac{(x-a)^{k-\alpha-n} f^{(k)}(a)}{\Gamma(k-\alpha-n+1)} \qquad \alpha, n \geq 0 \qquad (14) $$

If the derivatives $f^{(k)}(a)$ at the lower terminal vanish for $k = 0, 1, \ldots n-1$, then:

$$ {}_a\mathrm{D}_x^{\alpha}\left({}_a\mathrm{D}_x^{n} f(x)\right) = {}_a\mathrm{D}_x^{n+\alpha} f(x) \qquad \alpha, n \geq 0 \qquad (15) $$

As it has previously been seen, several different fractional operators have been developed throughout history. In the following subsections the main operators relevant to this work will be described: the Grnwald-Letnikov (GL) definition, the Riemann-Liouville (RL) and the Caputo (C) definitions [Miller and Ross, 1993; Oldham and Spanier, 1974; Podlubny, 1999; S. Samko and Marichev, 1993]. As it will be seen in the following subsections, while the first one is a discrete approach since it is based on a generalised difference quotient, the other two are based on an integral formulation, that is, they constitute a continuous approach.

Appendix C

C.1 Algorithms

Algorithm 1 Model algorithm for the quasi-static cyclic tensile and shear cases.

```
if $\underbrace{(\Delta\varepsilon_{ij.\,n} > 0 \text{ and } \sigma_{\mathrm{y}}(\bar{\varepsilon}_n^{\mathrm{p\ trial}}) = 0)}_{\mathrm{elastic-part}}$ or $\underbrace{(\Delta\varepsilon_{ij.\,n} > 0 \text{ and } \sigma_{\mathrm{y}}(\bar{\varepsilon}_n^{\mathrm{p\ trial}}) < \sigma_{\mathrm{y}}(\bar{\varepsilon}_{n-1}^{\mathrm{p\ trial}})}_{\mathrm{plastic-part}}$, then
    $\Delta\varepsilon_{ij.\,n} > 0$ is supposed to be elastic: an elastic prediction is calculated.
            –GO TO Algorithm 2–
    Then, the plastic admissibility is checked.
    if $q_{n+1}^{\mathrm{trial}} - \sigma_{\mathrm{y}}(\bar{\varepsilon}_{n+1}^{\mathrm{p\ trial}}) \leq 0$ then
        The elastic prediction is correct, so
            $(\cdot)_{n+1} := (\cdot)_{n+1}^{\mathrm{trial}}$
    else
        The Return Mapping algorithm is applied.
            –GO TO Algorithm 3–
    end if
else
    $\Delta\varepsilon_{ij.\,n}$ occurs within the hysteresis loop.
            –GO TO Algorithm 4–
end if
```

Algorithm 2 Elastic predictor.

```
Given $\Delta\varepsilon_{ij.\,n} > 0$ and the state variables at $t_n$, the **elastic prediction** is calculated.
    $\varepsilon^{\mathrm{e\ trial}}_{ij.\,n+1} := \varepsilon^{\mathrm{e}}_{ij.\,n} + \Delta\varepsilon_{ij.\,n}$
    $\bar{\varepsilon}^{\mathrm{p\ trial}}_{n+1} := \bar{\varepsilon}^{\mathrm{p}}_{n}$
    $Y^{\mathrm{trial}}_{ij.\,n+1} := Y_{ij}(\varepsilon^{\mathrm{e\ trial}}_{ij.\,n+1}); \quad \bar{Y}^{\mathrm{trial}}_{ij.\,n+1} := \max_{\tau \le t}\left(\sqrt{Y^{\mathrm{trial}}_{ij.\,n+1}(\tau)}\right)$
    $Z^{\mathrm{trial}}_{ij.\,n+1} := Z_{ij}(\varepsilon^{\mathrm{e\ trial}}_{ij.\,n+1}); \quad \bar{Z}^{\mathrm{trial}}_{ij.\,n+1} := \max_{\tau \le t}\left(\sqrt{Z^{\mathrm{trial}}_{ij.\,n+1}(\tau)}\right)$
    $d^{\mathrm{trial}}_{ij.\,n+1} := f_{ij}(\bar{Y}^{\mathrm{trial}}_{ij.\,n+1})$
    $r^{\mathrm{trial}}_{ij.\,n+1} := g_{ij}(\bar{Y}^{\mathrm{trial}}_{ij.\,n+1})$
    $q^{\mathrm{trial}}_{n+1} := \sqrt{(\tilde{\sigma}^2_{12} + a^2_1\tilde{\sigma}^2_{11} + a^2_2\tilde{\sigma}^2_{22})}$
```

Algorithm 3 Return Mapping

```
Solve numerically the system
    $\varepsilon^{\mathrm{e}}_{ij.\,n+1} := \varepsilon^{\mathrm{e\ trial}}_{ij.\,n+1} - \Delta\gamma N_{n+1}$    (see Eq. 5.19 to determine $N_{n+1}$)
    $\bar{\varepsilon}^{\mathrm{p}}_{n+1} := \bar{\varepsilon}^{\mathrm{p}}_{n} + \Delta\gamma$
    $q^{\mathrm{trial}}_{n+1} - \sigma_{\mathrm{y}}(\bar{\varepsilon}^{\mathrm{p\ trial}}_{n+1}) = 0$
for $\varepsilon^{\mathrm{e}}_{ij.\,n+1}$, $\bar{\varepsilon}^{\mathrm{p}}_{n+1}$ and $\Delta\gamma$ (using e.g the Newton-Raphson method) and update $d_{ij.\,n+1}$, $d_{ij.\,n+1}$ and $q_{n+1}$.
```

Algorithm 4 Hysteresis loops.

```
if $\underbrace{i \neq j}_{\text{unloading-or-reloading-shear}}$ or $\underbrace{(i = j \text{ and } \Delta\varepsilon_{ij.\,n} < 0)}_{\text{unloading-tensile}}$ then
    The F-SLS model must be applied.
        $\varepsilon^{\mathrm{e}}_{ij.\,n+1} := \varepsilon^{\mathrm{e}}_{ij.\,n} + \Delta\varepsilon_{ij.\,n}$
        $\bar{\varepsilon}^{\mathrm{p}}_{n+1} := \bar{\varepsilon}^{\mathrm{p}}_{n}$
        $\varepsilon_{ij.\,n+1} := \varepsilon^{\mathrm{e}}_{ij.\,n+1} + \bar{\varepsilon}^{\mathrm{p}}_{n+1}$
    and the value of the material parameters are determined:
        $E^{*}_{ij.\,n+1} := E^{*}_{ij}(\bar{\varepsilon}^{\mathrm{p}}_{n+1})$
        $E^{\mathrm{v}}_{ij.\,n+1} := E^{\mathrm{v}}_{ij}(\bar{\varepsilon}^{\mathrm{p}}_{n+1})$
        $E^{\mathrm{m}}_{ij.\,n+1} := E^{\mathrm{m}}_{ij}(\bar{\varepsilon}^{\mathrm{p}}_{n+1})$
        $\alpha_{ij.\,n+1} := \alpha_{ij}(\bar{\varepsilon}^{\mathrm{p}}_{n+1})$
    Then, the stress state is calculated based on the F-SLS model:
        $\sigma_{ij.\,n+1} + \frac{E^{\mathrm{v}}_{ij.}}{E^{\mathrm{m}}_{ij.\,n+1}}\, {}_{n}\mathrm{D}^{\alpha}_{n+1}\sigma_{ij.} =$
            $= E^{*}_{ij.\,n+1}\varepsilon_{ij.\,n+1} + \frac{E^{*}_{ij.\,n+1} + E^{\mathrm{m}}_{ij.}}{E^{\mathrm{m}}_{ij.}} E^{\mathrm{v}}_{ij.\,n+1}\, {}_{n}\mathrm{D}^{\alpha}_{n+1}\varepsilon_{ij.}$
else
    $\underbrace{i = j}_{\text{reloading-tensile}}$, so the linear elastic model is applied.
        $E^{\mathrm{r}}_{ij.\,n+1} := E^{\mathrm{r}}_{ij}(\bar{\varepsilon}^{\mathrm{p}}_{n+1})$
        $\sigma_{ij.\,n+1} := E^{\mathrm{r}}_{ij}(\varepsilon^{\mathrm{e}}_{ij.\,n} + \Delta\varepsilon_{ij.\,n})$
end if
```